NASA Contractor Report 195368

Micromechanical Modeling of the Thermal Expansion of Graphite/Copper Composites With Nonuniform Microstructure

Brett A. Bednarcyk and Marek-Jerzy Pindera
University of Virginia
Charlottesville, Virginia

August 1994

Prepared for
Lewis Research Center
Under Grant NAG3–1319

National Aeronautics and
Space Administration

Page intentionally left blank

Abstract

Two micromechanical models were developed to investigate the thermal expansion of graphite/copper (Gr/Cu) composites. The models incorporate the effects of temperature-dependent material properties, matrix inelasticity, initial residual stresses due to processing history, and nonuniform fiber distribution. The first model is based on the multiple concentric cylinder geometry, with each cylinder treated as a two-phase composite with a characteristic fiber volume fraction. By altering the fiber volume fraction of the individual cylinders, unidirectional composites with radially nonuniform fiber distributions can be investigated using this model. The second model is based on the inelastic lamination theory. By varying the fiber content in the individual laminae, composites with nonuniform fiber distribution in the thickness direction can be investigated. In both models, the properties of the individual regions (cylinders or laminae) are calculated using the method of cells micromechanical model. Classical incremental plasticity theory is used to model the inelastic response of the copper matrix at the micro-level.

The models were used to characterize the effects of nonuniform fiber distribution on the thermal expansion of Gr/Cu. These effects were compared to the effects of matrix plasticity, choice of stress-free temperature, and slight fiber misalignment. It was found that the radially nonuniform fiber distribution has little effect on the thermal expansion of Gr/Cu but could become significant for composites with large fiber-matrix transverse CTE and Young's modulus mismatch. The effect of nonuniform fiber distribution in the through-thickness direction of a laminate was more significant, but only approached that of the stress-free temperature for the most extreme cases that include large amounts of bending. Subsequent comparison with experimental thermal expansion data indicated the need for more accurate characterization of the graphite fiber thermo-mechanical properties. Correlation with cyclic data revealed the presence of a mechanism not considered in the developed models. The predicted response did, however, exhibit ratcheting behavior that has been observed experimentally in Gr/Cu. Finally, simulation of the actual fiber distribution of particular specimens had little effect on the predicted thermal expansion.

Acknowledgments

This research was supported by NASA Lewis Research Center, Cleveland, OH through Grant No. NASA NAG3-1319. The authors are grateful for this financial support, and the technical advice and assistance of the NASA grant monitor, Dr. Robert V. Miner. The first author would particularly like to thank Drs. David Ellis and Sandra DeVincent for making the NASA Lewis experience an enjoyable and exciting one, and for the assistance in the experimental portions of this investigation. The thermal expansion test results presented in this report have been generated by Dr. DeVincent at the NASA Lewis Research Center.

Table of Contents

Abbreviations

ABAQUS ..... commercially available finite element package

CCMICRON ..... analytical model consisting of the combination of the multiple concentric cylinder model and the method of cells

CTE ..... coefficient of thermal expansion

Gr/Cu ..... graphite/copper

Ksi ..... thousand pounds per square inch

lb_f ..... pounds force

MCLAM ..... analytical model consisting of the combination of lamination theory and the method of cells

mm ..... millimeter

Msi ..... million pounds per square inch

OFHC ..... oxygen free high conductivity

P100 ..... kind of graphite fiber

SFT ..... stress-free temperature

Temp ..... temperature

um ..... micron

V_f ..... fiber volume fraction

v/o ..... fiber volume fraction

°F ..... degrees Fahrenheit

Symbols

1, 2, 3 ..... Cartesian coordinate directions for a lamina

$A_1 \ldots A_{12}$ ..... variables introduced for notational simplicity in the method of cells

A_1^k, A_2^k ..... unknown coefficients in the multiple concentric cylinder model

A_c ..... cylindrical assemblage cross-sectional area

A_{ij} ..... components of the extensional stiffness matrix

b_{ij} ..... method of cells effective stiffness matrix components

B_{ij} ..... components of the coupling stiffness matrix

C_{ij} ..... stiffness matrix components

C_{ij}^* ..... method of cells averaged effective stiffness components

$C_{ij}^{(\beta\gamma)}$ ..... subcell stiffness components

$\overline{C}_{ij}^k$ ..... rotated stiffness components

D ..... variable introduced for notational simplicity in the method of cells

D_{ij} ..... components of the bending stiffness matrix

dH_{11}, dH_{22}, dH_{33}, dH_{12} ..... increments in the H_{ij} terms

$d\lambda$ ..... proportionality constant in classical incremental plasticity theory

$d\varepsilon_1^p$, $d\varepsilon_2^p$, $d\varepsilon_3^p$, $d\varepsilon_{12}^p$ ..... plastic strain increments

$d\varepsilon_{eff}^p$ ..... effective plastic strain increment

E ..... isotropic Young's modulus

E_A ..... axial Young's modulus

E_T ..... transverse Young's modulus

E_1^k ..... axial Young's modulus in the kth layer

E_2^k ..... transverse Young's modulus in the kth layer

e'_{ij} ..... modified strain deviator

f ..... generic function

f, m ..... fiber, matrix

f_i^k ..... thermal force terms in the multiple concentric cylinder model

F_i^T ..... variable introduced for notational simplicity in the method of cells

$\underline{F}^m$ ..... mechanical force vector

$\underline{F}^p$ ..... plastic force vector

$\underline{F}^T$ ..... thermal force vector

G ..... isotropic shear modulus

G_A ..... axial shear modulus

$G(r), \overline{G}(r)$ ..... functions introduced for notational simplicity in the multiple concentric cylinder model

G_{12}^k ..... axial shear modulus

g_i^k ..... plastic force terms in the multiple concentric cylinder model

H ..... total laminate thickness

h, l ..... unit cell dimensions

H_1, H_2 ..... variables introduced for notational simplicity in the multiple concentric cylinder model

$H_{11}, H_{22}, H_{33}, H_{12}$ ..... functions involving plastic strains introduced for notational simplicity in the method of cells

h_1, h_2, l_1, l_2 ..... subcell dimensions

HSP, H ..... hardening slope

$J_1 \ldots J_4$ ..... variables introduced for notational simplicity in the method of cells

k ..... denotes an arbitrary cylinder or lamina

k_{ij}^k ..... local/global stiffness matrix components

M_x, M_y, M_{xy} ..... laminate moments per unit length

n ..... number of cylinders in assemblage

N ..... number of laminae in the laminate

N_x, N_y, N_{xy} ..... laminate forces per unit length

Q_i, Q_i', Q_i'' ..... variables introduced for notational simplicity in the method of cells

Q_{ij}^k ..... reduced stiffness matrix components

$\overline{Q}_{ij}^k$ ..... rotated reduced stiffness matrix components

r_k ..... radial position of the kth interface in an assemblage of cylinders

r' ..... variable of integration

$\underline{\underline{SM}}$ ..... generic stiffness matrix

$S_{ij}^{(\beta\gamma)}$ ..... average subcell stress components

$\underline{S}^f$ ..... fiber compliance matrix

$\underline{S}^m$ ..... matrix material compliance matrix

$\underline{S}^*$ ..... effective composite compliance matrix

T ..... current temperature

T_0 ..... reference temperature

$T_1 \ldots T_{16}$ ..... variables introduced for notational simplicity in the method of cells

$[T]$ ..... rotation matrix

u, v, w ..... displacement components in the coordinate directions

u_0, v_0, w_0 ..... midplane displacement components

$u_i^{(\beta\gamma)}$ ..... subcell displacement components

V ..... unit cell volume

V_c ..... composite volume

$V_{\beta\gamma}$ ..... subcell volume

$w_i^{(\beta\gamma)}$ ..... displacement components of the centers of the subcells

w_k^+, w_k^- ..... radial displacements at interfaces of concentric cylinders

x, r, θ ..... cylindrical coordinate directions

x, y, z ..... Cartesian coordinate directions in a laminate

x_0 ..... generic position variable

$x_1, \bar{x}_2^{(\beta)}, \bar{x}_3^{(\gamma)}$ ..... subcell local coordinate directions

Y ..... yield stress

z_k ..... through-thickness position of the kth interface in a laminate

α ..... isotropic CTE

α_A ..... axial CTE

α_T ..... transverse CTE

$\alpha_{xx}, \alpha_{\theta\theta}, \alpha_{rr}$ ..... CTEs in cylindrical coordinate directions

α_1^k, α_2^k ..... CTEs in the principal material coordinates of a lamina

α_x^k, α_y^k, α_{xy}^k ..... CTEs in the laminate coordinates

α_z^k ..... through-thickness CTE of a lamina

$\alpha_1^{(\beta\gamma)}$, $\alpha_2^{(\beta\gamma)}$ ..... subcell CTEs

α_1^*, α_2^* ..... method of cells effective CTEs

$\underline{\alpha}^f$ ..... fiber CTE vector

$\underline{\alpha}^m$ ..... matrix CTE vector

$\underline{\alpha}^*$ ..... effective CTE vector

$(\beta\gamma)$ ..... denote individual subcells

ΔT ..... change in temperature from a reference temperature

Δx ..... generic change in position

δ_{ij} ..... Kronecker delta

ε_0 ..... uniform longitudinal strain

ε_1, ε_2, γ_{12} ..... total strain components in the principal material coordinates of a lamina

ε_{et} ..... equivalent modified total strain

ε_{xx}, $\varepsilon_{\theta\theta}$, ε_{rr} ..... total strain components in cylindrical coordinates

ε_x, ε_y, γ_{xy} ..... total strain components in the laminate coordinates

ε_z ..... through-thickness total strain

$\overline{\varepsilon}_{ij}$ ..... average cell strain components

ε_x^0, ε_y^0, γ_{xy}^0 ..... midplane strain components

ε_1^p, ε_2^p, γ_{12}^p ..... plastic strain components in the principal material coordinates

ε^p_{eff} ..... effective plastic strain

$\varepsilon^p_{eff}\big|_{previous}$ ..... effective plastic strain at the end of the previous loading increment

$\varepsilon^p_{ij}\big|_{previous}$ ..... plastic strain components at the end of the previous loading increment

ε^p_{xx}, $\varepsilon^p_{\theta\theta}$, ε^p_{rr} ..... plastic strain components in cylindrical coordinates

ε^p_x, ε^p_y, γ^p_{xy} ..... plastic strain components in the laminate coordinates

ε^p_z ..... through-thickness plastic strain

$\varepsilon^{(\beta\gamma)}_{ij}$ ..... subcell total strain components

$\varepsilon^{e(\beta\gamma)}_{ij}$ ..... subcell elastic strain components

$\varepsilon^{p(\beta\gamma)}_{ij}$ ..... subcell plastic strain components

$\varepsilon^{T(\beta\gamma)}_{ij}$ ..... subcell thermal strain components

θ ..... angle relating principal material and laminate coordinates

κ_x, κ_y, κ_{xy} ..... midplane curvatures

λ ..... variable introduced for notational simplicity in the multiple concentric cylinder model

ν ..... isotropic Poisson's ratio

ν_A ..... axial Poisson's ratio

ν_T ..... transverse Poisson's ratio

ν^k_{12}, ν^k_{21} ..... Poisson's ratios in the kth layer

$\underline{\xi}$ ..... generic unknown vector

ρ_c ..... composite density

ρ_f ..... fiber density

ρ_m ..... matrix density

$\sigma_1, \sigma_2, \tau_{12}$ ..... stress components in the principal material coordinates of a lamina

σ_{eff} ..... effective stress

$\sigma_{xx}, \sigma_{\theta\theta}, \sigma_{rr}$ ..... stress components in cylindrical coordinates

$\sigma_x, \sigma_y, \tau_{xy}$ ..... stress components in the laminate coordinates

σ_Y ..... yield stress

σ_z ..... through-thickness stress

$\overline{\sigma}_{ij}$ ..... average cell stress components

$\sigma_{ij}^{(\beta\gamma)}$ ..... subcell stress components

$\sigma_{rr}^{k+}, \sigma_{rr}^{k-}$ ..... radial stresses at the interfaces of the concentric cylinders

$\phi_{11}^k, \phi_{22}^k, \psi_k, \Omega_k, \Pi_k$ ..... variables introduced for notational simplicity in the multiple concentric cylinder model

$\phi_i^{(\beta\gamma)}, \psi_i^{(\beta\gamma)}$ ..... microvariables in the method of cells

Figures

1. Introduction

A composite material is formed by reinforcing one material with another. The result is a new material with properties distinct from either of the constituents. Composites are classified by the type of matrix material (polymer, ceramic, or metal) and by the type of reinforcements (particles, chopped fibers, or continuous fibers). Continuous fiber-reinforced metal matrix composites consist of a metal matrix reinforced with continuous fibers. This type of composite may have unidirectional fibers only, or it may have layers with fibers oriented in different directions. The latter type of fiber-reinforced composite is referred to as a laminate.

Figure 1.1 shows a micrograph of unidirectional graphite/copper (Gr/Cu), a continuous fiber-reinforced metal matrix composite, with the long fiber direction perpendicular to the page. Composite materials are desirable for many applications because they are generally stiff and strong but low in density. This is the case for Gr/Cu. Copper is displaced by the less dense graphite fibers, so the composite is lighter than pure copper. In addition, the fibers are stiffer and stronger than pure copper in the long fiber direction, thus the composite is stiffer and stronger in this direction as well.

In recent years, many new applications have become apparent for composite materials, partially fueled by reduced manufacturing costs and improved quality. However, use of composites actually dates

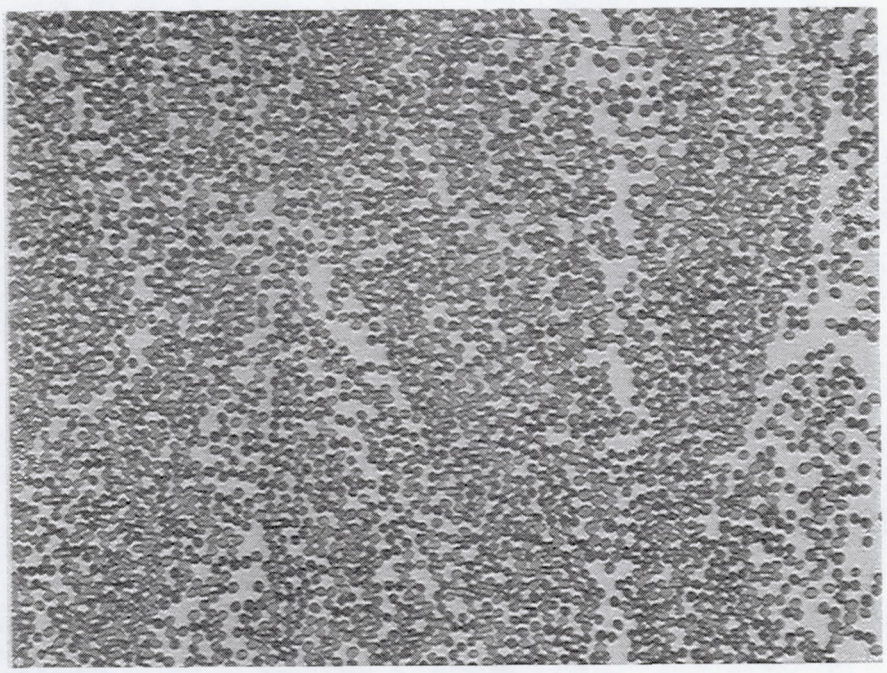

Figure 1.1: Micrograph of a cross-section of unidirectional Gr/Cu. Dark circles are graphite fibers, light areas are copper. Courtesy of S.M. DeVincent.

back a long time. Wood, one of the first structural materials used by man, is a natural composite. It consists of lignin, an amorphous polymer, reinforced with cellulose fibers (Ashby and Jones, 1980). One of the oldest and most common man-made composites is reinforced concrete. Steel rods are imbedded in the concrete in the direction of loading to increase the strength of the material. Fiberglass is a good example of another composite that has been in use for decades. This and other polymer matrix composites are easy to manufacture because of the low melting or softening temperatures of polymers. Thus, polymer matrix composites have been used extensively for applications including boat components and sporting goods. Ceramic matrix composites have also found a niche in the sporting goods industry.

Many of the current generation high-performance aircraft are manufactured partly from composite materials. Examples include the boron/epoxy horizontal stabilizer of the Grumman F-14, and the vertical and horizontal stabilizers of the McDonnell-Douglas F-15 (Jones, 1975). The main drawback

of polymer matrix composites is the same characteristic that makes them easy to manufacture; namely their low softening temperature. Thus for elevated temperature applications for aircraft and reentry vehicles, metal matrix composites are desirable. Metal matrix composites are much more difficult to manufacture, but the weight savings over un-reinforced metals can be dramatic. This is why there is currently much research focusing on metal matrix composites such as silicon carbide/titanium. This and other metal matrix composites may potentially become major structural materials for aerospace applications well into the next century.

One might wonder why entire structures are not made from the reinforcement material since it provides superior strength and stiffness and lower density than unreinforced metals. The answer is that reinforcement materials such as graphite, boron, and silicon carbide are ceramics. Thus they are brittle and susceptible to rapid crack growth and fracture. When drawn into fibers, many of these materials have oriented microstructures, giving them highly favorable properties in one direction at the expense of the properties in the other directions. In addition, some inclusion materials, such as graphite, oxidize significantly in air at temperatures well below the melting point of matrix metals. By combining fibers with metals, the most desirable properties of both materials are preserved while many drawbacks associated with the individual materials are eliminated.

Gr/Cu is unique from other metal matrix composites in several ways. Copper exhibits the highest thermal conductivity of any metal, but it also has a high density and a high coefficient of thermal expansion (CTE). By reinforcing copper with graphite fibers, the density and longitudinal thermal expansion are significantly reduced while the thermal conductivity remains quite high. This unique combination of features has made Gr/Cu a leading candidate material for high heat transfer applications in which low weight is a design consideration. These applications include heat exchangers for spacecraft and reentry vehicles. The leading edges of the airfoil of the proposed national aerospace plane (NASP) were to reach temperatures on the order of 1450° C as the vehicle reentered the atmosphere (Upadhya, 1992). NASA proposed to actively cool the leading edges with a hydrogen slurry. To make this process efficient, the material from which the heat exchanger is manufactured should have a high thermal conductivity. A lower density, high thermal conductivity material such as Gr/Cu can save weight,

allowing reentry vehicles like the NASP to operate more economically. The same holds for spacecraft power thermal management systems. As an example, for the SP-100 nuclear power system, the mass of the radiators may account for as much as 90% of the total mass of the power system (Ellis, 1992). Using Gr/Cu for this application will save weight. Thus, NASA is interested in developing Gr/Cu composites and better understanding their thermo-mechanical behavior. The thermal expansion of this material is of particular importance since it is likely that Gr/Cu components will experience a wide range of temperatures over their lifetimes.

Composites may seem ideal for many applications, but drawbacks do exist which depend on the particular material system. For metal matrix composites such as Gr/Cu, these drawbacks include the difficulty and the expense of manufacturing them. The fabrication of Gr/Cu has been the topic of much research at NASA Lewis. Bonding between the fiber and the matrix has been a problem because graphite surfaces are not easily wetted by copper. Evidence suggests that by adding a small amount of chromium to the copper matrix, the fiber/matrix bonding can be significantly improved (DeVincent, 1994a).

Non-uniform fiber distribution has been identified as another problem that may affect the properties and performance of Gr/Cu. For a composite to possess optimal properties, the reinforcement phase should typically be distributed as uniformly as possible. Regions with a low density of inclusions behave more like the matrix material, and they may potentially degrade the overall behavior of the composite. An exception to this rule is the emerging class of functionally graded composites in which the distribution of the reinforcement phase is deliberately tailored for specific applications. Micrographs of the Gr/Cu specimens tested for this investigation revealed that the material may contain large channels of copper with few fibers. Figure 1.2 shows these channels in a Gr/Cu specimen. The current investigation seeks to determine the effects of these copper channels, and non-uniform fiber distribution in general, on the thermal expansion of Gr/Cu. The thermal expansion of this material is important not only because of the large change in temperature it experiences during fabrication, but also because of the hundreds of thermal cycles that it will experience as part of a spacecraft power system or a reentry vehicle.

This thesis outlines the development and implementation of two micromechanical models that were used to investigate the thermal expansion of Gr/Cu composites with non-uniform fiber distribution.

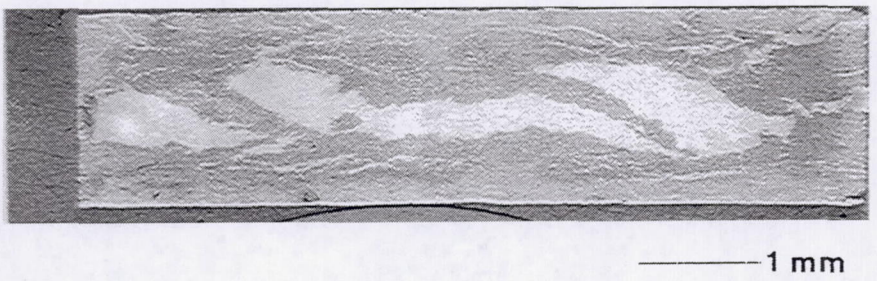

Figure 1.2: Micrograph of a cross-section of a unidirectional Gr/Cu thermal expansion specimen. Note the presence of large copper channels. Courtesy of S.M. DeVincent.

The first model combines elements of the multiple concentric cylinder model (Pindera *et al.*, 1992, 1993) with the method of cells (Aboudi, 1989) to simulate the thermal expansion behavior of composites with a radial variation in fiber distribution. This model will be referred to as CCMICRON. Figure 1.3a shows a composite with radially nonuniform fiber distribution that could be modeled with CCMICRON, and Figure 1.3b illustrates how the microstructure at a point in a cylinder can be modeled with the method of cells. The second model combines elements of the classical lamination theory (Jones, 1975) with the method of cells to allow fiber distribution variation in the through-thickness direction. This model will be referred to as MCLAM. Figure 1.4a shows a composite with fiber distribution that is nonuniform in the through-thickness direction that could be modeled with MCLAM, and Figure 1.4b illustrates how the microstructure at a point in a layer can be modeled with the method of cells.

The method of cells is employed to evaluate the effective properties of each composite cylinder in the case of CCMICRON, and each composite layer in MCLAM. Since the stresses that arise in the composite due to the thermal expansion mismatch between the fiber and matrix phases can cause yielding in the matrix, an inelastic constitutive theory is needed to model the thermal expansion accurately . In both models, the inelastic constitutive theory used is classical incremental plasticity. Classical

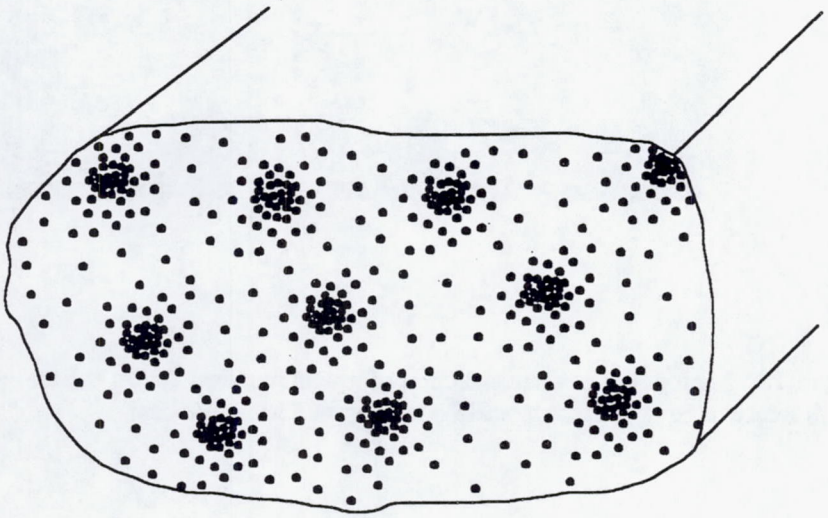

Figure 1.3a: A composite with radially nonuniform fiber distribution.

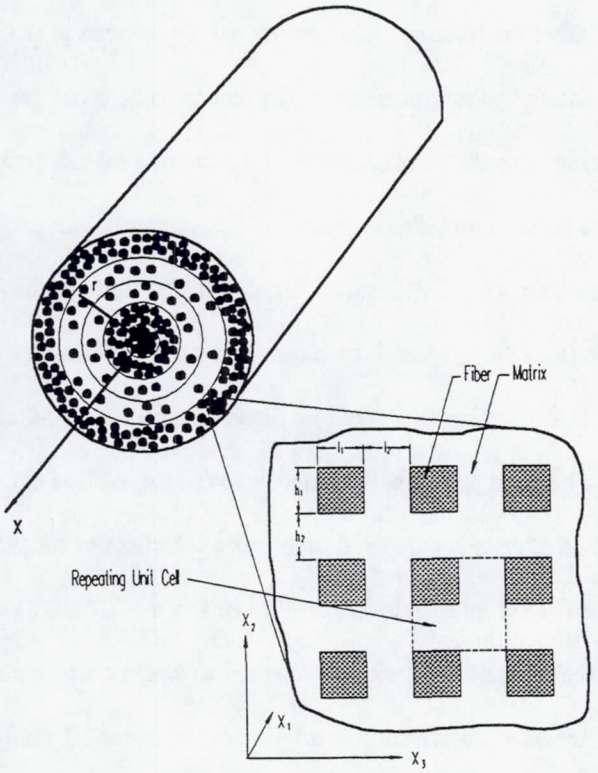

Figure 1.3b: The micro-scale geometry of inhomogeneous cylinders in an assemblage of concentric cylinders represented by the method of cells.

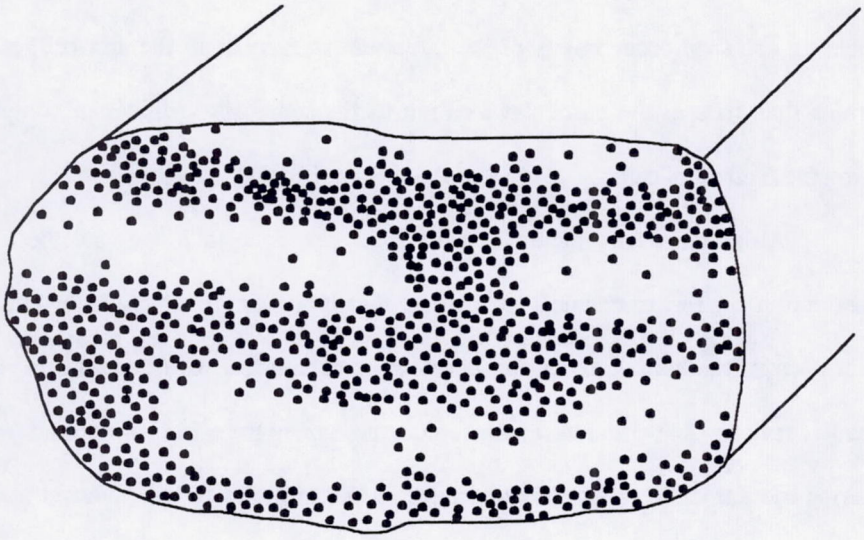

Figure 1.4a: A composite with nonuniform fiber distribution in a Cartesian direction.

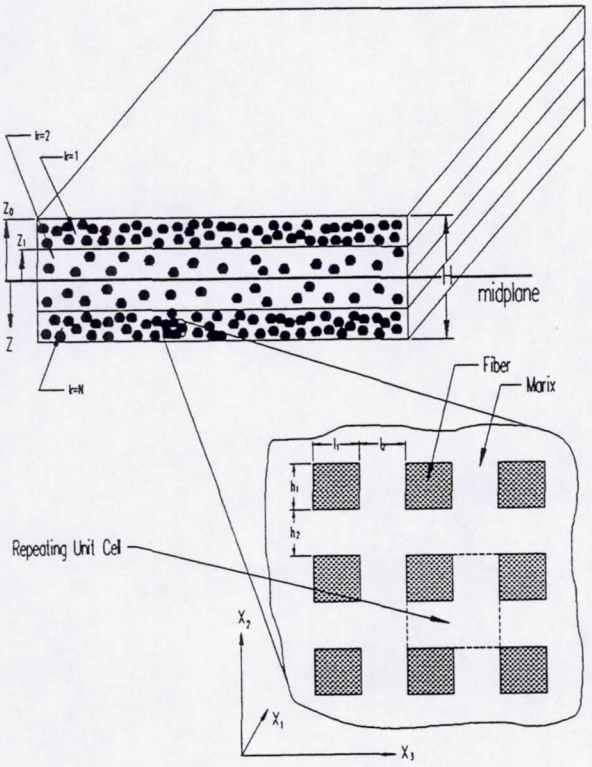

Figure 1.4b: The micro-scale geometry of a laminate represented by the method of cells.

incremental plasticity is employed to model the response of the copper matrix at the micro-level (the subcell level). The strains that arise at a particular location in a composite cylinder or a composite layer are considered to be acting on a repeating unit cell consisting of a fiber subcell and three matrix subcells. Yielding can then occur in any of the three matrix subcells in the unit cell, and if it does, the inelastic strains that arise at the particular location in the composite cylinder or composite layer are calculated using the method of cells.

Although a fair amount of work has been done to investigate the effect of nonuniform fiber distribution on the mechanical properties of composites, relatively little effort has been expended to characterize the thermal expansion behavior of composites with nonuniform microstructures. The next chapter reviews the work done to date on characterizing the effects of nonuniform fiber distribution on the thermo-mechanical response of composites. Most of the work has involved modeling, but several purely experimental investigations also have been conducted. By examining the work that has been done to date on this subject, the justification for the present investigation becomes apparent.

2. Literature Review

2.1 Overview

Much effort has been expended in modeling the thermal and mechanical response of composites during the past 30 years. As an increasing number of factors that affect the response of these materials became apparent, different models were developed that take these factors into account. These factors include anisotropy and temperature-dependent properties of the phases, plasticity of the matrix, inclusion microstructure, imperfect interfacial bonding, complex fiber geometries, and inhomogeneous fiber distribution.

The idea of investigating the effect of the proximity or arrangement of inclusions on the overall composite response while holding the fiber volume fraction constant is not particularly new. In 1967, an elastic finite difference model was used by Adams and Doner (1967a) to investigate transverse normal loading of a unidirectional continuous-fiber composite. A doubly periodic rectangular array of fibers in a matrix was considered, and the shape and volume fraction of the fibers was varied. This model was used again by the same authors to examine longitudinal shear loading of a unidirectional composite (Adams and Doner, 1967b). This latter investigation considered the effect of fiber distribution by modeling the composite as a square array of fibers in the matrix and comparing the resulting predicted composite shear

modulus with the predictions of the composite cylinder assemblage model developed by Hashin and Rosen (1964). It was determined that the square packing arrangement results in a higher shear modulus when the fiber volume fractions of both arrangements are identical. The investigation also pointed out the fact that closely spaced fibers produce high stress concentrations in the matrix.

An early analytical investigation of the effects of different fiber arrangements was performed by Pickett (1968). An elasticity formulation based on the Airy stress function approach was used to determine the composite stiffness matrix for hexagonal and rectangular arrays of continuous unidirectional fibers in an elastic matrix. However, the emphasis was placed on varying the fiber volume fraction and the properties of the fiber; results were not presented for a variation in the packing arrangement with all other relevant parameters held constant.

When continuous fiber composites are modeled, unit cells are usually constructed in the cross-section perpendicular to the long fiber direction. Thus, long cylindrical fibers appeared as circles. For short fiber or whisker composites, it is often preferable to consider a cross-section parallel to the long fiber direction. Thus, short cylinders appear as rectangles. This latter type of cross-section was considered by Chang and Conway (1968). An analytical approach was employed in this investigation. The plane strain elasticity problem was solved for an infinite sheet containing columns of short fibers subjected to normal loading in the fiber direction. The representative volume element (RVE) considered consisted of the rectangle of matrix between two adjacent aligned short fibers. A point-matching technique was used to impose interfacial continuity. The effect of different fiber distributions was examined by varying the aspect ratio of the RVE, but in doing this, the amount of fiber in the RVE changed as well. Thus the effect of the variation in fiber distribution or spacing was not isolated.

Adams (1970) performed a finite-element analysis of unidirectional continuous-fiber composites subjected to transverse normal loading taking into account the elastoplastic response of the matrix until failure. Analysis was performed for square and rectangular arrays of fibers which were modeled using a unit cell consisting of a rectangle of matrix surrounding a single fiber (with appropriate boundary conditions). The rectangular fiber array was oriented such that in the direction of the applied load the fiber spacing was smaller (i.e., shorter sides of rectangle parallel to loading). The results showed that the

stress concentration in the matrix and the transverse stiffness were far greater for the rectangular array than the square array. It was also found that the square array exhibited more matrix yielding than the rectangular array. This is expected since the rectangular array exhibits a higher fiber volume fraction in the loading direction than does the square array.

In recent years, several finite-element investigations have been performed that, like the early work of Adams, take into account fiber distribution by use of different unit cells. Brockenbrough and Suresh (1990) considered fiber shape and fiber packing in continuous fiber composites simultaneously with unit cells representing square edge-packed square fibers, square diagonal-packed square fibers, hexagonally-packed hexagonal fibers, square edge-packed circular fibers, and square diagonal-packed circular fibers using the commercially available finite-element code ABAQUS. The matrix was considered to be elastoplastic. The term "square edge-packed" refers to an array in which the squares (whose corners are the fibers) are aligned such that the edges are parallel to the transverse axes while "square diagonal-packed" refers to the same array rotated 45° with respect to the transverse axes. The results indicated that for axial tension, the packing arrangements have no effect since they are all equivalent in this direction. In response to transverse tension, on the other hand, it was found that for both square and circular fibers, the square diagonal-packed arrangements exhibited lower yield and more plastic flow than the square edge-packed arrangements. This is in agreement with the results of Adams, since in the transverse direction the square-diagonal packed arrangement has greater fiber spacing. The square edge-packing has a higher effective fiber volume fraction in the transverse direction, thus the properties of the fiber are more dominant.

A random distribution of 26 square fibers was also considered by the authors in the same study. The longitudinal response of the random distribution was very close for all of the packing arrangements considered, while the transverse response corresponded most closely to the response of the square edge-packed square fibers. This suggests that square edge-packing best models the response of an actual composite.

In a similar study performed by Brockenbrough *et al.* (1990) using the same finite-element model, the response of square edge, square diagonal, triangular, and random arrays with continuous

circular fibers was investigated. Triangular-packing is equivalent to hexagonal-packing. Elastoplastic stress-strain curves were generated for longitudinal and transverse normal, as well as transverse shear loading. For all packing arrangements the response to longitudinal loading was elastic to failure and very similar. The predicted response of composites with the different packing arrangements to transverse normal and transverse shear loading was presented in the form of elastic modulus, yield stress, and degree of hardening. The square edge-packing arrangement provided the highest values for each of these properties, followed by random packing, triangular-packing, and square diagonal-packing. Again, expected trends were obtained given the fiber spacing in the loading direction. The response of the random fiber distribution arrangements subjected to shear and transverse normal loading lay nearly halfway between the response of the square edge and triangular packing arrangements, but slightly closer to that of the triangular-packing.

In another investigation performed by Nakamura and Suresh (1993) using ABAQUS and the same packing arrangements, more random packing cases were considered, and the analysis was repeated after a cool-down from 520 °C to account for residual stresses. The matrix was treated as elastoplastic. The trends due to fiber packing arrangement were the same as those found by Brockenbrough *et al.* (1990). Transverse composite CTEs were also generated for the different configurations by taking the average of the lateral expansions in the two transverse directions. The transverse CTEs were similar for each packing arrangement, and no trend was apparent. Nakamura and Suresh also presented a single value for the longitudinal CTE and stated that the value was independent of fiber packing arrangement.

Mueller (1994) developed a nonlinear finite-element model to investigate the effect of hexagonal and square packing arrays on the predicted thermo-mechanical properties and the plastic behavior (for transverse normal loading) of continuous boron/aluminum composites. It was found that the packing arrangement did not significantly affect the predicted longitudinal mechanical properties but did significantly affect the predicted transverse mechanical properties. Neither the predicted longitudinal nor transverse CTE was affected by the packing arrangement. Comparison of the plastic behavior of the composite predicted using the two packing arrangements revealed that the square packing arrangement exhibits significantly more hardening than the hexagonal packing arrangement.

A different approach using a finite-element model was taken by Bigelow (1992) to examine the effects of non-uniform fiber distribution. A rectangular packing arrangement of 16 continuous fibers was considered. One fiber was then moved successively closer to one of its neighbors, until the two fibers were touching. The magnitude of each stress component was then examined in the matrix region between the two fibers. It was found that as the space between fibers decreased, each stress component became proportionally greater in this matrix region. It was concluded that the stress concentration in the region was sufficiently large to cause local yielding and fiber-matrix debonding.

Wisnom (1990) used ABAQUS to examine the transverse tensile strength of unidirectional continuous fiber composites using interface failure criteria to account for a weak fiber/matrix bond. The matrix was treated as elastoplastic. One factor considered was the effect of two different packing arrangements, namely rectangular and diamond (which is nearly hexagonal). The method by which the fiber packing arrangement was accounted for was different in this case. Instead of considering two different unit cells, the same unit cell was considered with different boundary conditions to account for the interaction of adjacent fibers. Results indicated that the different packing arrangements did not affect the transverse strength significantly. This conclusion is disputed by Nakamura and Suresh (1993) who observed significant shifts in the post-yield stress-strain response based on packing arrangement.

A finite-element model was also used by Hiemstra and Sottos (1993) to investigate the interaction of four continuous fibers in an infinite matrix subjected to a uniform change in temperature. The spacing among the fibers was varied, and it was found that smaller spacing of the fibers resulted in higher radial and hoop stresses at the interface. Predictions of the location of the onset of microcracking were also made, and they were shown to be consistent with experimental evidence.

Dragone and Nix (1990) addressed the non-uniform inclusion distribution problem using a finite-element model to simulate creep in composites reinforced by long plate-like inclusions. The reinforcing plates were considered to be infinite in one direction and finite in the other two. The load was applied in the infinite plate direction, and power law creep was used to model the response of the matrix. The unit cell, taken from a cross-section of the infinite direction, included eight plate-like inclusions initially aligned in two columns of four. The middle two plate-like inclusions of each column were moved toward

the outside of the unit cell to form new inclusion patterns. The results showed that increased shifting of the plates caused higher stresses and creep in the matrix, while the stresses in the inclusions were highest for the aligned arrangement.

A uniform distribution and two different clustering arrangements of aligned short fibers or whiskers were modeled by Christman *et al.* (1989) using a finite-element approach. The unit cells were taken from the plane parallel to the fiber direction. Normal loading parallel to the whiskers was simulated, and stress-strain curves, hydrostatic stress distributions, and plastic strain distributions were generated. The investigation indicated that higher degrees of clustering result in lower yielding and more plastic flow.

Tvergaard (1990) also considered a unit cell from the plane parallel to the direction of aligned short fibers. In this case the unit cell consisted of one quarter of a fiber and the surrounding matrix that forms a rectangle. A finite-element model was employed to examine the response of short fiber composites subjected to normal loading in the fiber direction. Fiber distribution was taken into account by varying the aspect ratio of the unit cell, and in order to maintain a constant fiber volume fraction, the aspect ratio of the fiber had to be changed as well. Thus as the fiber distribution was changed, the size and shape of the fiber were changed as well. Therefore the effect of the fiber distribution was not isolated in this investigation.

McHugh *et al.* (1993) used a materials science-based approach to investigate the response of a particle reinforced composite. The authors employed an elastic-viscoplastic two-dimensional polycrystal finite-element model based on crystallographic slip theory that considers individual hexagonal grains. The reinforcement phase was introduced by replacing individual matrix grains with reinforcement particles. Thus the inclusion arrangement could be easily altered. Two of the arrangements considered, rectangular and rhombus, had the same inclusion volume fraction The model simulated the application of normal uniform displacement. It was found that the rectangular arrangement produces higher strain concentrations in the matrix near the inclusions. This higher degree of strain concentration allows the strain field in a larger volume of the matrix to be relatively low in magnitude compared to the rhombus arrangement during elastic deformation. Thus the rectangular arrangement provides a stronger constraint

on plastic flow than the rhombus arrangement because a lower volume of the matrix is subjected to concentrated strain.

The Ritz method, which deals with minimizing potential energy, was used by Martin and Leissa (1989) to determine the elastic stress and displacement fields in a unidirectional composite sheet with variable fiber spacing. The fiber volume fraction could be varied as a function of the transverse direction. The case analyzed was a parabolic variation in the fiber content with a high fiber volume fraction in the middle and low fiber volume fraction at the edges of the sheet. Cases with several different boundary conditions were examined. While most of the results presented focus on the convergence of the required numeric integration, it was found that under transverse loading regions with low fiber volume content experience greater displacements.

Pandey and Sherbourne (1993) used potential energy minimization to examine the prebuckling stress fields in composite plates with inhomogeneous fiber distributions, which were introduced by allowing the fiber volume content to vary in the transverse direction. It was found that a parabolic fiber distribution, like that investigated by Martin and Leissa, is an effective way to increase the transverse buckling load of composite plates.

A shear lag analysis was performed by Ochiai and Osamura (1989a) to examine the stress concentration in a continuous-fiber composite plate with non-uniform fiber spacing and broken fibers. The plate modeled consisted of two intact fibers on either side of three broken fibers in an elastoplastic matrix subjected to in-plane shear. The positions of the intact fibers were varied, and the stresses in each fiber were found. It was determined that the stress in the intact fibers was more dependent on the proximity to the broken fibers than the proximity to another intact fiber. Small spaces between the intact fibers and the broken fibers lead to higher stresses in the intact fibers, as did large spaces between adjacent intact fibers.

Ochiai and Osamura (1989b) subsequently used the same model to investigate the tensile strength of a composite plate with non-uniform fiber spacing. In this case, the plate modeled consisted of a repeating pattern of three fibers separated by large spaces followed by three fibers separated by small spaces. The composite was subjected to longitudinal tension, and the strength of each fiber was taken

from statistical data via a Monte Carlo method. The simulation was also performed on a composite plate with the same number of fibers with uniform fiber spacing. Results indicated that due to stress concentration in the regions with small spaces between fibers, the tensile strength of the composite with non-uniform fiber spacing was smaller than the tensile strength of the composite with uniform fiber spacing.

A shear lag model was also used by Karbhari and Wilkins (1991) in an investigation to study fiber-matrix debonding in a unidirectional continuous fiber composite under normal loading in the fiber direction. Concentric cylinder geometry was considered. The formulation included a term to account for the proximity of the nearest neighbor fiber to the one being considered in the concentric cylinder. This term depends not only on the fiber volume fraction, but also on a packing factor. The packing factor can be chosen to simulate different fiber packing arrangements. This investigation considered hexagonal and square packing as well as the cylindrical RVE alone with no interaction from other fibers. The generated results consist of the out-of-plane shear stress at the fiber-matrix interface and the axial stress distribution in the fiber. The effect of the two different packing arrangements was shown to be small, but there was a difference between the two arrangements and the cylinder with no other fiber interaction. The inclusion of the outside fibers in the analysis decreased the interfacial shear stress as well as the longitudinal stress in the fiber. This suggests that interactions from closely situated fibers can have a significant effect on the stress field near the fibers.

In order to examine a different kind of variation in fiber spacing, Pagano and Brown (1993) considered a concentric cylinder assemblage consisting of a fiber embedded in a matrix annulus which was surrounded by composite annuli with 0.2 and 0.6 fiber volume fractions. Thus, the fiber was surrounded by a composite with a fiber volume fraction that increased in a step-wise manner with increasing radius. The interface was permitted to debond and radially propagating annular cracks were introduced. A variational model was employed in which the fiber and matrix were treated as isotropic and elastic to failure. The loading considered was combined uniform radial pressure and a uniform temperature change. It was found that a lower fiber volume fraction near the fiber and the surrounding matrix lead to a higher energy release rate, higher stresses, and thus faster crack propagation.

Pindera and Freed (1992) considered a similar geometric arrangement. The concentric cylinder assemblage model was combined with the method of cells to model unidirectional fibers in an elastic matrix with elastoplastic inclusions. The inclusion volume fraction in the matrix was varied radially from 0.0 at the fiber/matrix interface to 1.0 at the outer radius of the assemblage. The opposite case (high inclusion content near the fiber, low inclusion content in the outer region) was also considered. Results were generated in the form of residual stress distributions in the matrix due to a change in temperature of -1425 °F. It was found that the radial, longitudinal, and hoop stresses were greater for the case of low inclusion volume fraction near the fiber than the opposite case.

There have also been several experimental investigations into the effect of non-uniform fiber distribution. MacKay (1990) used scanning electron microscopy to examine unidirectional Ti-15V-3Cr-3Al-3Sn/SCS 6 SiC composites for microcracks. The microstructure of the composite was such that the fibers were arranged in rows; very closely spaced in one direction, and widely spaced in the other. It was found that microcracks due to cool down from fabrication temperatures were present in the matrix and in the outer layer of the fiber in regions of close fiber spacing. These microcracks are believed to be caused by large hoop stress concentrations in the aforementioned regions due to the close fiber spacing.

Komenda and Henderson (1993) performed creep tests on short alumina fibers in Al - 0.3 Cu matrix. In order to account for scatter in the results, a method to quantify the fiber spacing was developed. A graphical method was used to represent a composite cross-section as fiber-rich zones and fiber-free zones. Then a parameter called the coefficient of variation of fiber-free zone size was defined as the standard deviation in the fiber-free zone size divided by the mean fiber-free zone size. This parameter accounted for the scatter in the creep test results, and proved to be a more important factor than fiber volume fraction alone for composites with fiber volume fractions of 0.1, 0.2, and 0.3.

Tensile tests were performed by Zhenhai *et al.* (1991) on unidirectional composites consisting of bundles of graphite fibers in an aluminum matrix. At failure, the bundles, rather than the individual fibers, pulled out of the matrix, resulting in a higher composite tensile strength than would be the case if individual fibers pulled out. The bundle pull-out occurred because the bundle regions had high strength due to high local fiber volume fraction while the inter-bundle regions had low yield strengths. The

bundles were more difficult to pull out than individual fibers, so the composite strength was greater relative to similar composites with uniformly distributed fibers.

A recent series of papers authored by Rammerstorfer and co-workers deserves special attention. This work, performed in Austria, represents the only in-depth investigation into the effects of non-uniform fiber distribution on the thermal expansion behavior of composites to date. As described below, it is all based on finite-element analysis.

Siegmund *et al.* (1992) considered the thermal expansion behavior of a short fiber metal matrix composite. Temperature-dependent properties were used for both the fiber and the matrix, and the matrix was treated as elastoplastic. A rectangular unit cell consisting of one quarter of a fiber and the surrounding matrix taken from a plane parallel to the long fiber direction (i.e., plane in which short fibers appear as rectangles) was used for the finite-element analysis. Staggered and non-staggered fiber arrays were analyzed separately with constant fiber volume fraction, constant fiber aspect ratio, and variable unit cell aspect ratio. Varying the unit cell aspect ratio corresponds to moving the fibers closer together in one direction and farther apart in the other. It was found that this variation had little effect on the thermal expansion of the staggered arrangement, but in the non-staggered arrangement, larger unit cell aspect ratios (i.e., larger end-to-end spacing of fibers, smaller side-to-side spacing of fibers) lead to a significantly larger amount of thermal expansion. This can be explained by the fact that the staggered array is more isotropic, and the shifting makes less of a difference than in the non-staggered array. In the non-staggered array, the greater aspect ratio leads to a larger area of fiber-free matrix which causes the greater thermal expansion.

Böhm *et al.* (1993) used a similar approach to model a wide range of fiber arrangements with varying degrees of fiber staggering for short fiber metal matrix composites. The results were presented only qualitatively. While the response to axial mechanical loading did not vary significantly with the degree of staggering, the overall thermal expansion behavior did vary significantly. The fact that the thermal expansion of the less staggered arrangements showed significant dependence on unit cell aspect ratio (as was found in the previous investigation) was also mentioned. This investigation also addressed modeling of unidirectional continuous fiber composites. Once again, a finite-element model treating the

matrix as elastoplastic was used, but in this case the unit cells were taken from the plane perpendicular to the fiber direction. A hexagonal array, a square array, three perturbed square arrays, and a clustered square array of fibers were considered. A great deal of numerical and graphical results were presented for each fiber arrangement. The significant result from the stand point of the present investigation is that, as was the case in Nakamura and Suresh (1993), the predicted longitudinal and transverse CTEs for the continuous fiber composites showed little variation with fiber arrangement, and no trend was apparent.

Weissenbek and Rammerstorfer (1993) considered short fibers in staggered and unstaggered arrangements with varying unit cell aspect ratios. As was the case in previous investigations, it was found that the thermal expansion of the staggered arrangement had little dependence on the unit cell aspect ratio, while the unstaggered arrangement showed a large degree of dependence. As the aspect ratio changed, resulting in larger areas void of fibers and larger areas with a high density of fibers, the thermal expansion increased.

Weissenbek *et al.* (1993) examined the thermal response of particulate composites by considering several three-dimensional unit cells with the inclusions in simple cubic, face centered cubic, and base centered cubic arrangements. Cubic, spherical, and cylindrical inclusions were modeled. A finite-element model was used with the matrix treated as elastoplastic. Results indicated that the three particle arrangements considered had no significant effect on the thermal expansion. Thus, this type of inclusion non-uniformity in which packing arrangements are considered is different than shifting short fibers with respect to each other, which was shown in the previous investigations to have a significant effect.

2.2 Role of the Present Investigation

The majority of the investigations discussed in the previous section examine the effect of different periodic fiber arrays on the mechanical properties, stress fields, and yield behavior of composites. Most of the inclusions that were considered were continuous fibers or short fibers. Some of the investigations account for the nonuniformity in the distribution of the fibers by considering random fiber packing arrangements. Some considered a geometry taken from a plane perpendicular to the fiber direction, while others considered a geometry taken from a plane parallel to the fiber direction. Some of the work done in the area is analytical and some is experimental, but most is numerical, based on the finite-element approach. Typically, the investigations revealed that different fiber arrangements do have a significant impact on the quantities being studied. Thus, in general, it can be inferred that nonuniform fiber distribution may be an important factor influencing the response of composites.

Little work has been done to characterize the effect of nonuniform fiber distribution on the thermal expansion of composites. Nakamura and Suresh (1993) presented composite CTEs for different continuous fiber packing arrangements through the use of a finite-element model and found that the fiber packing had no effect. A similar result was published by Mueller (1994). The finite-element investigations by Rammerstorfer and co-workers addressed the thermal expansion of short fiber composites with different periodic fiber arrangements and found the effect of the packing arrangement to be significant. However, when they investigated different fiber packing arrangements in continuous fiber composites, they too found no significant effect (Böhm *et al.*, 1993).

The most important conclusion that follows from the work of Rammerstorfer and co-workers is that regions in a composite with a lower density of inclusions than the overall composite can have a significant effect on the thermal expansion of composites. Thus there is reason to believe that nonuniform fiber distribution can affect the thermal expansion of continuous-fiber composites. A more thorough investigation for continuous-fiber composites thus appears to be warranted. An analytical approach is taken in the current investigation rather than the finite-element approach that has been used previously. Thus the models developed herein can be used in a more efficient manner than those developed previously

to examine similar effects. Furthermore, instead of accounting for fiber distribution through fiber packing arrangements, the present investigation considers macroscopic nonuniform fiber distributions. As will be demonstrated, this approach allows the simulation of the actual microstructures of individual composite specimens. This cannot be done when considering micro-scale packing arrangements.

The model referred to as CCMICRON, developed in this thesis, is similar to the model of Pindera and Freed (1992). It has some additional features, such as thermal cycling capability rather than a monotonic temperature change, and it admits fibers that are transversely isotropic rather than simply isotropic. The model referred to as MCLAM also has these features. Both models are used in this thesis to examine the longitudinal and transverse thermal expansion of unidirectional Gr/Cu composites. The fiber is treated as transversely isotropic and elastic, and the matrix is treated as isotropic and elastoplastic. Both the fiber and the matrix are considered to have temperature-dependent properties. In CCMICRON, the composite is modeled as a cylinder with a step-wise variable fiber volume fraction in the radial direction, while in MCLAM the step-wise fiber volume fraction variation is in the through-thickness direction. Residual stresses from fabrication are accounted for by cooling the composite from an assumed stress-free consolidation temperature before heating it to simulate a thermal expansion test.

In summary, the effect of non-uniform fiber distribution on the thermal expansion of composites has not been thoroughly addressed. The approach taken in the current investigation is different than the previous investigations that addressed the thermal expansion of continuous fiber composites with different fiber packing arrangements (Nakamura and Suresh, 1993; Mueller, 1994; Böhm *et al.*, 1993). Instead of varying the fiber packing arrangement, macro-scale nonuniformity is simulated by allowing the fiber volume fraction to vary in a piece-wise manner in the radial or through-thickness direction. In addition, efficient analytical models are developed in contrast to the finite-element models used previously.

3. Analytical Models

This chapter outlines the development of the multiple concentric cylinder model, inelastic lamination theory, the method of cells, and classical incremental plasticity theory. Section 3.4 describes the procedure through which the method of cells is incorporated into both the concentric cylinder model and lamination theory to produce the computer codes CCMICRON and MCLAM, respectively. Section 3.5 discusses the solution procedure for the models. As discussed in Chapter 1, CCMICRON is capable of modeling the thermal expansion of composites with radially nonuniform fiber distribution (see Figure 1.3). Similarly, MCLAM is capable of modeling the thermal expansion of composites with fiber distribution that is nonuniform in the through-thickness direction (see Figure 1.4).

3.1 Multiple Concentric Cylinder Model

Figure 3.1 illustrates the geometry that is the basis for the multiple concentric cylinder model (Williams and Pindera, 1994b). The core of the assemblage of cylinders is denoted by the subscript or superscript "1" and the outermost shell by "n". An arbitrary shell is denoted by "k" and has inner radius r_{k-1} and outer radius r_k. Traction and displacement components are assigned a "-" superscript at the inner radius and a "+" superscript at the outer radius. The coordinate system is cylindrical with the origin at the center of the assemblage. The displacement components in the coordinate directions (x, θ, r) are, respectively, (u, v, w).

A displacement formulation is used to solve the boundary value problem with time independent plasticity under the assumption of generalized plane strain. For axisymmetric loading, the displacement

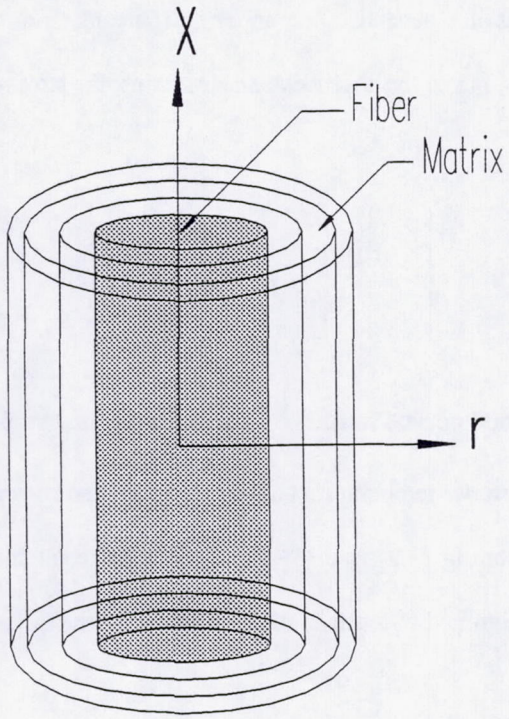

Figure 3.1: Multiple concentric cylinder geometry.

components take the form

$$u = u(x) = \varepsilon_0 x, \quad v = 0, \quad w = w(r) \tag{3.1}$$

where ε_0 is the uniform longitudinal strain throughout the assemblage. Utilizing standard strain-displacement relations yields,

$$\varepsilon_{xx} = \frac{du}{dx} = \varepsilon_0, \quad \varepsilon_{\theta\theta} = \frac{w(r)}{r}, \quad \varepsilon_{rr} = \frac{dw(r)}{dr} \tag{3.2}$$

with the shear strain components identically zero. Applying the equations of equilibrium, recognizing that the stress components, like the strain components, are at most functions of the coordinate r, yields,

$$\frac{d\sigma_{rr}}{dr} + \frac{\sigma_{rr} - \sigma_{\theta\theta}}{r} = 0 \tag{3.3}$$

as the only surviving equation.

It is desired to express the differential equation (3.3) in terms of displacements. To do so stress-strain equations are needed. For an orthotropic material in cylindrical coordinates with thermal and inelastic strains, but in the absence of shear strains, the stress-strain relations are given by,

$$\begin{Bmatrix} \sigma_{xx} \\ \sigma_{\theta\theta} \\ \sigma_{rr} \end{Bmatrix} = \begin{bmatrix} C_{xx} & C_{x\theta} & C_{xr} \\ C_{x\theta} & C_{\theta\theta} & C_{\theta r} \\ C_{xr} & C_{\theta r} & C_{rr} \end{bmatrix} \begin{Bmatrix} \varepsilon_{xx} - \varepsilon_{xx}^p - \alpha_{xx}(T - T_0) \\ \varepsilon_{\theta\theta} - \varepsilon_{\theta\theta}^p - \alpha_{\theta\theta}(T - T_0) \\ \varepsilon_{rr} - \varepsilon_{rr}^p - \alpha_{rr}(T - T_0) \end{Bmatrix} \tag{3.4}$$

where ε_{ii} are total normal strains, ε_{ii}^p are plastic normal strains, and $\alpha_{ii}(T - T_0)$ are thermal strains. T_0 denotes the reference temperature and T represents the current temperature.

Substituting (3.2) into (3.4) and then the result into (3.3), the following governing differential equations are obtained in terms of displacements for the three cases:

Transversely Isotropic, Elastic Layers $\left(C_{x\theta} = C_{xr},\ C_{\theta\theta} = C_{rr},\ \alpha_{\theta\theta} = \alpha_{rr}\right)$

$$\frac{d^2w}{dr^2} + \frac{1}{r}\frac{dw}{dr} - \frac{w}{r^2} = 0 \tag{3.5a}$$

Orthotropic, Elastic Layers

$$\frac{d^2w}{dr^2} + \frac{1}{r}\frac{dw}{dr} - \frac{w}{r^2}\frac{C_{\theta\theta}}{C_{rr}} = \frac{1}{r}\left[\frac{(C_{\theta x} - C_{xr})}{C_{rr}}\varepsilon_0 + \sum_{i=x,\theta,r}\frac{(C_{ri} - C_{\theta i})}{C_{rr}}\alpha_{ii}(T - T_0)\right] \tag{3.5b}$$

Transversely Isotropic, Inelastic Layers

$$\frac{d^2w}{dr^2} + \frac{1}{r}\frac{dw}{dr} - \frac{w}{r^2} = \frac{1}{r}\sum_{i=x,\theta,r}\frac{(C_{ri} - C_{\theta i})}{C_{rr}}\varepsilon_{ii}^p(r) + \frac{d}{dr}\sum_{i=x,\theta,r}\frac{C_{ri}}{C_{rr}}\varepsilon_{ii}^p(r) \tag{3.5c}$$

The plastic strain distribution is assumed to be known at the start of each loading increment.

For thermal loading, there are no tractions on the outside of the assemblage,

$$\sigma_{rr}(r_n) = 0 \tag{3.6}$$

while continuity of interfacial tractions and displacements requires that,

$$u_{k-1}(r_{k-1}) = u_k(r_{k-1}), \qquad \sigma_{rr}^{k-1}(r_{k-1}) = \sigma_{rr}^{k}(r_{k-1}). \tag{3.7}$$

Further, for unconstrained thermal expansion, longitudinal equilibrium across the cross-sectional area of the assemblage, A_c, is satisfied by the condition

$$\int_{A_c}\sigma_{xx}\,dA_c = 0. \tag{3.8}$$

The solutions to the differential equations given in (3.5) are obtained in the form,

Transversely Isotropic, Elastic Layers

$$w(r) = A_1 r + \frac{A_2}{r} \tag{3.9a}$$

Orthotropic, Elastic Layers

$$w(r) = A_1 r^{\lambda} + A_2 r^{-\lambda} + \frac{(C_{\theta x} - C_{rx})}{(C_{rr} - C_{\theta\theta})} r\varepsilon_0 + \sum_{i=x,\theta,r} \frac{(C_{ri} - C_{\theta i})}{(C_{rr} - C_{\theta\theta})} \alpha_{ii} r (T - T_0) \tag{3.9b}$$

where $\lambda = \left(\frac{C_{\theta\theta}}{C_{rr}} \right)^{\frac{1}{2}}$

Transversely Isotropic, Inelastic Layers

$$w(r) = \frac{1}{2r} \int_{r_{k-1}}^{r} \sum_{i=x,\theta,r} \frac{(C_{ri} + C_{\theta i})}{C_{rr}} \varepsilon_{ii}^{p}(r') r' dr' + \frac{r}{2} \int_{r_{k-1}}^{r} \sum_{i=x,\theta,r} \frac{(C_{ri} - C_{\theta i})}{C_{rr}} \varepsilon_{ii}^{p}(r') \frac{dr'}{r'} + \frac{1}{2} \sum_{i=x,\theta,r} \frac{C_{ri}}{C_{rr}} \varepsilon_{ii}^{p}(r_{k-1}) r \left(\frac{r_{k-1}^2}{r^2} - 1 \right) + A_1 r + \frac{A_2}{r} \tag{3.9c}$$

where $r_{k-1} \le r \le r_k$ in the kth layer.

Thus the displacement field is known in terms of two unknown coefficients in each layer, A_1^k and A_2^k, the uniform longitudinal strain, ε_0, and the plastic strain distributions. Since the radial displacement at the center of the assemblage must vanish, A_2^1 must vanish for the solid core. With the use of the boundary, continuity, and longitudinal equilibrium conditions, equations (3.6), (3.7), and (3.8), respectively, the unknown coefficients and ε_0 can be found. In the presence of plasticity, an iterative procedure must be employed since the inelastic strains are dependent upon the unknown coefficients. The procedure developed by Mendelson (1983) is used to accomplish this, as described in Section 3.5.

It is desirable to reformulate the problem using the concept of a local stiffness matrix in order to reduce the number of simultaneous equations in the solution of the prescribed boundary-value problem. This procedure replaces the coefficients A_1^k and A_2^k with the interfacial displacements w_k^- and w_k^+ as the basic unknowns in the system of equations obtained through the application of equations (3.6), (3.7), and (3.8). The replacement entails evaluating w_k^- and w_k^+ using equation (3.9) (i.e., successively substituting r_{k-1} and r_k for r) and solving for A_1^k and A_2^k. The resulting expressions are then used to determine the strains in terms of the interfacial displacements from equation (3.2), and ultimately the interfacial radial stresses, σ_{rr}^- and σ_{rr}^+, from (3.4). The results can be written in the form,

$$\begin{Bmatrix} -\sigma_{rr}^- \\ \sigma_{rr}^+ \end{Bmatrix}^k = \begin{bmatrix} k_{11} & k_{12} \\ k_{21} & k_{22} \end{bmatrix}^k \begin{Bmatrix} w^- \\ w^+ \end{Bmatrix}_k + \begin{Bmatrix} k_{13} \\ k_{23} \end{Bmatrix}^k \varepsilon_0 + \begin{Bmatrix} f_1 \\ f_2 \end{Bmatrix}^k (T - T_0) + \begin{Bmatrix} g_1 \\ g_2 \end{Bmatrix}^k . \tag{3.10}$$

In this expression k_{ij}^k are the components of the local stiffness matrix and are functions of the geometry and temperature-dependent elastic properties of the material. The vector elements f_i^k and g_i^k account for the thermal and plastic effects, respectively. Expressions for these elements for the three types of layers described by (3.9) are given in Appendix A.

Restating the interfacial traction and displacement continuity conditions, (3.7), in the notation of (3.10) yields,

$$\sigma_{rr}^{k+} - \sigma_{rr}^{k+1-} = 0, \qquad k = 1,\ldots,n-1 \tag{3.11}$$

$$w_k = w_k^+ = w_{k+1}^-. \tag{3.12}$$

By applying (3.11) and (3.12) to each interface using (3.10), the following equations arise,

$$(k_{22}^1 + k_{11}^2)w_1 + k_{12}^2 w_2 + (k_{23}^1 + k_{13}^2)\varepsilon_0 = -(f_2^1 + f_1^2)(T - T_0) - (g_2^1 + g_1^2) \tag{3.13}$$

$$k_{21}^k w_{k-1} + (k_{22}^k + k_{11}^{k+1})w_k + k_{12}^{k+1} w_{k+1} + (k_{23}^k + k_{13}^{k+1})\varepsilon_0 = -(f_2^k + f_1^{k+1})(T - T_0) - (g_2^k + g_1^{k+1})$$

$$k_{21}^n w_{n-1} + k_{22}^n w_n + k_{23}^n \varepsilon_0 = -f_2^n (T - T_0) - g_2^n.$$

Note that equation (3.6) and the fact that A_2^1 vanishes have been employed. The remaining equation necessary to determine ε_0 is given by the longitudinal equilibrium condition, (3.8), and it can be expressed as,

$$(\phi_{22}^1 + \phi_{11}^2)w_1 + \ldots + (\phi_{22}^k + \phi_{11}^{k+1})w_k + \ldots + \phi_{22}^n w_n + \sum_{k=1}^{n} \psi_k \varepsilon_0 = -\sum_{k=1}^{n} \Omega_k (T - T_0) - \sum_{k=1}^{n} \Pi_k \tag{3.14}$$

where ϕ_{11}^k, ϕ_{22}^k, ψ_k, Ω_k, and Π_k are given in the Appendix A.

Equations (3.13) and (3.14) can now be used to form the global stiffness matrix equation,

$$\begin{bmatrix} k_{22}^1 + k_{11}^2 & k_{12}^2 & 0 & . & k_{23}^1 + k_{13}^2 \\ k_{21}^2 & k_{22}^2 + k_{11}^3 & k_{12}^3 & . & . \\ 0 & k_{21}^3 & . & . & . \\ . & . & . & k_{22}^n & k_{23}^n \\ \phi_{22}^1 + \phi_{11}^2 & . & . & \phi_{22}^n & \sum \psi_k \end{bmatrix} \begin{Bmatrix} w_1 \\ w_2 \\ . \\ w_n \\ \varepsilon_0 \end{Bmatrix} = -\begin{Bmatrix} f_2^1 + f_1^2 \\ . \\ . \\ f_2^n \\ \sum \Omega_k \end{Bmatrix} (T - T_0) - \begin{Bmatrix} g_2^1 + g_1^2 \\ . \\ . \\ g_2^n \\ \sum \Pi_k \end{Bmatrix} \tag{3.15}$$

The global stiffness matrix can be constructed by superposing the local stiffness matrix of each layer along the matrix diagonal in an overlapping fashion, and then adding a row and a column.

By reformulating the problem using the local global stiffness matrix approach the number of equations that must be solved is reduced by nearly 50% for a large number of concentric cylinders in the assemblage. Additionally, the global stiffness matrix is ideal for computer implementation because of its simple construction for an arbitrary number of layers.

3.2 Lamination Theory

Figure 3.2 illustrates the lamination theory geometry. The 1-2 coordinates refer to the principle material coordinates of a lamina while the x-y coordinates refer to the laminate, as shown in Figure 3.3. Jones (1975) provides a text book derivation of the lamination theory equations without considering inelastic effects. Herein, the lamination theory equations are re-derived taking these effects into account.

Assuming plane stress, the constitutive equations for a lamina in the presence of inelastic strains are:

$$\begin{bmatrix} \sigma_1 \\ \sigma_2 \\ \tau_{12} \end{bmatrix} = \begin{bmatrix} Q_{11}^k & Q_{12}^k & 0 \\ Q_{12}^k & Q_{22}^k & 0 \\ 0 & 0 & Q_{66}^k \end{bmatrix} \begin{bmatrix} \varepsilon_1 - \varepsilon_1^p - \alpha_1^k \Delta T \\ \varepsilon_2 - \varepsilon_2^p - \alpha_2^k \Delta T \\ \gamma_{12} - \gamma_{12}^p \end{bmatrix} \tag{3.16}$$

where Q_{ij}^k are the components of the reduced stiffness matrix for the kth layer and are functions of the

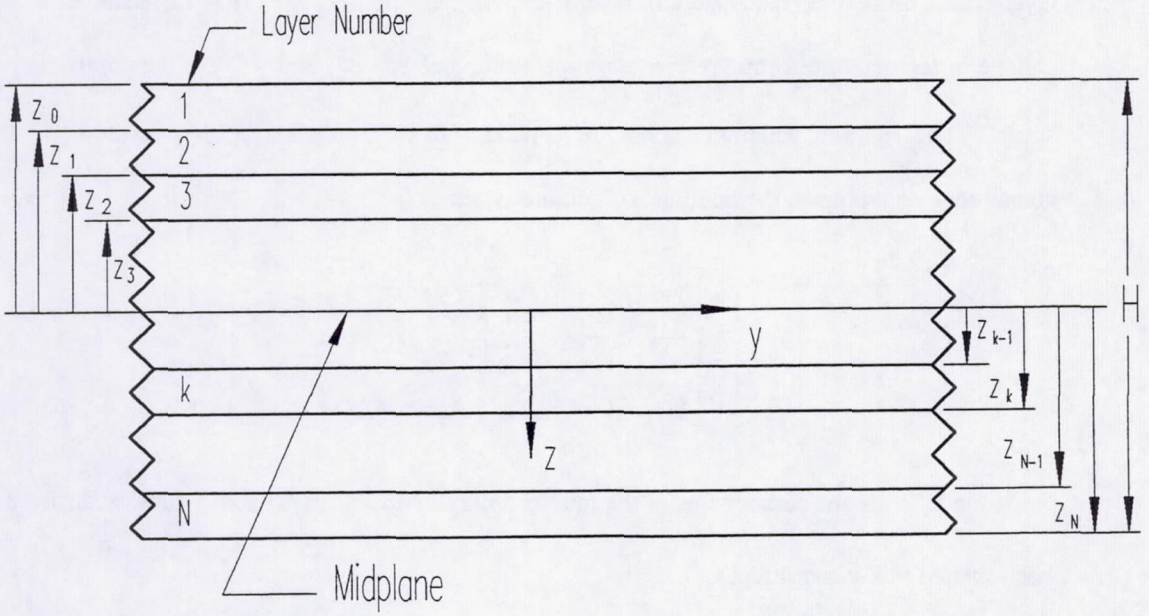

Figure 3.2: Lamination theory geometry.

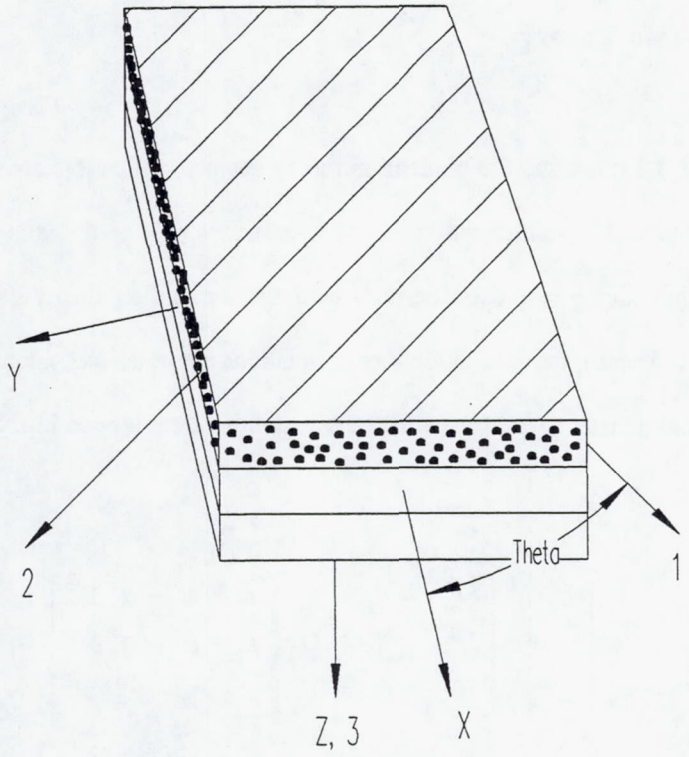

Figure 3.3: The laminate (x-y) and principle material (1-2) coordinates in a laminated composite.

layer elastic properties (see Appendix B for equations), α_1^k and α_2^k are the layer secant CTEs, ΔT is the change in temperature from a reference temperature, and ε_1^p, ε_2^p, and γ_{12}^p are the components of plastic strain. The rotation equations given in Appendix B are applied to (3.16) resulting in the lamina constitutive equations in the laminate coordinate system:

$$\begin{bmatrix} \sigma_x \\ \sigma_y \\ \tau_{xy} \end{bmatrix} = \begin{bmatrix} \overline{Q}_{11}^k & \overline{Q}_{12}^k & \overline{Q}_{16}^k \\ \overline{Q}_{12}^k & \overline{Q}_{22}^k & \overline{Q}_{26}^k \\ \overline{Q}_{16}^k & \overline{Q}_{26}^k & \overline{Q}_{66}^k \end{bmatrix} \begin{bmatrix} \varepsilon_x - \alpha_x^k \Delta T - \varepsilon_x^p \\ \varepsilon_y - \alpha_y^k \Delta T - \varepsilon_y^p \\ \gamma_{xy} - \alpha_{xy}^k \Delta T - \gamma_{xy}^p \end{bmatrix} \tag{3.17}$$

Here, the $\overline{Q}_{ij}^k$ are the components of the rotated reduced stiffness matrix, and each vector from (3.16) has been rotated to x-y coordinates.

According to the Kirchoff-Love hypothesis for plates, a plane cross-section that is originally perpendicular to the midplane of the laminate (an x-y plane) remains planar and perpendicular to the

midplane when the laminate is subjected to bending and extension. This hypothesis leads to the following expressions for the in-plane displacement components, u and v:

$$u = u_0 - z\frac{\partial w_0}{\partial x} \qquad v = v_0 - z\frac{\partial w_0}{\partial y} \tag{3.18}$$

where u_0, v_0, and w_0 are the midplane displacements. Using standard strain-displacement relations, the laminate in-plane strain components are written as

$$\begin{bmatrix} \varepsilon_x \\ \varepsilon_y \\ \gamma_{xy} \end{bmatrix} = \begin{bmatrix} \varepsilon_x^0 \\ \varepsilon_y^0 \\ \gamma_{xy}^0 \end{bmatrix} + z \begin{bmatrix} \kappa_x \\ \kappa_y \\ \kappa_{xy} \end{bmatrix} \tag{3.19}$$

where

$$\begin{bmatrix} \varepsilon_x^0 \\ \varepsilon_y^0 \\ \gamma_{xy}^0 \end{bmatrix} = \begin{bmatrix} \dfrac{\partial u_0}{\partial x} \\ \dfrac{\partial v_0}{\partial y} \\ \dfrac{\partial u_0}{\partial y} + \dfrac{\partial v_0}{\partial x} \end{bmatrix} \qquad \begin{bmatrix} \kappa_x \\ \kappa_y \\ \kappa_{xy} \end{bmatrix} = \begin{bmatrix} \dfrac{\partial^2 w_0}{\partial x^2} \\ \dfrac{\partial^2 w_0}{\partial y^2} \\ 2\dfrac{\partial^2 w_0}{\partial x\,\partial y} \end{bmatrix}. \tag{3.20}$$

ε_x^0, ε_y^0, and γ_{xy}^0 are the midplane strains, and κ_x, κ_y, and κ_{xy} are the midplane curvatures. Combining (3.17) and (3.19) yields

$$\begin{bmatrix} \sigma_x \\ \sigma_y \\ \tau_{xy} \end{bmatrix} = \begin{bmatrix} \overline{Q}_{11}^k & \overline{Q}_{12}^k & \overline{Q}_{16}^k \\ \overline{Q}_{12}^k & \overline{Q}_{22}^k & \overline{Q}_{26}^k \\ \overline{Q}_{16}^k & \overline{Q}_{26}^k & \overline{Q}_{66}^k \end{bmatrix} \left\{ \begin{bmatrix} \varepsilon_x^0 \\ \varepsilon_y^0 \\ \gamma_{xy}^0 \end{bmatrix} + z \begin{bmatrix} \kappa_x \\ \kappa_y \\ \kappa_{xy} \end{bmatrix} + \begin{bmatrix} \alpha_x^k \\ \alpha_y^k \\ \alpha_{xy}^k \end{bmatrix} \Delta T + \begin{bmatrix} \varepsilon_x^p \\ \varepsilon_y^p \\ \gamma_{xy}^p \end{bmatrix} \right\}. \tag{3.21}$$

The resultant laminate forces per unit length (N_x, N_y, and N_{xy}) and moments per unit length (M_x, M_y, and M_{xy}) are obtained by integrating stresses over the laminate thickness H. The integration is performed in a piecewise manner across each layer as indicated below.

$$\begin{bmatrix} N_x \\ N_y \\ N_{xy} \end{bmatrix} = \int_{\frac{-H}{2}}^{\frac{H}{2}} \begin{bmatrix} \sigma_x \\ \sigma_y \\ \tau_{xy} \end{bmatrix} dz = \sum_{k=1}^{N} \int_{z_{k-1}}^{z_k} \begin{bmatrix} \sigma_x \\ \sigma_y \\ \tau_{xy} \end{bmatrix} dz \tag{3.22}$$

$$\begin{bmatrix} M_x \\ M_y \\ M_{xy} \end{bmatrix} = \int_{\frac{-H}{2}}^{\frac{H}{2}} \begin{bmatrix} \sigma_x \\ \sigma_y \\ \tau_{xy} \end{bmatrix} z dz = \sum_{k=1}^{N} \int_{z_{k-1}}^{z_k} \begin{bmatrix} \sigma_x \\ \sigma_y \\ \tau_{xy} \end{bmatrix} z dz \tag{3.23}$$

Substituting (3.21) into (3.22) and (3.23) yields,

$$\begin{bmatrix} N_x \\ N_y \\ N_{xy} \end{bmatrix} = \sum_{k=1}^{N} \begin{bmatrix} \overline{Q}_{11}^k & \overline{Q}_{12}^k & \overline{Q}_{16}^k \\ \overline{Q}_{12}^k & \overline{Q}_{22}^k & \overline{Q}_{26}^k \\ \overline{Q}_{16}^k & \overline{Q}_{26}^k & \overline{Q}_{66}^k \end{bmatrix} \left\{ \int_{z_{k-1}}^{z_k} \begin{bmatrix} \varepsilon_x^0 \\ \varepsilon_y^0 \\ \gamma_{xy}^0 \end{bmatrix} dz + \int_{z_{k-1}}^{z_k} \begin{bmatrix} \kappa_x \\ \kappa_y \\ \kappa_{xy} \end{bmatrix} z dz + \int_{z_{k-1}}^{z_k} \begin{bmatrix} \alpha_x^k \\ \alpha_y^k \\ \alpha_{xy}^k \end{bmatrix} \Delta T dz + \int_{z_{k-1}}^{z_k} \begin{bmatrix} \varepsilon_x^p \\ \varepsilon_y^p \\ \gamma_{xy}^p \end{bmatrix} dz \right\} \tag{3.24}$$

$$\begin{bmatrix} M_x \\ M_y \\ M_{xy} \end{bmatrix} = \sum_{k=1}^{N} \begin{bmatrix} \overline{Q}_{11}^k & \overline{Q}_{12}^k & \overline{Q}_{16}^k \\ \overline{Q}_{12}^k & \overline{Q}_{22}^k & \overline{Q}_{26}^k \\ \overline{Q}_{16}^k & \overline{Q}_{26}^k & \overline{Q}_{66}^k \end{bmatrix} \left\{ \int_{z_{k-1}}^{z_k} \begin{bmatrix} \varepsilon_x^0 \\ \varepsilon_y^0 \\ \gamma_{xy}^0 \end{bmatrix} z dz + \int_{z_{k-1}}^{z_k} \begin{bmatrix} \kappa_x \\ \kappa_y \\ \kappa_{xy} \end{bmatrix} z^2 dz + \int_{z_{k-1}}^{z_k} \begin{bmatrix} \alpha_x^k \\ \alpha_y^k \\ \alpha_{xy}^k \end{bmatrix} \Delta T z dz + \int_{z_{k-1}}^{z_k} \begin{bmatrix} \varepsilon_x^p \\ \varepsilon_y^p \\ \gamma_{xy}^p \end{bmatrix} z dz \right\} \tag{3.25}$$

Recognizing that the midplane strains, midplane curvatures, and lamina CTEs are independent of z, the following definitions are introduced:

$$\begin{bmatrix} A_{11} & A_{12} & A_{16} \\ A_{12} & A_{22} & A_{26} \\ A_{16} & A_{26} & A_{66} \end{bmatrix} = \sum_{k=1}^{N} \begin{bmatrix} \overline{Q}_{11}^k & \overline{Q}_{12}^k & \overline{Q}_{16}^k \\ \overline{Q}_{12}^k & \overline{Q}_{22}^k & \overline{Q}_{26}^k \\ \overline{Q}_{16}^k & \overline{Q}_{26}^k & \overline{Q}_{66}^k \end{bmatrix} \left(z_k - z_{k-1} \right) \tag{3.26}$$

$$\begin{bmatrix} B_{11} & B_{12} & B_{16} \\ B_{12} & B_{22} & B_{26} \\ B_{16} & B_{26} & B_{66} \end{bmatrix} = \sum_{k=1}^{N} \begin{bmatrix} \overline{Q}_{11}^k & \overline{Q}_{12}^k & \overline{Q}_{16}^k \\ \overline{Q}_{12}^k & \overline{Q}_{22}^k & \overline{Q}_{26}^k \\ \overline{Q}_{16}^k & \overline{Q}_{26}^k & \overline{Q}_{66}^k \end{bmatrix} \left(z_k^2 - z_{k-1}^2 \right) \tag{3.27}$$

$$\begin{bmatrix} D_{11} & D_{12} & D_{16} \\ D_{12} & D_{22} & D_{26} \\ D_{16} & D_{26} & D_{66} \end{bmatrix} = \sum_{k=1}^{N} \begin{bmatrix} \overline{Q}_{11}^k & \overline{Q}_{12}^k & \overline{Q}_{16}^k \\ \overline{Q}_{12}^k & \overline{Q}_{22}^k & \overline{Q}_{26}^k \\ \overline{Q}_{16}^k & \overline{Q}_{26}^k & \overline{Q}_{66}^k \end{bmatrix} \left(z_k^3 - z_{k-1}^3 \right) \tag{3.28}$$

where the matrix $\underline{A}$ is called the extensional stiffness, $\underline{B}$ is called the coupling stiffness, and $\underline{D}$ is called the bending stiffness. Additionally,

$$\begin{bmatrix} N_x^T \\ N_y^T \\ N_{xy}^T \end{bmatrix} = \sum_{k=1}^{N} \begin{bmatrix} \overline{Q}_{11}^k & \overline{Q}_{12}^k & \overline{Q}_{16}^k \\ \overline{Q}_{12}^k & \overline{Q}_{22}^k & \overline{Q}_{26}^k \\ \overline{Q}_{16}^k & \overline{Q}_{26}^k & \overline{Q}_{66}^k \end{bmatrix} \begin{bmatrix} \alpha_x^k \\ \alpha_y^k \\ \alpha_{xy}^k \end{bmatrix} \Delta T \left(z_k - z_{k-1} \right) \tag{3.29}$$

$$\begin{bmatrix} M_x^T \\ M_y^T \\ M_{xy}^T \end{bmatrix} = \sum_{k=1}^{N} \begin{bmatrix} \overline{Q}_{11}^k & \overline{Q}_{12}^k & \overline{Q}_{16}^k \\ \overline{Q}_{12}^k & \overline{Q}_{22}^k & \overline{Q}_{26}^k \\ \overline{Q}_{16}^k & \overline{Q}_{26}^k & \overline{Q}_{66}^k \end{bmatrix} \begin{bmatrix} \alpha_x^k \\ \alpha_y^k \\ \alpha_{xy}^k \end{bmatrix} \Delta T \left(z_k^2 - z_{k-1}^2 \right) \tag{3.30}$$

$$\begin{bmatrix} N_x^p \\ N_y^p \\ N_{xy}^p \end{bmatrix} = \sum_{k=1}^{N} \begin{bmatrix} \overline{Q}_{11}^k & \overline{Q}_{12}^k & \overline{Q}_{16}^k \\ \overline{Q}_{12}^k & \overline{Q}_{22}^k & \overline{Q}_{26}^k \\ \overline{Q}_{16}^k & \overline{Q}_{26}^k & \overline{Q}_{66}^k \end{bmatrix} \int_{z_{k-1}}^{z_k} \begin{bmatrix} \varepsilon_x^p \\ \varepsilon_y^p \\ \gamma_{xy}^p \end{bmatrix} \left(z_k - z_{k-1} \right) dz \tag{3.31}$$

$$\begin{bmatrix} M_x^p \\ M_y^p \\ M_{xy}^p \end{bmatrix} = \sum_{k=1}^{N} \begin{bmatrix} \overline{Q}_{11}^k & \overline{Q}_{12}^k & \overline{Q}_{16}^k \\ \overline{Q}_{12}^k & \overline{Q}_{22}^k & \overline{Q}_{26}^k \\ \overline{Q}_{16}^k & \overline{Q}_{26}^k & \overline{Q}_{66}^k \end{bmatrix} \int_{z_{k-1}}^{z_k} \begin{bmatrix} \varepsilon_x^p \\ \varepsilon_y^p \\ \gamma_{xy}^p \end{bmatrix} \left(z_k^2 - z_{k-1}^2 \right) dz \tag{3.32}$$

where $\left[N^T \right]$ and $\left[M^T \right]$ are the thermal force and moment vectors, and $\left[N^p \right]$ and $\left[M^p \right]$ are the plastic force and moment vectors. Note that the plastic strains are dependent on z, and thus the integrals in (3.31) and (3.32) cannot be solved a priori.

Using the above definitions, equations (3.24) and (3.25) can be written as

$$\begin{bmatrix} N_x + N_x^T + N_x^P \\ N_y + N_y^T + N_y^P \\ N_{xy} + N_{xy}^T + N_{xy}^P \\ M_x + M_x^T + M_x^P \\ M_y + M_y^T + M_y^P \\ M_{xy} + M_{xy}^T + M_{xy}^P \end{bmatrix} = \begin{bmatrix} A_{11} & A_{12} & A_{16} & B_{11} & B_{12} & B_{16} \\ A_{12} & A_{22} & A_{26} & B_{12} & B_{22} & B_{26} \\ A_{16} & A_{26} & A_{66} & B_{16} & B_{26} & B_{66} \\ B_{11} & B_{12} & B_{16} & D_{11} & D_{12} & D_{16} \\ B_{12} & B_{22} & B_{26} & D_{12} & D_{22} & D_{26} \\ B_{16} & B_{26} & B_{66} & D_{16} & D_{26} & D_{66} \end{bmatrix} \begin{bmatrix} \varepsilon_x^0 \\ \varepsilon_y^0 \\ \gamma_{xy}^0 \\ \kappa_x \\ \kappa_y \\ \kappa_{xy} \end{bmatrix}. \tag{3.33}$$

In order to determine the out-of-plane strain, ε_z, the out-of-plane stress, σ_z, is set to zero, and the standard constitutive equation is used to yield,

$$\varepsilon_z = \frac{-\overline{C}_{13}^k}{\overline{C}_{33}^k}\left(\varepsilon_x - \alpha_x^k \Delta T - \varepsilon_x^p\right) - \frac{\overline{C}_{23}^k}{\overline{C}_{33}^k}\left(\varepsilon_y - \alpha_y^k \Delta T - \varepsilon_y^p\right) - \frac{\overline{C}_{36}^k}{\overline{C}_{33}^k}\left(\gamma_{xy} - \alpha_{xy}^k \Delta T - \gamma_{xy}^p\right) + \alpha_z^k \Delta T + \varepsilon_z^p \tag{3.34}$$

where $\overline{C}_{ij}^k$ are rotated stiffness matrix components in the kth layer, and $\alpha_z^k = \alpha_2^k$ for transversely isotropic layers.

The six-by-six matrix in (3.33) is referred to as the ABD matrix or the laminate stiffness matrix. This equation is the key to lamination theory. If the loading applied to the laminate and the plastic strains are known, the laminate stiffness matrix is inverted, and the midplane strains and curvatures are calculated. Then using (3.19), the strains at every point in the laminate are calculated, and from (3.21), the stresses can be calculated as well. The solution procedure in the presence of plastic effects is discussed in Section 3.5.

3.3 The Method of Cells

The method of cells, developed by Aboudi (1989), is based on the representation of a doubly periodic array of infinitely long fibers in a matrix by the geometry shown in Figures 3.4. The basic building block of this doubly periodic array of fibers in a matrix, the repeating unit cell, is shown in Figure 3.5. The four individual subcells that make up the unit cell are denoted by $(\beta\gamma)$= (11), (12), (21), or (22). Each subcell has a local Cartesian coordinate system denoted by $x_1, \bar{x}_2^{(\beta)}, \bar{x}_3^{(\gamma)}$.

The subcell displacement components are represented by a first order Taylor series expansion in $\bar{x}_2^{(\beta)}, \bar{x}_3^{(\gamma)}$,

$$u_i^{(\beta\gamma)} = w_i^{(\beta\gamma)} + \bar{x}_2^{(\beta)}\,\phi_i^{(\beta\gamma)} + \bar{x}_3^{(\gamma)}\,\psi_i^{(\beta\gamma)} \qquad i = 1,2,3 \tag{3.35}$$

where $w_i^{(\beta\gamma)}$ are the displacement components of the center of the subcell, and the microvariables $\phi_i^{(\beta\gamma)}$ and $\psi_i^{(\beta\gamma)}$ represent the dependence of the subcell displacements on the local coordinates. In order to

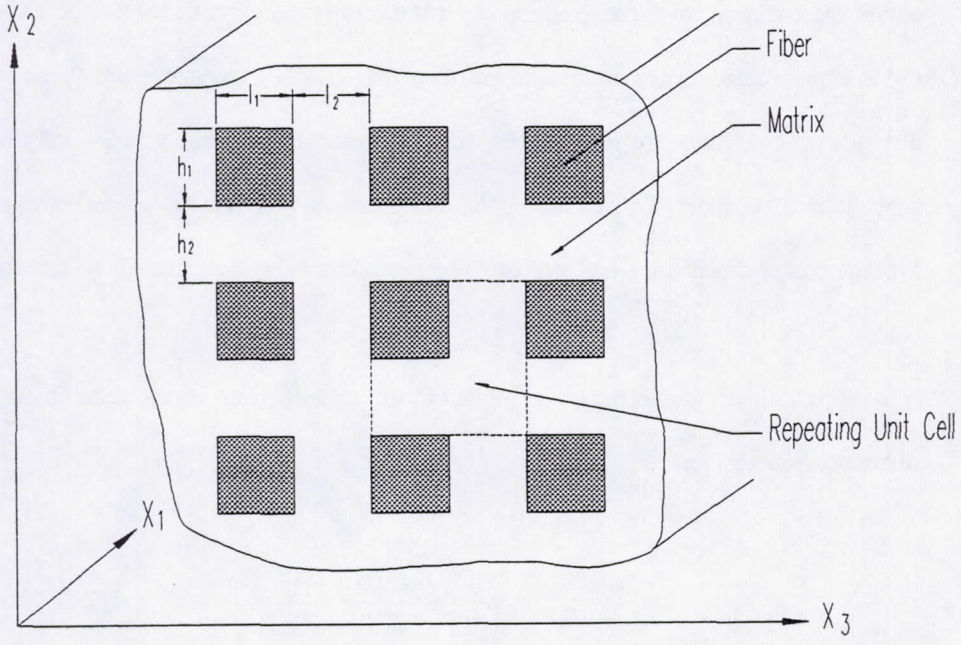

Figure 3.4: Method of cells geometry: doubly periodic array of square fibers in the matrix.

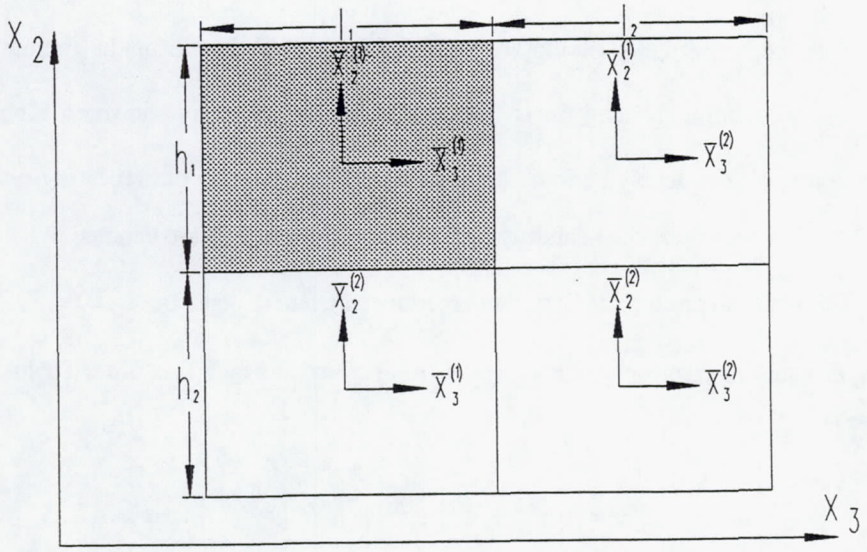

Figure 3.5: Method of cells geometry: the repeating unit cell.

obtain the effective constitutive equation for the composite, expressions for the microvariables in terms of the average strains of the composite are required. These expressions are found with the use of strain-displacement relations for the subcells, subcell constitutive equations, continuity conditions between the subcells and between adjacent unit cells, and relations between the subcell stresses and strains and the average composite stresses and strains. The procedure for generating all the required relations is outlined below.

The microvariables can be related to the subcell strain components through the standard strain-displacement relations:

$$\varepsilon_{ij}^{(\beta\gamma)} = \frac{1}{2}\left(\frac{\partial u_i^{(\beta\gamma)}}{\partial \overline{x}_j^{(\bullet)}} + \frac{\partial u_j^{(\beta\gamma)}}{\partial \overline{x}_i^{(\bullet)}} \right) \qquad i = 1,2,3. \tag{3.36}$$

Continuity of interfacial displacements between the four subcells within the unit cell requires that

$$u_i^{(1\gamma)}\Big|_{\bar{x}_2^{(1)}=\frac{-h_1}{2}} = u_i^{(2\gamma)}\Big|_{\bar{x}_2^{(2)}=\frac{h_2}{2}} \tag{3.37}$$

and,

$$u_i^{(\beta 1)}\Big|_{\bar{x}_3^{(1)}=\frac{l_1}{2}} = u_i^{(\beta 2)}\Big|_{\bar{x}_3^{(2)}=\frac{-l_2}{2}}. \tag{3.38}$$

These continuity conditions are applied in an average sense; the integrals of the displacement components along the boundary are required to be continuous. Thus,

$$\int_{\frac{-l_\gamma}{2}}^{\frac{l_\gamma}{2}} \left(u_i^{(1\gamma)}\Big|_{\bar{x}_2^{(1)}=\frac{-h_1}{2}} - u_i^{(2\gamma)}\Big|_{\bar{x}_2^{(2)}=\frac{h_2}{2}} \right) d\bar{x}_3^{(\gamma)} = 0 \tag{3.39}$$

and,

$$\int_{\frac{-h_\beta}{2}}^{\frac{h_\beta}{2}} \left(u_i^{(\beta 1)}\Big|_{\bar{x}_3^{(1)}=\frac{l_1}{2}} = u_i^{(\beta 2)}\Big|_{\bar{x}_3^{(2)}=\frac{-l_2}{2}} \right) d\bar{x}_2^{(\beta)} = 0. \tag{3.40}$$

Substituting for $u_i^{(\beta\gamma)}$ in (3.39) and (3.40) with (3.35), and performing the integration yields,

$$w_i^{(1\gamma)} - \frac{h_1}{2}\phi_i^{(1\gamma)} = w_i^{(2\gamma)} + h_2\,\phi_i^{(2\gamma)} \tag{3.41}$$

and,

$$w_i^{(\beta 1)} + \frac{l_1}{2}\psi_i^{(\beta 1)} = w_i^{(\beta 2)} - l_2\,\psi_i^{(\beta 2)}. \tag{3.42}$$

Continuity between adjacent cells is also required. Considering first the x_2-direction yields,

$$u_i^{(1\gamma)}\Big|_{\bar{x}_2^{(1)}=\frac{h_1}{2}}\Big|_{below} = u_i^{(2\gamma)}\Big|_{\bar{x}_2^{(2)}=\frac{-h_2}{2}} \tag{3.43}$$

and,

$$u_i^{(1\gamma)}\Big|_{\bar{x}_2^{(1)}=\frac{h_1}{2}} = u_i^{(2\gamma)}\Big|_{\bar{x}_2^{(2)}=\frac{-h_2}{2}}\Big|_{above} \tag{3.44}$$

where "above" and "below" refer to the adjacent cells. Applying these conditions in an average sense, substituting with (3.35), and integrating yields,

$$w_i^{(1\gamma)} + \frac{h_1}{2}\phi_i^{(1\gamma)}\Big|_{below} = w_i^{(2\gamma)} - \frac{h_2}{2}\phi_i^{(2\gamma)} \tag{3.45}$$

and,

$$w_i^{(1\gamma)} + \frac{h_1}{2}\phi_i^{(1\gamma)} = w_i^{(2\gamma)} - \frac{h_2}{2}\phi_i^{(2\gamma)}\Big|_{above}. \tag{3.46}$$

The quantities from the cells above and below are represented using a Taylor series expansion of the form

$$f(x_0+\Delta x) = f(x_0) + \frac{\partial f}{\partial x}\Big|_{x_0}\Delta x + \frac{\partial^2 f}{\partial x^2}\Big|_{x_0}\Delta x^2 + \ldots \tag{3.47}$$

Retaining only terms up to the first order in the cell dimension h_β in equation (3.45) yields,

$$w_i^{(1\gamma)} - (h_1+h_2)\frac{\partial w_i^{(1\gamma)}}{\partial x_2} + \frac{h_1}{2}\phi_i^{(1\gamma)} = w_i^{(2\gamma)} - \frac{h_2}{2}\phi_i^{(2\gamma)}. \tag{3.48}$$

Similarly, equation (3.46) becomes,

$$w_i^{(1\gamma)} + \frac{h_1}{2}\phi_i^{(1\gamma)} = w_i^{(2\gamma)} + (h_1+h_2)\frac{\partial w_i^{(2\gamma)}}{\partial x_2} - \frac{h_2}{2}\phi_i^{(2\gamma)} \tag{3.49}$$

Subtracting (3.49) from (3.48) yields,

$$\frac{\partial w_i^{(1\gamma)}}{\partial x_2} = \frac{\partial w_i^{(2\gamma)}}{\partial x_2}. \tag{3.50}$$

and subtracting (3.49) from (3.38) yields,

$$h_1\phi_i^{(1\gamma)} + h_2\phi_i^{(2\gamma)} = (h_1 + h_2)\frac{\partial w_i^{(2\gamma)}}{\partial x_2}. \tag{3.51}$$

A similar application of displacement continuity between cells in the x_3-direction yields,

$$\frac{\partial w_i^{(\beta 1)}}{\partial x_3} = \frac{\partial w_i^{(\beta 2)}}{\partial x_3} \tag{3.52}$$

and,

$$l_1\psi_1^{(\beta 1)} + l_2\psi_2^{(\beta 2)} = (l_1 + l_2)\frac{\partial w_i^{(\beta 2)}}{\partial x_3}. \tag{3.53}$$

Requiring $\varepsilon_{11}^{(\beta\gamma)}$ to be uniform in the cell and using (3.36) yields,

$$\frac{\partial w_1^{(11)}}{\partial x_1} = \frac{\partial w_1^{(12)}}{\partial x_1} = \frac{\partial w_1^{(21)}}{\partial x_1} = \frac{\partial w_1^{(22)}}{\partial x_1}. \tag{3.54}$$

The conditions of (3.50), (3.52), and (3.54) can be satisfied by requiring

$$w_i^{(11)} = w_i^{(12)} = w_i^{(21)} = w_i^{(22)} = w_i. \tag{3.55}$$

The average strain components in the composite are given by

$$\bar{\varepsilon}_{ij} = \frac{1}{V}\sum_{\beta,\gamma=1}^{2} V_{\beta\gamma}\,\varepsilon_{ij}^{(\beta\gamma)} \tag{3.56}$$

where $V_{\beta\gamma} = h_\beta l_\gamma$ and $V = (h_1 + h_2)(l_1 + l_2)$. Substituting using (3.36), (3.51), (3.53), and (3.55) yields

$$\bar{\varepsilon}_{ij} = \frac{1}{2}\left(\frac{\partial w_i}{\partial x_j} + \frac{\partial w_j}{\partial x_i}\right) \tag{3.57}$$

This expression relates the gradients of the subcell center displacements to average cell strains. It will be used to relate the subcell strains to the average cell strains.

The total strain components in the subcells are represented as the sum of the elastic (e), plastic (p), and thermal (T) strains,

$$\varepsilon_{ij}^{(\beta\gamma)} = \varepsilon_{ij}^{e\,(\beta\gamma)} + \varepsilon_{ij}^{p(\beta\gamma)} + \varepsilon_{ij}^{T(\beta\gamma)}. \tag{3.58}$$

The subcell constitutive equations are used to relate the subcell stresses and strains. For transversely isotropic constituents with 2-3 isotropy they are given by

$$\begin{bmatrix} \sigma_{11}^{(\beta\gamma)} \\ \sigma_{22}^{(\beta\gamma)} \\ \sigma_{33}^{(\beta\gamma)} \\ \sigma_{12}^{(\beta\gamma)} \\ \sigma_{13}^{(\beta\gamma)} \\ \sigma_{23}^{(\beta\gamma)} \end{bmatrix} = \begin{bmatrix} C_{11}^{(\beta\gamma)} & C_{12}^{(\beta\gamma)} & C_{12}^{(\beta\gamma)} & 0 & 0 & 0 \\ C_{12}^{(\beta\gamma)} & C_{22}^{(\beta\gamma)} & C_{23}^{(\beta\gamma)} & 0 & 0 & 0 \\ C_{12}^{(\beta\gamma)} & C_{23}^{(\beta\gamma)} & C_{22}^{(\beta\gamma)} & 0 & 0 & 0 \\ 0 & 0 & 0 & C_{44}^{(\beta\gamma)} & 0 & 0 \\ 0 & 0 & 0 & 0 & C_{44}^{(\beta\gamma)} & 0 \\ 0 & 0 & 0 & 0 & 0 & C_{66}^{(\beta\gamma)} \end{bmatrix} \begin{bmatrix} \varepsilon_{11}^{e\,(\beta\gamma)} \\ \varepsilon_{22}^{e\,(\beta\gamma)} \\ \varepsilon_{33}^{e\,(\beta\gamma)} \\ 2\,\varepsilon_{12}^{e\,(\beta\gamma)} \\ 2\,\varepsilon_{13}^{e\,(\beta\gamma)} \\ 2\,\varepsilon_{23}^{e\,(\beta\gamma)} \end{bmatrix} \tag{3.59}$$

where $C_{66}^{(\beta\gamma)} = \frac{1}{2}(C_{22}^{(\beta\gamma)} - C_{23}^{(\beta\gamma)})$. Note that the shear strains, $\varepsilon_{ij}^{e\,(\beta\gamma)}$ $(i \neq j)$, are tensorial quantities.

The average stress components in the composite are given by

$$\overline{\sigma}_{ij} = \frac{1}{V} \sum_{\beta,\gamma=1}^{2} V_{\beta\gamma}\, S_{ij}^{(\beta\gamma)} \tag{3.60}$$

where $S_{ij}^{(\beta\gamma)}$ are the average subcell stresses, given by

$$S_{ij}^{(\beta\gamma)} = \frac{1}{V} \int_{-h_\beta/2}^{h_\beta/2} \int_{-l_\gamma/2}^{l_\gamma/2} \sigma_{ij}^{(\beta\gamma)}\, d\overline{x}_2^{(\beta)}\, d\overline{x}_3^{(\gamma)}. \tag{3.61}$$

However, from (3.36) and (3.55) it is clear that the subcell strain components are independent of $\overline{x}_2^{(\beta)}$ and $\overline{x}_3^{(\gamma)}$. Then from (3.59), $\sigma_{ij}^{(\beta\gamma)}$ are independent of $\overline{x}_2^{(\beta)}$ and $\overline{x}_3^{(\gamma)}$ as well, and (3.61) reduces to,

$$S_{ij}^{(\beta\gamma)} = \sigma_{ij}^{(\beta\gamma)}. \tag{3.62}$$

Equations (3.60) and (3.62) will be used to relate the subcell stresses and the average cell stresses. Substituting (3.37) into (3.62) and using (3.36), (3.54), (3.55), and (3.57), as well as the condition of incompressibility of plastic deformation,

$$\varepsilon_{11}^{p\,(\beta\gamma)} + \varepsilon_{22}^{p\,(\beta\gamma)} + \varepsilon_{33}^{p\,(\beta\gamma)} = 0 \tag{3.63}$$

the following relations are obtained:

$$S_{11}^{(\beta\gamma)} = C_{11}^{(\beta\gamma)}\,\bar{\varepsilon}_{11} + C_{12}^{(\beta\gamma)}\left(\phi_2^{(\beta\gamma)} + \psi_3^{(\beta\gamma)}\right) - \left(C_{11}^{(\beta\gamma)}\alpha_1^{(\beta\gamma)} + 2\,C_{12}^{(\beta\gamma)}\alpha_2^{(\beta\gamma)}\right)\Delta T - \left(C_{11}^{(\beta\gamma)} - C_{12}^{(\beta\gamma)}\right)\varepsilon_{11}^{p\,(\beta\gamma)}$$

$$S_{22}^{(\beta\gamma)} = C_{12}^{(\beta\gamma)}\,\bar{\varepsilon}_{11} + C_{22}^{(\beta\gamma)}\,\phi_2^{(\beta\gamma)} + C_{23}^{(\beta\gamma)}\,\psi_3^{(\beta\gamma)} - \left[C_{12}^{(\beta\gamma)}\alpha_1^{(\beta\gamma)} + \left(C_{22}^{(\beta\gamma)} + C_{23}^{(\beta\gamma)}\right)\alpha_2^{(\beta\gamma)}\right]\Delta T - \left(C_{11}^{(\beta\gamma)} - C_{12}^{(\beta\gamma)}\right)\varepsilon_{22}^{p\,(\beta\gamma)}$$

$$S_{33}^{(\beta\gamma)} = C_{12}^{(\beta\gamma)}\,\bar{\varepsilon}_{11} + C_{23}^{(\beta\gamma)}\,\phi_2^{(\beta\gamma)} + C_{22}^{(\beta\gamma)}\,\psi_3^{(\beta\gamma)} - \left[C_{12}^{(\beta\gamma)}\alpha_1^{(\beta\gamma)} + \left(C_{22}^{(\beta\gamma)} + C_{23}^{(\beta\gamma)}\right)\alpha_2^{(\beta\gamma)}\right]\Delta T - \left(C_{11}^{(\beta\gamma)} - C_{12}^{(\beta\gamma)}\right)\varepsilon_{33}^{p\,(\beta\gamma)}$$

$$S_{12}^{(\beta\gamma)} = C_{44}^{(\beta\gamma)}\left(\phi_1^{(\beta\gamma)} + \frac{\partial w_2}{\partial x_1}\right) - 2\,C_{44}^{(\beta\gamma)}\,\varepsilon_{12}^{p\,(\beta\gamma)}$$

$$S_{13}^{(\beta\gamma)} = C_{44}^{(\beta\gamma)}\left(\psi_1^{(\beta\gamma)} + \frac{\partial w_3}{\partial x_1}\right) - 2\,C_{44}^{(\beta\gamma)}\,\varepsilon_{13}^{p\,(\beta\gamma)}$$

$$S_{23}^{(\beta\gamma)} = C_{66}^{(\beta\gamma)}\left(\psi_2^{(\beta\gamma)} + \phi_3^{(\beta\gamma)}\right) - 2\,C_{66}^{(\beta\gamma)}\,\varepsilon_{13}^{p\,(\beta\gamma)} \tag{3.64}$$

where $\alpha_i^{(\beta\gamma)}$ are the subcell CTEs. It should be noted that the coefficients of the inelastic terms are specialized to an isotropic material because the inelastic constitutive theory that will be used is applicable only for an isotropic material. If the material is transversely isotropic, it is required to be elastic in both CCMICRON and MCLAM.

As the last step in generating the effective constitutive equations, continuity of tractions is applied along the subcell and cell interfaces in an average sense yielding

$$S_{2i}^{(1\gamma)} = S_{2i}^{(2\gamma)} \tag{3.65}$$

$$S_{3i}^{(\beta 1)} = S_{3i}^{(\beta 2)} \tag{3.66}$$

At this point, there is a sufficient number of equations to solve for the microvariables to obtain the overall composite stress-strain relations. From (3.51) with i = 2,

$$\phi_2^{(12)} = \frac{\left(h\,\bar{\varepsilon}_{22} - h_2\,\phi_2^{(22)}\right)}{h_1} \tag{3.67}$$

$$\phi_2^{(21)} = \frac{\left(h\,\bar{\varepsilon}_{22} - h_1\,\phi_2^{(11)}\right)}{h_2} \tag{3.68}$$

where $h = h_1 + h_2$. Similarly, from (3.53) with i = 3,

$$\psi_3^{(12)} = \frac{\left(l\,\bar{\varepsilon}_{33} - l_1\,\psi_3^{(11)}\right)}{l_2} \tag{3.69}$$

$$\psi_3^{(21)} = \frac{\left(l\,\bar{\varepsilon}_{33} - l_2\,\psi_3^{(22)}\right)}{l_1} \tag{3.70}$$

where $l = l_1 + l_2$. From (3.65) with i = 2, using (3.64) and (3.67)-(3.70), we obtain:

$$\begin{aligned}\left(C_{22}^f + \frac{h_1}{h_2}C_{22}^m\right)\phi_2^{(11)} + C_{23}^f\,\psi_3^{(11)} + C_{23}^m\frac{l_2}{l_1}\,\psi_3^{(22)} &= \left(C_{12}^m - C_{12}^f\right)\bar{\varepsilon}_{11} + C_{22}^m\frac{h}{h_2}\bar{\varepsilon}_{22} + C_{23}^m\frac{l}{l_1}\bar{\varepsilon}_{33} \\ &\quad -\left(F_m^T - F_f^T\right)\Delta T - \left(C_{11}^m - C_{12}^m\right)\varepsilon_{22}^{p\,(21)} + \left(C_{11}^f - C_{12}^f\right)\varepsilon_{22}^{p\,(11)}\end{aligned} \tag{3.71}$$

$$C_{22}^m\left(1 + \frac{h_2}{h_1}\right)\phi_2^{(22)} + C_{23}^m\frac{l_1}{l_2}\,\psi_3^{(11)} + C_{23}^m\,\psi_3^{(22)} = C_{22}^m\frac{h}{h_1}\bar{\varepsilon}_{22} + C_{23}^m\frac{l}{l_2}\bar{\varepsilon}_{33} - \left(C_{11}^m - C_{12}^m\right)\left(\varepsilon_{22}^{p\,(12)} - \varepsilon_{22}^{p\,(22)}\right) \tag{3.72}$$

where $F_i^T = C_{12}^i \alpha_1^i + \left(C_{22}^i + C_{23}^i\right)\alpha_2^i \quad (i = f, m)$. Recognizing that the (11) subcell is occupied by the fiber while the remaining subcells are occupied by matrix, "f" and "m" superscripts have been used in (3.71) and (3.72). From (3.66) with i=3, using (3.64) and (3.67)-(3.70), we obtain:

$$C_{23}^f \phi_2^{(11)} + C_{23}^m \frac{h_2}{h_1}\phi_2^{(22)} + \left(C_{22}^f + C_{22}^m \frac{l_1}{l_2}\right)\psi_3^{(11)} = \left(C_{12}^m - C_{12}^f\right)\bar{\varepsilon}_{11} + C_{23}^m \frac{h}{h_1}\bar{\varepsilon}_{22} + C_{22}^m \frac{l}{l_2}\bar{\varepsilon}_{33} - \left(F_m^T - F_f^T\right)\Delta T - \left(C_{11}^m - C_{12}^m\right)\varepsilon_{33}^{p\,(12)} + \left(C_{11}^f - C_{11}^m\right)\varepsilon_{33}^{p\,(11)} \tag{3.73}$$

$$C_{23}^m \frac{h_1}{h_2}\phi_2^{(11)} + C_{23}^m \phi_2^{(22)} + C_{22}^m\left(1 + \frac{l_2}{l_1}\right)\psi_3^{(22)} = C_{23}^m \frac{h}{h_2}\bar{\varepsilon}_{22+} + C_{22}^m \frac{l}{l_1}\bar{\varepsilon}_{33} - \left(C_{11}^m - C_{12}^m\right)\left(\varepsilon_{33}^{p\,(21)} - \varepsilon_{33}^{p\,(22)}\right) \tag{3.74}$$

Equations (3.71) - (3.74) form a set of simultaneous equations that can be written,

$$\begin{bmatrix} 0 & A_1 & A_2 & A_3 \\ A_4 & 0 & A_5 & A_6 \\ A_7 & A_8 & A_9 & 0 \\ A_{10} & A_{11} & 0 & A_{12} \end{bmatrix} \begin{bmatrix} \phi_2^{(11)} \\ \phi_2^{(22)} \\ \psi_3^{(11)} \\ \psi_3^{(22)} \end{bmatrix} = \begin{bmatrix} J_1 \\ J_2 \\ J_3 \\ J_4 \end{bmatrix}. \tag{3.75}$$

Equation (3.75) can then be inverted to solve for the microvariables,

$$\begin{bmatrix} \phi_2^{(11)} \\ \phi_2^{(22)} \\ \psi_3^{(11)} \\ \psi_3^{(22)} \end{bmatrix} = \begin{bmatrix} T_1 & T_2 & T_3 & T_4 \\ T_5 & T_6 & T_7 & T_8 \\ T_9 & T_{10} & T_{11} & T_{12} \\ T_{13} & T_{14} & T_{15} & T_{16} \end{bmatrix} \begin{bmatrix} J_1 \\ J_2 \\ J_3 \\ J_4 \end{bmatrix}. \tag{3.76}$$

Where explicit expressions for A_i, T_i, and J_i are given in Appendix C.

The remaining microvariables involved in the normal stress-strain relations can be determined using (3.67) - (3.70). Then using (3.60) and (3.64) the composite constitutive relations are obtained in the form,

$$\begin{bmatrix} \overline{\sigma}_{11} \\ \overline{\sigma}_{22} \\ \overline{\sigma}_{33} \end{bmatrix} = \begin{bmatrix} b_{11} & b_{12} & b_{13} \\ b_{12} & b_{22} & b_{23} \\ b_{13} & b_{23} & b_{33} \end{bmatrix} \left\{ \begin{bmatrix} \overline{\varepsilon}_{11} \\ \overline{\varepsilon}_{22} \\ \overline{\varepsilon}_{33} \end{bmatrix} - \begin{bmatrix} \alpha_1^* \\ \alpha_2^* \\ \alpha_3^* \end{bmatrix} \Delta T \right\} - \begin{bmatrix} H_{11} \\ H_{22} \\ H_{33} \end{bmatrix} \tag{3.77}$$

where b_{ij} are components of the effective stiffness matrix, H_{ij} contain the plastic terms, and α_i^* are the effective composite CTEs. The effective CTEs that arise from the method of cells are identical to those predicted by Levin's formula (Aboudi 1991). The expressions for b_{ij}, H_{ij}, and α_i^* are given in Appendix C.

For a square cell and square subcells (i.e., $h_1 = h_2$ and $l_1 = l_2$), $b_{12} = b_{13}$, $b_{22} = b_{33}$, and $b_{44} = b_{55}$. This leaves 6 independent elastic constants, rather than 5 for the transversely isotropic case. It is desirable to have cylinders in CCMICRON and layers in MCLAM that are transversely isotropic (with isotropy in the plane transverse to the fiber direction). Thus the effective stiffness matrix components are rotationally averaged about the x_1 axis to yield a transversely isotropic set of effective stiffness components. The results of this averaging procedure are given in Appendix C.

The effective shear stress-strain relations are not needed for CCMICRON since all shear components of stress and strain are zero for the axisymmetric loading that is considered in the development of the model. For MCLAM, while the out-of-plane shear stress and strain components $(\sigma_{13}, \varepsilon_{13}, \sigma_{23}, \varepsilon_{23})$ in a lamina are zero, the in-plane shear stress and strain components $(\sigma_{12}, \varepsilon_{12})$ are, in general, non-zero. Thus, effective in-plane shear stress-strain relations are needed.

From (3.51) with i=1, we obtain:

$$\phi_1^{(21)} = \frac{h\dfrac{\partial w_1}{\partial x_2} - h_1\phi_1^{(11)}}{h_2} \tag{3.78}$$

$$\phi_1^{(12)} = \frac{h\dfrac{\partial w_1}{\partial x_2} - h_2\phi_1^{(22)}}{h_1}. \tag{3.79}$$

and from (3.65) with i=1, using (3.64), we have:

$$C_{44}^{f}\left(\phi_1^{(11)}+\frac{\partial w_2}{\partial x_1}\right)-2\,C_{44}^{f}\,\varepsilon_{12}^{p\,(11)}=C_{44}^{m}\left(\phi_1^{(21)}+\frac{\partial w_2}{\partial x_1}\right)-2\,C_{44}^{m}\,\varepsilon_{12}^{p\,(21)} \tag{3.80}$$

$$\phi_1^{(12)}-2\,\varepsilon_{12}^{p\,(12)}=\phi_1^{(22)}-2\,\varepsilon_{12}^{p\,(22)}. \tag{3.81}$$

Equations (3.78) and (3.80) can be solved for $\phi_1^{(11)}$ and $\phi_1^{(21)}$ while (3.79) and (3.81) can be solved for $\phi_1^{(12)}$ and $\phi_1^{(22)}$.

$$\phi_1^{(11)}=\frac{hC_{44}^{m}\dfrac{\partial w_1}{\partial x_2}+h_2\left(C_{44}^{m}-C_{44}^{f}\right)\dfrac{\partial w_2}{\partial x_1}-2h_2\left(C_{44}^{m}\varepsilon_{12}^{p\,(21)}-C_{44}^{f}\varepsilon_{12}^{p\,(11)}\right)}{h_2C_{44}^{f}+h_1C_{44}^{m}} \tag{3.82}$$

$$\phi_1^{(21)}=\frac{hC_{44}^{f}\dfrac{\partial w_1}{\partial x_2}-h_1\left(C_{44}^{m}-C_{44}^{f}\right)\dfrac{\partial w_2}{\partial x_1}+2h_1\left(C_{44}^{m}\varepsilon_{12}^{p\,(21)}-C_{44}^{f}\varepsilon_{12}^{p\,(11)}\right)}{h_2C_{44}^{f}+h_1C_{44}^{m}} \tag{3.83}$$

$$\phi_1^{(12)}=\frac{\partial w_1}{\partial x_2}+2\frac{h_2}{h}\left(\varepsilon_{12}^{p\,(12)}-\varepsilon_{12}^{p\,(22)}\right) \tag{3.84}$$

$$\phi_1^{(22)}=\frac{\partial w_1}{\partial x_2}-2\frac{h_1}{h}\left(\varepsilon_{12}^{p\,(12)}-\varepsilon_{12}^{p\,(22)}\right) \tag{3.85}$$

The remaining constitutive relation can then be determined as follows.

$$\bar{\sigma}_{12}=\frac{1}{V}\sum_{\beta,\gamma=1}^{2}V_{\beta\gamma}\,S_{12}^{(\beta\gamma)}=2b_{44}\bar{\varepsilon}_{12}-H_{12} \tag{3.86}$$

where $\bar{\varepsilon}_{12}=\dfrac{1}{2}\left(\dfrac{\partial w_1}{\partial w_2}+\dfrac{\partial w_2}{\partial w_1}\right)$. The expressions for b_{44} and H_{12} are given in Appendix C. At this point, everything that is needed from the method of cells for CCMICRON and MCLAM has been determined.

3.4 Incorporation of the Method of Cells into CCMICRON and MCLAM

The process of incorporating the method of cells into CCMICRON and MCLAM is straightforward. CCMICRON relies on the effective properties for each cylinder and MCLAM relies on effective properties for each layer. These effective properties, in the form of effective stiffness components and effective CTEs, are determined from the method of cells using equations (3.77) and (3.86) given in the preceding section. For elastic cases, this is all that is necessary. However, for cases in which plasticity is present, the microgeometry of the method of cells is utilized again.

In CCMICRON, the stress and strain components are dependent on the radial distance, r. In MCLAM, the stress and strain components are dependent on the through-thickness position, z. In both models the plastic strains are integrated over the model geometry to find the plastic force terms in equations (3.15) and (3.33). To accurately account for this variation in the plastic strain integrals, the individual cylinders in CCMICRON and the individual layers in MCLAM are divided into 20 regions. This results in 21 evaluation points in each cylinder or layer, where the first and last point coincide with the individual cylinder or layer boundaries. The stress and strain components at these 21 points are continuously updated throughout the specified loading cycle. When plasticity is present, the strain components are evaluated from the solution of equation (3.15) or (3.33) at a particular evaluation point and subsequently applied as the average cell strains within the method of cells. It should be noted that for MCLAM, the average cell strains correspond to the strains at the evaluation point in the principle material (1-2) coordinate system for the layer. The subcell strains are then determined from (3.36). The results are,

$$\varepsilon_{11}^{(\beta\gamma)} = \bar{\varepsilon}_{11} \qquad \varepsilon_{22}^{(\beta\gamma)} = \phi_2^{(\beta\gamma)} \qquad \varepsilon_{33}^{(\beta\gamma)} = \psi_{33}^{(\beta\gamma)}$$

$$\varepsilon_{12}^{(11)} = \frac{C_{44}^m (h_1 + h_2)}{h_1 C_{44}^m + h_2 C_{44}^f} \bar{\varepsilon}_{12}$$

$$\varepsilon_{12}^{(21)} = \frac{C_{44}^f (h_1 + h_2)}{h_1 C_{44}^m + h_2 C_{44}^f} \bar{\varepsilon}_{12}$$

$$\varepsilon_{12}^{(12)} = \varepsilon_{12}^{(22)} = \bar{\varepsilon}_{12} \tag{3.87}$$

where the microvariables are obtained from the solution of equation (3.76).

Thus, the subcell strains are known at each evaluation point. The knowledge of the average and subcell strains allows the determination of plastic strain increments within each subcell using the classical incremental plasticity theory equations presented in Section 3.6. These subcell plastic strain increments are then used to evaluate increments in the plasticity terms (the H_{ij} terms) in (3.77) and (3.86). The H_{ij} increments are then used to determine the macroscopic plastic strain increments from,

$$\begin{bmatrix} d\varepsilon_1^p \\ d\varepsilon_2^p \\ d\varepsilon_3^p \end{bmatrix} = \begin{bmatrix} b_{11} & b_{12} & b_{13} \\ b_{12} & b_{22} & b_{23} \\ b_{13} & b_{23} & b_{33} \end{bmatrix}^{-1} \begin{bmatrix} dH_{11} \\ dH_{22} \\ dH_{33} \end{bmatrix}$$

$$d\varepsilon_{12}^p = \frac{dH_{12}}{b_{44}}. \tag{3.88}$$

These plastic strain increments are then used to re-evaluate the plastic force terms, resulting in new macroscopic strains at each evaluation point upon solution of the respective global equations, (3.15) and (3.33). The new estimates of the total macroscopic strains at the various radial or through-thickness locations are then passed to the method of cells, and the process is repeated, as described in the following section, until the desired convergence is achieved.

To summarize the process, when plasticity is present, the strain components at the evaluation points obtained from CCMICRON and MCLAM are taken as the average cell strain components in the method of cells. The subcell strains are then calculated and used to evaluate the subcell plastic strain increments using the classical incremental plasticity theory equations. These are then employed to calculate the macroscopic plastic strain increments.

3.5 Solution Procedure

In CCMICRON and MCLAM, the sets of equations that must be solved are given by (3.15) and (3.33) respectively. They can both be written in the form,

$$\underline{\underline{SM}}\ \underline{\xi} = \underline{F}^m + \underline{F}^T + \underline{F}^p \tag{3.89}$$

where $\underline{\underline{SM}}$ is a type of stiffness matrix, $\underline{\xi}$ is a vector consisting of the unknown displacements in the case of CCMICRON, or midplane strains and curvatures in the case of MCLAM, $\underline{F}^m$ is the mechanical force vector, $\underline{F}^T$ is the thermal force vector, and $\underline{F}^p$ is the plastic force vector. In the derivation presented in Section 3.1, it is assumed that there is no mechanical loading for CCMICRON. In both models, when plasticity is present, equation (3.89) cannot be solved for $\underline{\xi}$ directly because the components of $\underline{F}^p$ depend on total strain components, which themselves depend on the components of $\underline{\xi}$. Since $\underline{\xi}$ is not known, the total strain components cannot be evaluated directly, and neither can the components of $\underline{F}^p$. Thus an iterative process is necessary, together with application of mechanical and thermal loading in an incremental manner.

Once yielding has occurred, the plastic strains are set to what they were after the completion of the previous loading increment. The loading is incremented (i.e., a small temperature or mechanical loading step is applied) and the appropriate equations are used to calculate the components of the plastic force vector based on the previous plastic strain values. The thermal and mechanical force terms are known exactly, so (3.89) can be solved for the unknown vector, $\underline{\xi}$. The components of this vector are the interfacial radial displacements and the uniform axial strain in CCMICRON, and the midplane strains and curvatures in the lamination theory. These terms are then used to evaluate the strain field in the cylindrical assemblage or laminate. These new strain values are then used to calculate plastic strain increments through the use of the method of cells and the classical incremental plasticity constitutive theory. If the plastic strain increments are non-zero, the assumption that the plastic strains were the same

as they were after the previous loading increment was incorrect. The strain increments are added to these previous plastic strains following the procedure outlined by Mendelson (1983),

$$\varepsilon_{ij}^{p} = \varepsilon_{ij}^{p}\Big|_{previous} + d\varepsilon_{ij}^{p} \tag{3.90}$$

where $d\varepsilon_{ij}^{p}$ are the plastic strain increments. Section 3.6 will discuss how the plastic strain increments are calculated using the classical incremental plasticity theory.

Using the new values for the plastic strain components, the components of the plastic force vector are re-evaluated. Clearly, from (3.89), when the plastic force vector components change, the components of the unknown vector will change as well. The total strain field is modified, thus the plastic strains change again, and the process must be repeated. Eventually, after a number of iterations, the plastic strains converge, and another loading increment can be applied.

As noted in the previous section, since the strain components depend on the radial coordinate r in CCMICRON and the through-thickness coordinate z in MCLAM, they must be evaluated at a number of points in each cylinder or layer. The integrals that appear in the plastic force vector (see Appendix A and equations (3.31) and (3.32)) are evaluated numerically based on the plastic strains at a number of points in each layer or cylinder. Twenty-one evaluation points are used for this purpose.

3.6 Classical Incremental Plasticity Theory

The inelastic constitutive theory used in CCMICRON and MCLAM is based on modified Prandtl-Reuss incremental classical plasticity equations proposed by Mendelson (1983). Omitting the designation $(\beta\gamma)$ that identifies a given subcell for notational simplicity, the plastic strain increments for each subcell are calculated from

$$d\varepsilon_{ij}^{p} = e'_{ij}\, d\lambda \tag{3.91}$$

where e'_{ij} is the modified strain deviator and $d\lambda$ is a proportionality constant that ensures that the stress vector remains on the yield surface during plastic loading (Williams and Pindera, 1994b). The modified strain deviator is defined as

$$e'_{ij} = \varepsilon_{ij} - \varepsilon_{ij}^{p} - \frac{1}{3}\delta_{ij}\varepsilon_{kk} \tag{3.92}$$

where ε_{ij} is the total strain tensor for the subcell, and δ_{ij} is the Kronecker delta. It should be noted that the shear strains in this section are tensorial quantities. The proportionality constant, $d\lambda$, is given by

$$d\lambda = 1 - \frac{\sigma_{eff}}{3G\,\varepsilon_{et}} \tag{3.93}$$

where G is the subcell shear modulus, σ_{eff} is the effective stress in the matrix subcells, and ε_{et} is the equivalent modified total strain. $d\lambda > 0$ for plastic loading, and $d\lambda \le 0$ for neutral loading or unloading. In the modified Prandtl-Reuss equations proposed by Mendelson, the von Mises yield condition is built into (3.93); if $d\lambda \le 0$, no further yielding takes place. The equivalent modified strain required in (3.93) is given by,

$$\varepsilon_{et} = \sqrt{\frac{2}{3} e'_{ij} e'_{ij}}\,. \tag{3.94}$$

where the modified strain deviator, e'_{ij}, is known from (3.92).

The stress-strain response of the fiber is taken to be linearly elastic and temperature-dependent, and the elastoplastic matrix is taken to be bilinear and temperature-dependent. Input data for the models are required in the form of the yield stress (Y) and the post-yield slope of the stress-strain curve ("hardening slope", H) at a user-determined number of temperatures. The effective stress in the matrix is given by,

$$\sigma_{eff} = H\varepsilon^{p}_{eff} + Y \tag{3.95}$$

where ε^{p}_{eff} is the effective plastic strain, calculated from

$$\varepsilon^{p}_{eff} = \varepsilon^{p}_{eff}\Big|_{previous} + d\varepsilon^{p}_{eff} \tag{3.96}$$

where the effective plastic strain increment is given by

$$d\varepsilon_{eff} = \frac{\sqrt{2}}{3}\sqrt{\left(d\varepsilon^{p}_{1} - d\varepsilon^{p}_{2}\right)^{2} + \left(d\varepsilon^{p}_{2} - d\varepsilon^{p}_{3}\right)^{2} + \left(d\varepsilon^{p}_{3} - d\varepsilon^{p}_{1}\right)^{2} + 6\left(d\varepsilon^{p}_{12}\right)}\,. \tag{3.97}$$

4. Analytical Predictions

This chapter addresses the effects of matrix plasticity, stress-free temperature, nonuniform fiber distribution, and misalignment of fibers on the thermal expansion of Gr/Cu composites. The objective is to determine under what conditions these effects are important and should be considered in modeling the thermal response of real Gr/Cu composites. The examination of the effect of nonuniform fiber distribution comprises the majority of the chapter. Radially nonuniform fiber distribution and fiber distribution that is nonuniform in the through-thickness direction are modeled using CCMICRON and MCLAM, respectively.

4.1 Material Properties

In order to model the effective thermal expansion of Gr/Cu, material properties for graphite fibers and copper are needed as input data to the models described in the previous chapter. The required properties are the Young's moduli, the Poisson's ratios, the axial shear moduli (for transversely isotropic materials), the CTEs, and two quantities that characterize the inelastic behavior, namely the yield stress and the hardening slope. The constitutive response of inelastic materials is taken to be bilinear; the slope of the post-yield response is called the hardening slope (HSP). Table 4.1 gives the material properties for P100 graphite fibers and OFHC copper at a number of temperatures, together with the source of the data.

The ability of the models to accurately predict the composite behavior depends on the reliability of the material properties of the individual constituents. Unfortunately, the properties of the P100 graphite are not well characterized. The mechanical properties of the graphite fibers from Volk *et. al.* (1991) were backed out of a concentric cylinder model, while the fiber axial CTEs were obtained from measurements using a fiber dilatometer. The transverse fiber CTEs, on the other hand, were backed out using Chamberlain's equation with experimental transverse thermal expansion data for Gr/Cu (Ellis, 1992). These values may contain some error since Chamberlain's equation assumes that the composite behaves elastically (Raghava, 1988).

P100 Graphite Fibers

Temp °F	E_A Msi	E_T Msi	G_A Msi	ν_A	ν_T	α_A 10^{-6}/°F	α_T 10^{-6}/°F
70	100	0.5	1.42	0.41	0.45	-5.03	0
100	100	0.5	1.42	0.41	0.45	-4.75	1.2
300	100	0.5	1.42	0.41	0.45	-2.27	9.2
500	100	0.5	1.42	0.41	0.45	-0.208	14
700	101	0.5	1.42	0.41	0.45	0.992	14.4
900	102	0.5	1.42	0.41	0.45	2.53	14.8
1100	103.5	0.5	1.42	0.41	0.45	4.97	15.6
1300	104.5	0.5	1.42	0.41	0.45	5.45	16.3
1500	105.5	0.5	1.42	0.41	0.45	5.45	17.1
1700	106.5	0.5	1.42	0.41	0.45	5.45	17.9
Source	1	1	1	1	1	2	2

OFHC Copper

Temp °F	E Msi	ν	α 10^{-6}/°F	σ_Y Ksi	HSP Msi
70	18.8	0.35	8.18	10.3	1.425
100	18.7	0.35	8.28	9.97	1.403
300	18.0	0.35	9.35	9.37	1.270
500	17.2	0.36	10.1	8.95	1.126
700	16.4	0.37	10.7	8.42	1.000
900	15.5	0.375	11.6	6.15	0.760
1100	14.5	0.38	12.0	3.87	0.521
1300	13.2	0.38	12.3	2.25	0.363
1500	11.7	0.37	12.6	1.25	0.282
1700	9.8	0.35	14.7	0.27	0.204
Source	3	3	3	3/4	3/4

Table 4.1: Material properties for P100 graphite fibers and OFHC copper. Sources: 1 - Volk *et. al.* (1991); 2 - Ellis (1992); 3 - Rocketdyne Materials Properties Manual (1987); 4 - NASA Lewis Research Center (1992).

4.2 Effect of Plasticity

It is generally accepted that matrix yielding can occur in metal matrix composites when they are subjected to sufficiently high temperature changes. This is due to the large mismatch in the CTE of ceramic fibers and metallic matrices. When a temperature change is applied to a composite, the fiber and matrix tend to expand or contract by different amounts, especially in the direction of the fibers. However, since the fiber and matrix are bonded together, they must expand or contract the same amount in the fiber direction. This gives rise to stresses that are often high enough to yield the matrix.

If the effect of plasticity is ignored, the stresses in the matrix will continue to increase with increasing thermal load to a level that may be unrealistic for the material, resulting in a predicted composite response that will also be unrealistic. Figures 4.1 and 4.2 present a comparison of predictions for the longitudinal and transverse thermal expansion of Gr/Cu with an elastic matrix and an elastoplastic

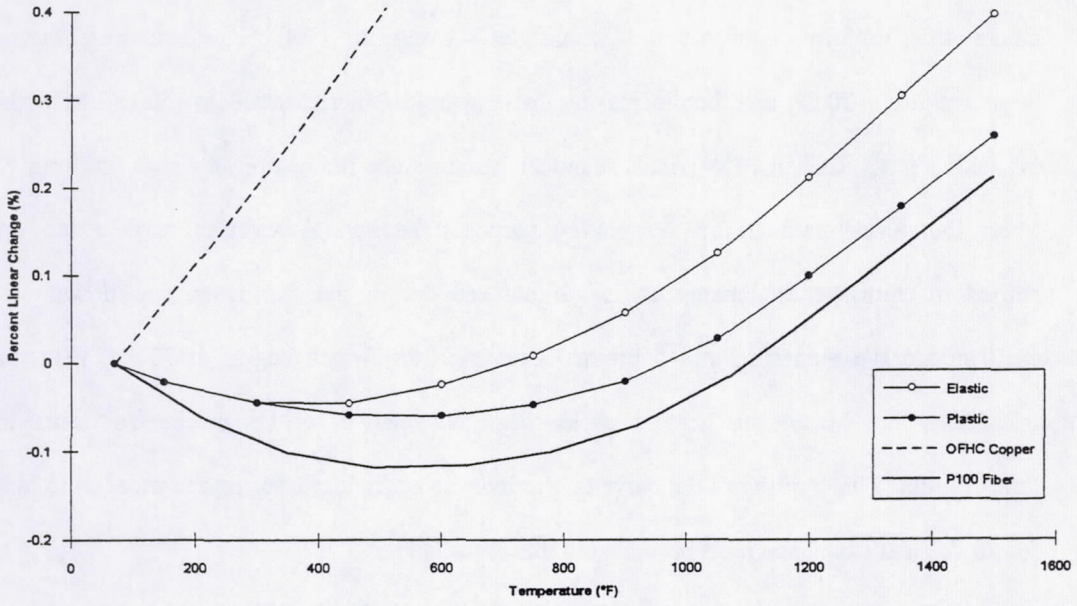

Figure 4.1: Longitudinal thermal expansion of 50 v/o Gr/Cu. Comparison between elastic and elastoplastic analysis. MCLAM was used with uniform fiber distribution to generate the composite results shown.

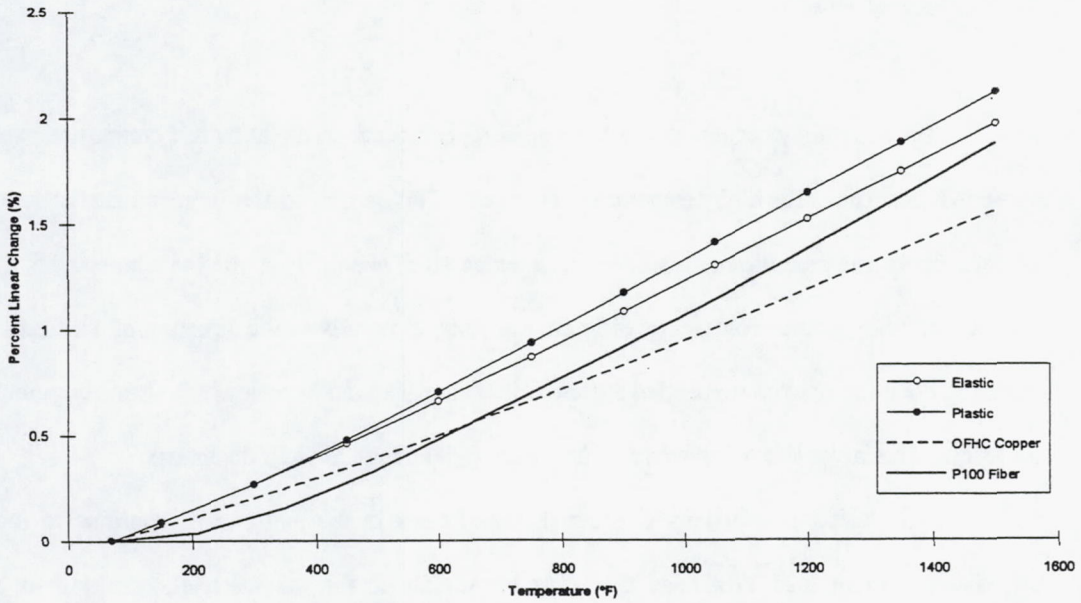

Figure 4.2: Transverse thermal expansion of 50 v/o Gr/Cu. Comparison between elastic and elastoplastic analysis. MCLAM was used with uniform fiber distribution to generate the composite results shown.

matrix. A stress-free temperature of 1700 °F was employed in the calculations. MCLAM was used to model this uniform unidirectional composite starting at 1700 °F, decreasing the temperature incrementally to 70 °F, and then increasing the temperature incrementally to 1500 °F to model a thermal expansion test. CCMICRON yields identical results since for composites with uniformly distributed fibers, the models are the same. For plotting purposes, the thermal expansion curve of the composite was shifted to eliminate the change in length induced during the fabrication cool-down. The thermal expansion curve then simulates a thermal expansion test which begins at 70 °F, with the thermally induced strain during the heating cycle measured relative to the specimen's dimensions at this temperature. This shifting of the curve to eliminate strain induced during the processing history is done for all thermal expansion plots presented in this investigation.

Thermal expansion curves are presented rather than plots of the instantaneous effective CTE of the composite because plastic deformation is an irreversible process. A CTE can only be defined when the thermal expansion is reversible since a CTE represents a material property independent of previous

deformation history. This is the case when a single phase material is subjected to thermal loading, or when the effects of prior inelastic deformation in multi-phase materials shake down due to sufficient strain hardening in the inelastic phases.

Figure 4.1 shows that plasticity has a major effect on the longitudinal response of Gr/Cu. For temperatures up to 300 °F the elastic and plastic predictions are the same since the matrix has not yet yielded. After yielding occurs, the plastic response diverges substantially from the elastic response. In the plastic case, the stresses in the matrix do not build up to the high levels observed in the elastic case. The matrix deforms much more easily in the plastic range, so its ability to restrain or transfer stress to the fiber is diminished. Thus the response is more dominated by the fiber in the plastic case than in the elastic case.

Figure 4.2 shows that the effect of plasticity on the thermal expansion is not as great in the transverse direction, but it is still substantial. Again, the elastic and plastic responses are identical until matrix yielding initiates at approximately 300 °F. The result that the predicted transverse composite response is not bounded by the transverse response of the fiber and the matrix indicates that the Poisson's effect has a significant impact. Since the copper matrix tends to expand more than the fiber in the longitudinal direction during heating, the fiber restrains the copper, placing the copper in compression. Thus, in addition to the positive thermal expansion in the transverse direction, there is a positive mechanical strain in the matrix in the transverse direction induced by the compressive stress in the longitudinal direction.

Matrix plasticity is a major factor affecting the thermal response of Gr/Cu. As the figures indicate, matrix yielding can occur at temperatures as low as 300 °F. The melting temperature of copper is 1981°F, so yielding is occurring well within the useful temperature range for pure copper. Thus treating the material as elastic and employing a yield-limited design strategy would reduce the service temperature of Gr/Cu components to a level that would render them ineffectual for most high heat flux applications. Alternatively, treating Gr/Cu as elastic at higher temperatures results in unrealistic predictions. Therefore, to obtain a useful and realistic model of the response of this composite, matrix inelasticity must be included at the expense of a simple analytical solution.

4.3 Effect of Stress-Free Temperature

When a thermal expansion test is performed on a composite, the expansion is usually measured as a change in length from room temperature. However, as briefly discussed in the preceding section, room temperature is not the true starting point of the thermal history of the composite. During the manufacturing process the composite is subjected to an elevated temperature required for consolidation of the fiber and matrix phases. In the case of Gr/Cu and most other metal matrix composites, the life of the composite begins near the melting temperature of matrix. The composite is then cooled to room temperature, which itself amounts to thermal loading. At some point during cool down, the molten or softened metal forms a bond with the fibers, and residual stresses arise because of the CTE mismatch just as they do during a thermal expansion test. Thus at the start of a thermal expansion test, high residual stresses may already exist in the composite, and the matrix may have already yielded. The residual stresses can have a profound effect on the behavior of the composite, and it is thus necessary to take these stresses into account when modeling the thermal expansion of metal matrix composites.

To account for residual stresses, a stress-free temperature other than room temperature is chosen. This is a temperature at which it is assumed that no stresses initially exist in the composite. The temperature cycle is started at the stress-free temperature and incrementally decreased to the starting temperature of the simulated thermal expansion test. The actual thermal expansion is then modeled by incrementally increasing the temperature, and the resulting thermal expansion curve is shifted, as described in the previous section, so that the starting temperature of the simulated thermal expansion test corresponds to zero thermal expansion.

The choice of the stress-free temperature can have a profound effect on the thermal expansion behavior. Figures 4.3 - 4.8 show the thermal expansion curves for stress-free temperatures of 1500 °F, 1000 °F, and 70 °F when the fiber volume fraction ranges from 0.70 to 0.30. Several trends should be noted from these figures. Higher stress-free temperatures result in greater thermal expansion in both the longitudinal and transverse directions. For the longitudinal direction, this may be attributable to greater strain-hardening of the matrix during cool down from higher stress-free temperatures. This increases the

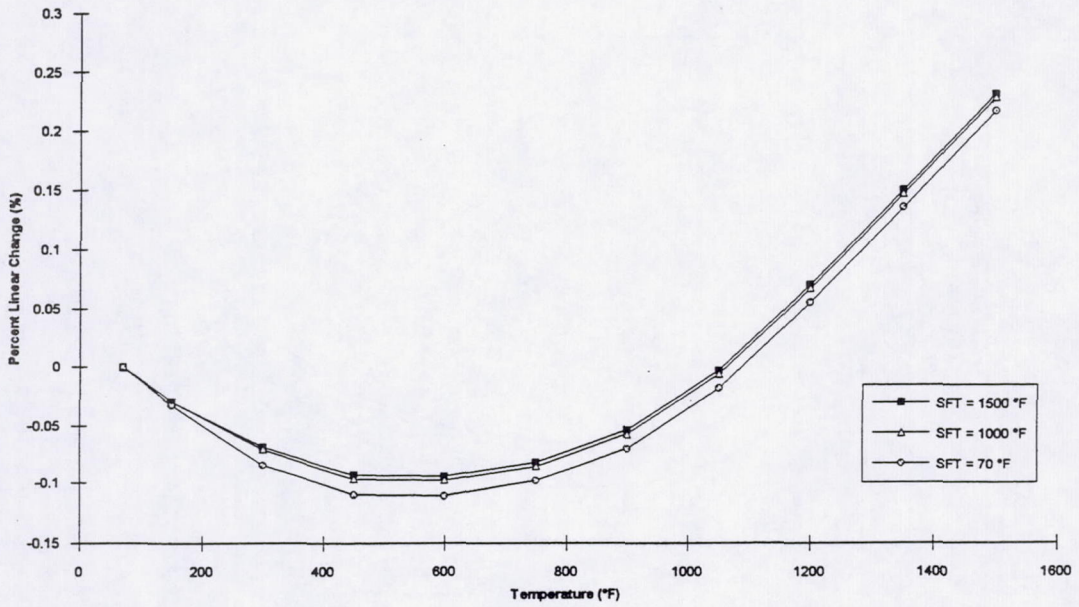

Figure 4.3: Longitudinal thermal expansion of 70 v/o P100 Gr/Cu for three stress-free temperatures (SFTs).

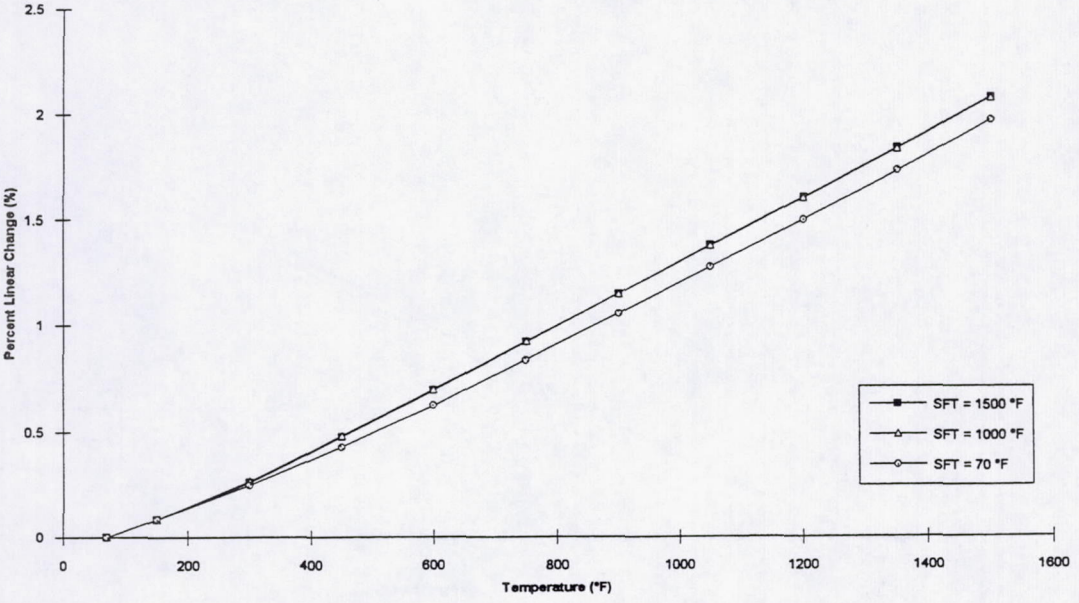

Figure 4.4: Transverse thermal expansion of 70 v/o P100 Gr/Cu for three stress-free temperatures (SFTs).

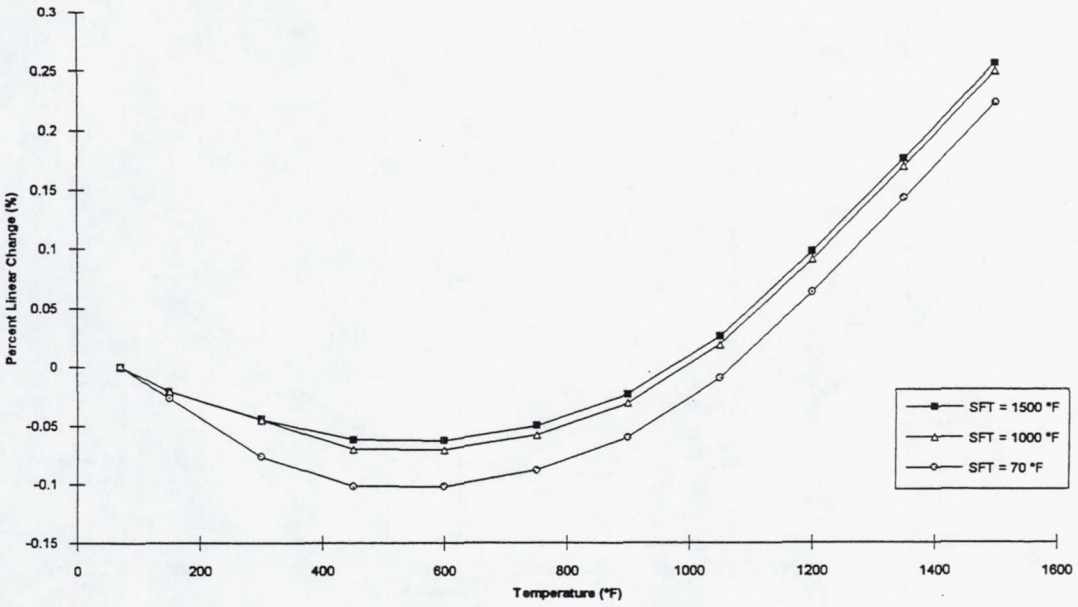

Figure 4.5: Longitudinal thermal expansion of 50 v/o P100 Gr/Cu for three stress-free temperatures (SFTs).

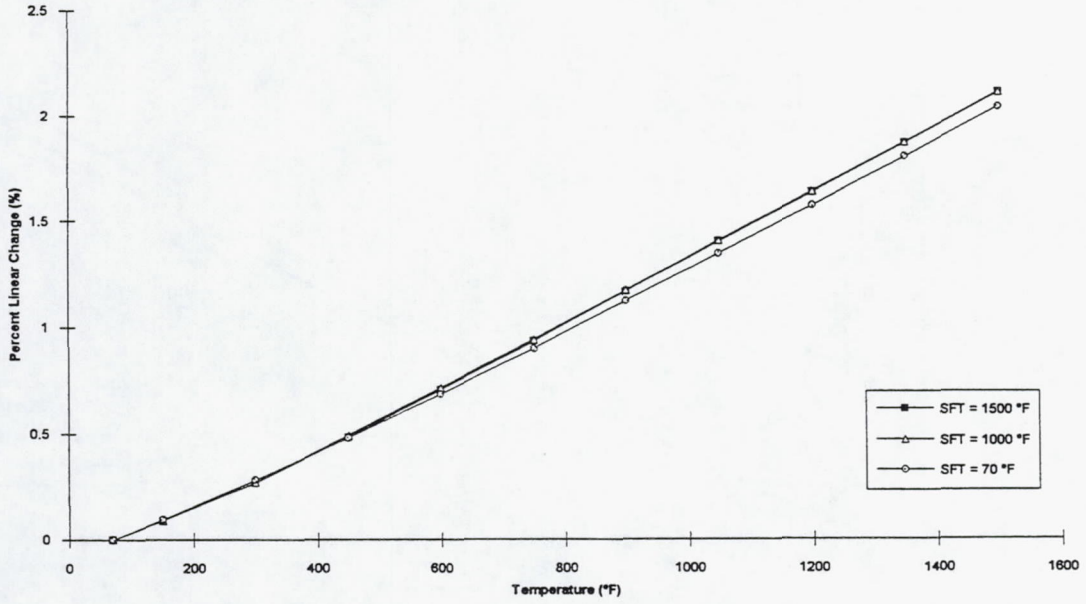

Figure 4.6: Transverse thermal expansion of 50 v/o P100 Gr/Cu for three stress-free temperatures (SFTs).

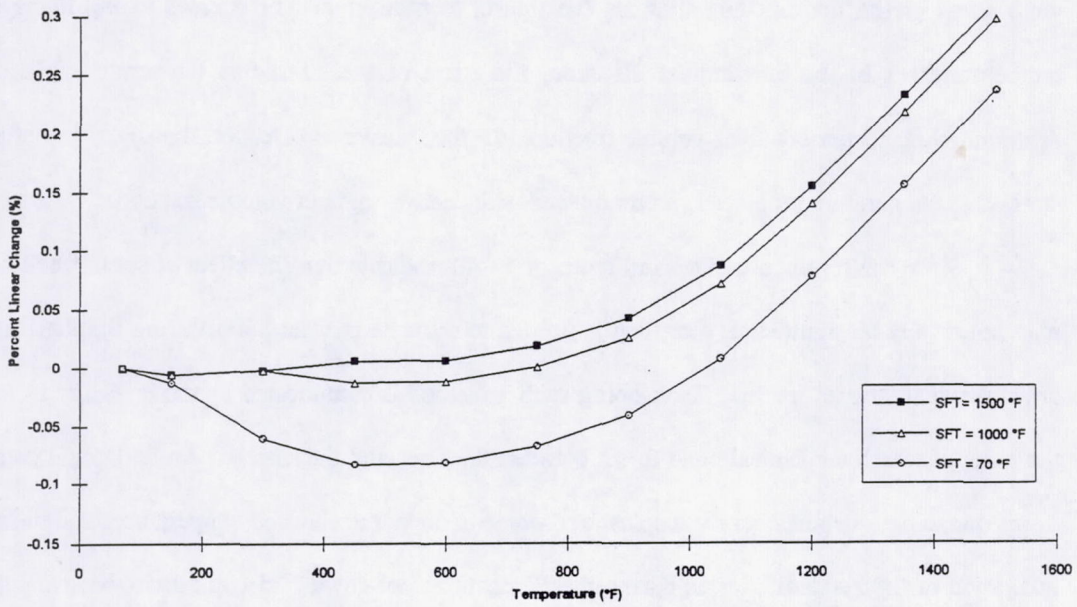

Figure 4.7: Longitudinal thermal expansion of 30 v/o P100 Gr/Cu for three stress-free temperatures (SFTs).

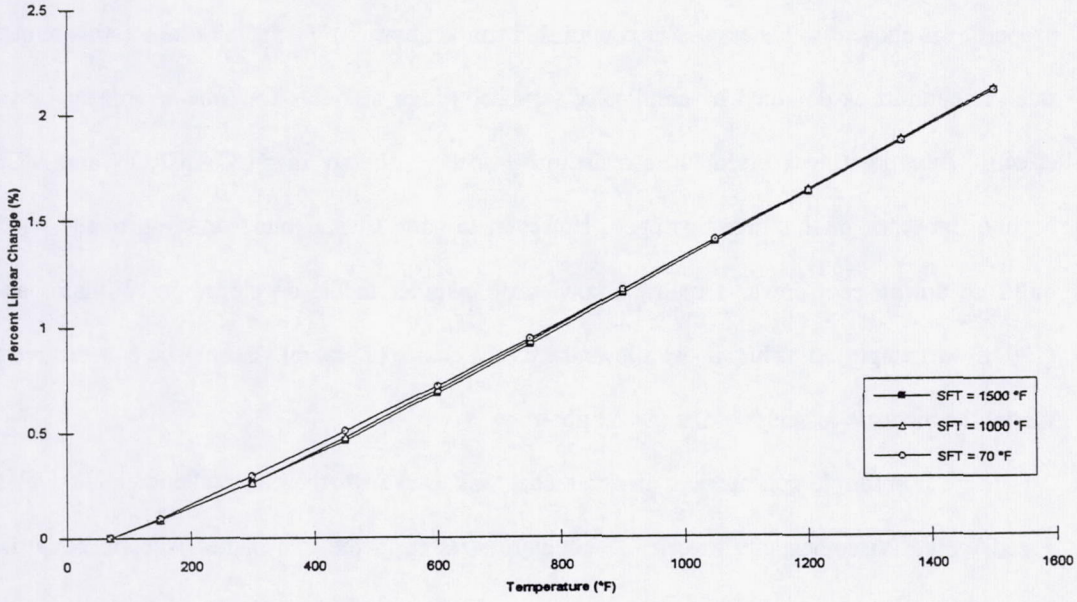

Figure 4.8: Transverse thermal expansion of 30 v/o P100 Gr/Cu for three stress-free temperatures (SFTs).

yield stress of the matrix, thus allowing the matrix to transfer greater stresses to the fibers at higher temperatures. In the longitudinal direction, the effect of the stress-free temperature becomes more profound with decreasing fiber volume fraction. In the transverse direction, however, the effect of the stress-free temperature becomes less pronounced with decreasing fiber volume fraction.

Since the results presented in Figures 4.3 - 4.8 indicate that the effect of stress-free temperature may potentially be significant, a method is needed to estimate at what point during the fabrication cool-down residual stresses initiate. Developing such a method is complicated by the difficulty in identifying the point at which a chemical bond forms between the fiber and the matrix. An additional complication arises due to time-dependent or viscoplastic response of copper at elevated temperatures and the associated relaxation of the residual stresses during the fabrication cool-down. Viscoplasticity becomes significant for metals at temperatures starting from between 0.3 and 0.4 times the absolute melting temperature (Ashby and Jones, 1981). This places the range for copper between 273 °F and 517 °F. Thus, for Gr/Cu, stress relaxation in the matrix may be an important factor.

A potential solution is to estimate bounds for the stress-free temperature. A conservative estimate of the stress-free temperature is obtained by assuming that the composite is stress-free when the matrix is near its molten state. A stress-free temperature that is as high as possible with the known matrix properties is chosen in this case. For copper this temperature is 1700 °F. A lower estimate of the stress-free temperature is obtained by employing a model which accounts for time-dependent or viscoplastic effects. Incorporating a viscoplastic constitutive scheme directly into CCMICRON and MCLAM was beyond the scope of this investigation. However, to gain a better understanding of the residual stress build up during cool down, a multiple concentric cylinder model developed by Williams and Pindera (1994a) was employed. This model allows the user a choice of several viscoplastic constitutive theories to model the inelastic response of the matrix phase.

The multiple concentric cylinder model was used with the classical incremental plasticity and Freed-Walker viscoplasticity theories to compare stresses in the matrix near the fiber-matrix interface after fabrication cool-down. The viscoplasticity theory developed by Freed *et al.* (1993) for application to copper and its alloys has been shown to be generally accurate. Figures 4.9 - 4.11 show the matrix

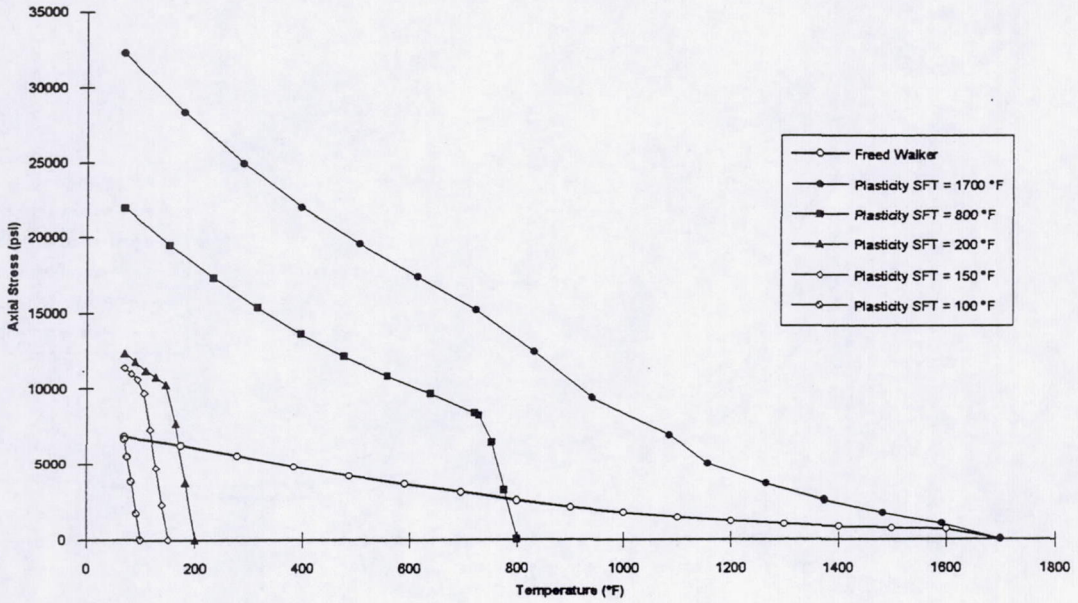

Figure 4.9: Matrix interfacial axial stress in 55 v/o Gr/Cu using multiple concentric cylinder model by Williams and Pindera (1994a) with Freed-Walker viscoplasticity and classical incremental plasticity.

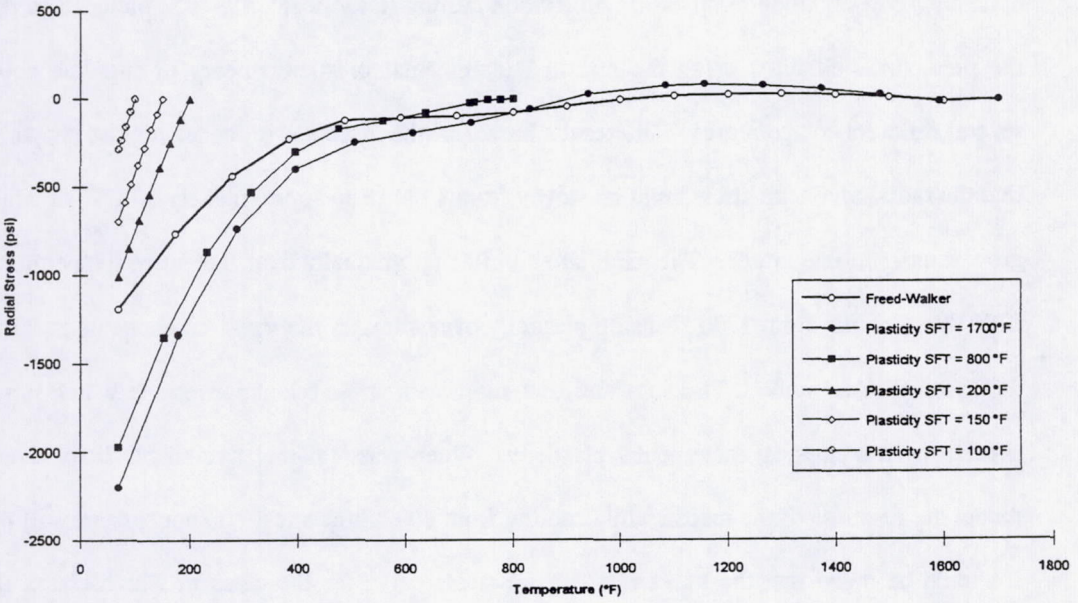

Figure 4.10: Matrix interfacial radial stress in 55 v/o Gr/Cu using multiple concentric cylinder model by Williams and Pindera (1994a) with Freed-Walker viscoplasticity and classical incremental plasticity.

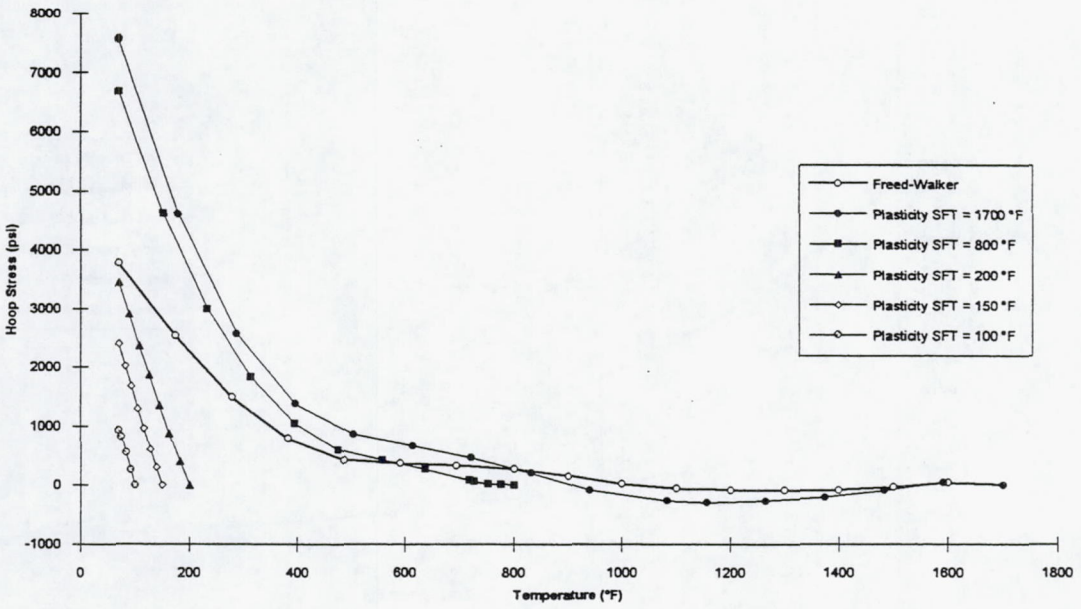

Figure 4.11: Matrix interfacial hoop stress in 55 v/o Gr/Cu using multiple concentric cylinder model by Williams and Pindera (1994a) with Freed-Walker viscoplasticity and classical incremental plasticity.

interfacial stress components predicted using the Freed-Walker viscoplasticity theory after cool-down from 1700 °F to room temperature in 15 minutes, simulating the actual cooling time of a unidirectional Gr/Cu plate after consolidation via pressure infiltration casting (DeVincent, 1994b). Included in the figures are the predictions obtained using the classical incremental plasticity theory to simulate cool-down from several different temperatures. The results based on the viscoplastic model for the copper matrix show that the radial and hoop stress build up slowly from 1700 °F to approximately 500 °F, at which point they grow rapidly in magnitude. The axial stress builds up gradually over the entire temperature range from 1700 °F. Cooling from 1700 °F using plasticity overestimates the stress components at 70 °F relative to the Freed-Walker model. This indicates that significant stress relaxation occurs which is not taken into account by the classical incremental plasticity. When classical incremental plasticity theory is used to model the response of the matrix while cooling from 800 °F the stress components are still overestimated. It should be noted that the knees in the axial stress curve for the cases in which classical incremental

plasticity was used with stress-free temperatures of 800 °F, 200 °F, and 150 °F correspond to the onset of yielding in the matrix.

In order to achieve approximately the same axial residual stress as the Freed-Walker model with plasticity, the stress-free temperature is taken to be 100 °F. Cooling from 100 °F to 70 °F does not cause yielding in the matrix. Since the axial stress is the most significant of the three stress components, 100 °F will be used as one approximation for the stress-free temperature. Using the reasoning described above, and in order to provide an upper bound, 1700 °F will be taken as a second approximation of the stress-free temperature. Subsequent effects that will be examined will be presented for both stress-free temperatures.

4.4 Effect of Nonuniform Fiber Distribution

4.4.1 CCMICRON

CCMICRON allows one to vary the fiber volume fraction in the radial direction in a piecewise fashion. This is accomplished by assembling concentric cylinders with different fiber volume fractions. Since an arbitrary number of concentric cylinders can be used, the radial fiber volume fraction variation can be as continuous as desired. To examine the effects of this type of nonuniform fiber distribution on the thermal expansion of Gr/Cu, it is necessary to compare the thermal expansion of a uniform composite with a nonuniform composite using an identical fiber volume fraction. In order to see the maximum effect, a composite with a large and abrupt change in fiber volume fraction was considered. Thus a composite with a fiber volume fraction of 0.55 was modeled with three different microstructures: uniform, a low fiber volume fraction core surrounded by a high fiber volume fraction cylinder (designated Low-High), and a high fiber volume fraction core surrounded by a low fiber volume fraction cylinder (designated High-Low). The boundary between the high and low fiber volume fraction regions was set at 0.7071 times the assemblage radius, so that the volume of the composite was divided evenly between the two regions. The fiber volume fraction of the dense region was chosen to be 0.9069 to correspond with the densest possible packing of cylinders. In order to achieve an overall fiber volume fraction of 0.55, the fiber volume fraction of the dilute region was set to 0.1931. Figure 4.12 shows the cross-sections of these two configurations.

Longitudinal and transverse thermal expansion curves for the three configurations using stress-free temperatures of 100 °F and 1700 °F are given in Figures 4.13 and 4.14. In the longitudinal direction, the effect of the nonuniform fiber distribution is nearly negligible for both stress-free temperatures. In the transverse direction there is a slight but noticeable variation for a stress-free temperature of 1700 °F. The Low-High configuration shows more divergence from the uniform case than does the High-Low configuration. However, the transverse thermal expansion with a stress-free temperature of 100 °F is not significantly affected by the nonuniform fiber distribution. In all cases shown in Figures 4.13 and 4.14 it is clear that the effect of the chosen stress-free temperatures is far greater than that of the nonuniform

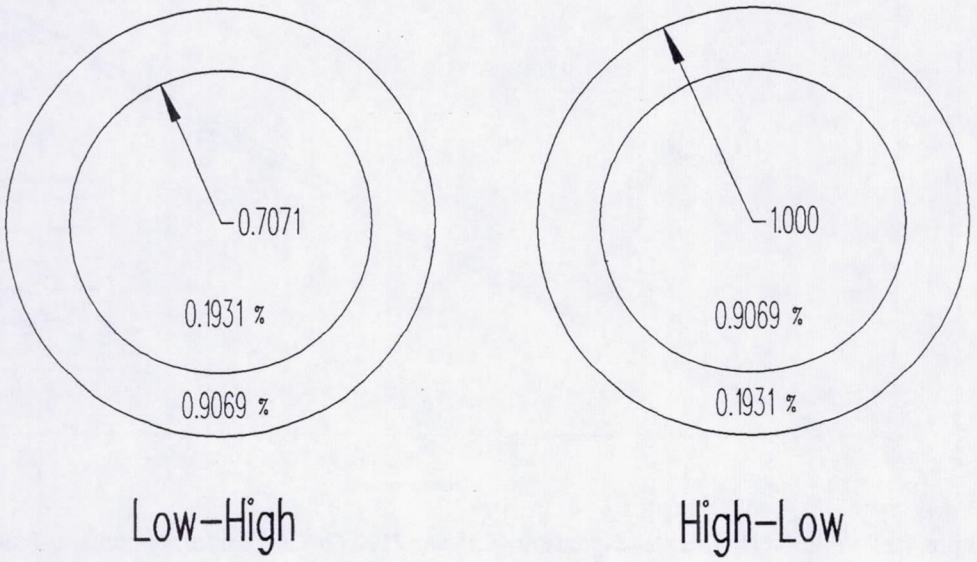

Figure 4.12: CCMICRON composite cylinder microstructures.

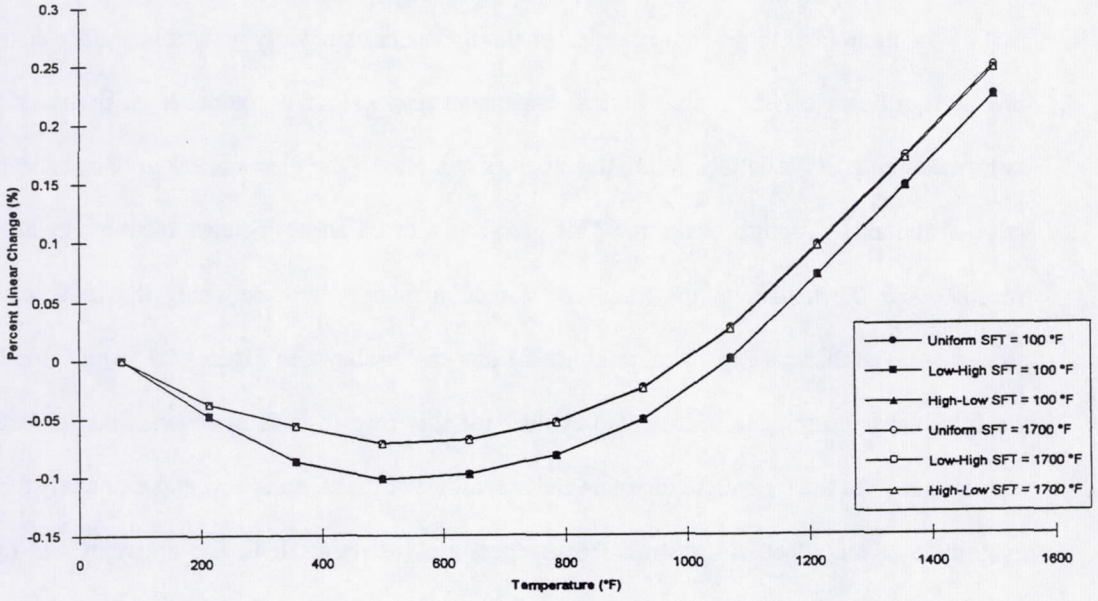

Figure 4.13: Longitudinal thermal expansion of 55 v/o P100 Gr/Cu. Uniform fiber distribution and the two cylinder arrangements are shown for stress-free temperatures of 100 °F and 1700 °F.

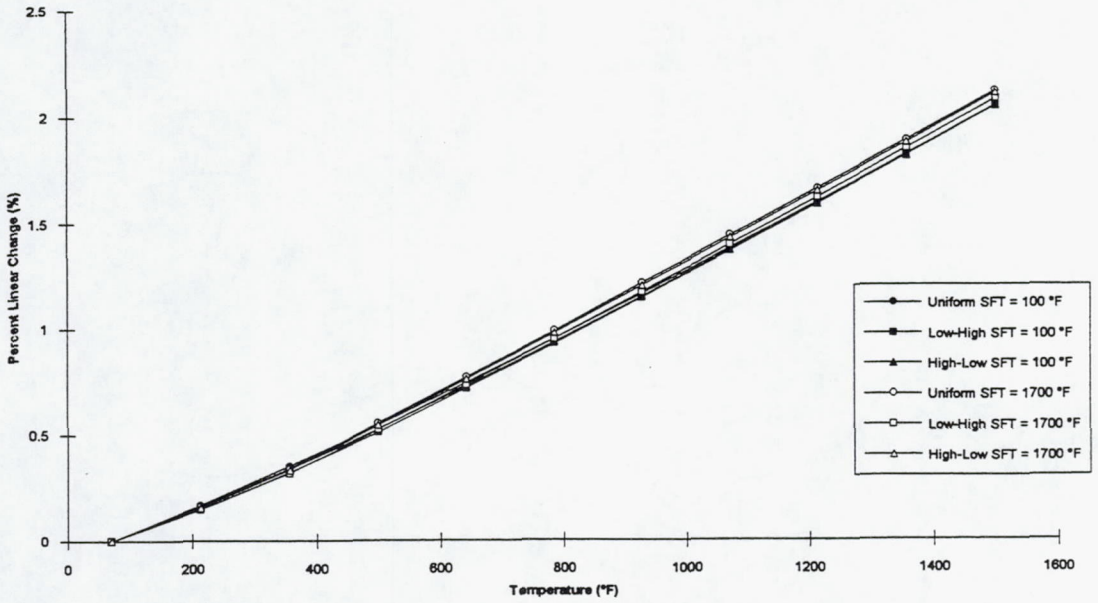

Figure 4.14: Transverse thermal expansion of 55 v/o P100 Gr/Cu. Uniform fiber distribution and the two cylinder arrangements are shown for stress-free temperatures of 100 °F and 1700 °F.

microstructure. Thus, this type of radially nonuniform fiber distribution appears not to be of great importance to the thermal expansion of Gr/Cu.

In an attempt to determine under what circumstances radially nonuniform fiber distribution may have a significant effect on the thermal expansion response of a composite, a parametric study was performed using CCMICRON. First, the Young's modulus of the fiber was taken to be isotropic using the value of the axial Young's modulus. This produces a much larger Young's modulus mismatch between the fiber and the matrix in the transverse direction than is the case using the transversely isotropic properties. The thermal expansion response for this case is shown in Figures 4.15 and 4.16. The effect of the fiber nonuniformity is much more evident for this case in both directions and for both stress-free temperatures. In the transverse direction the magnitude of the effect is now approximately the same as the magnitude of the effect of the stress-free temperature variation. It is also apparent that the Low-High configuration has a greater effect than does the High-Low configuration.

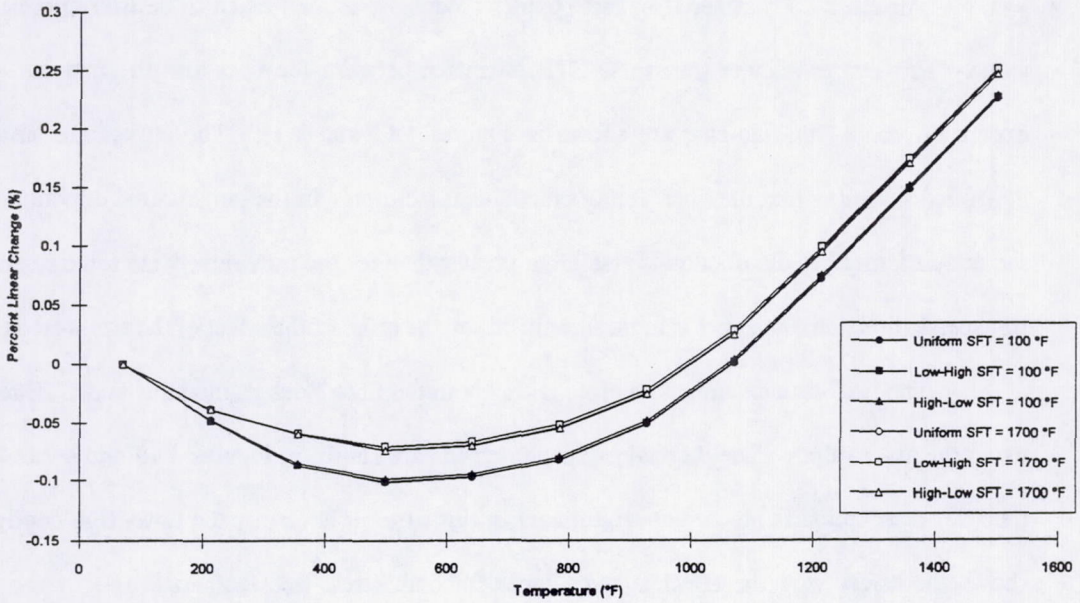

Figure 4.15: Longitudinal thermal expansion of 55 v/o P100 Gr/Cu with the fiber Young's modulus taken to be isotropic. Uniform fiber distribution and the two cylinder arrangements are shown for stress-free temperatures of 100 °F and 1700 °F.

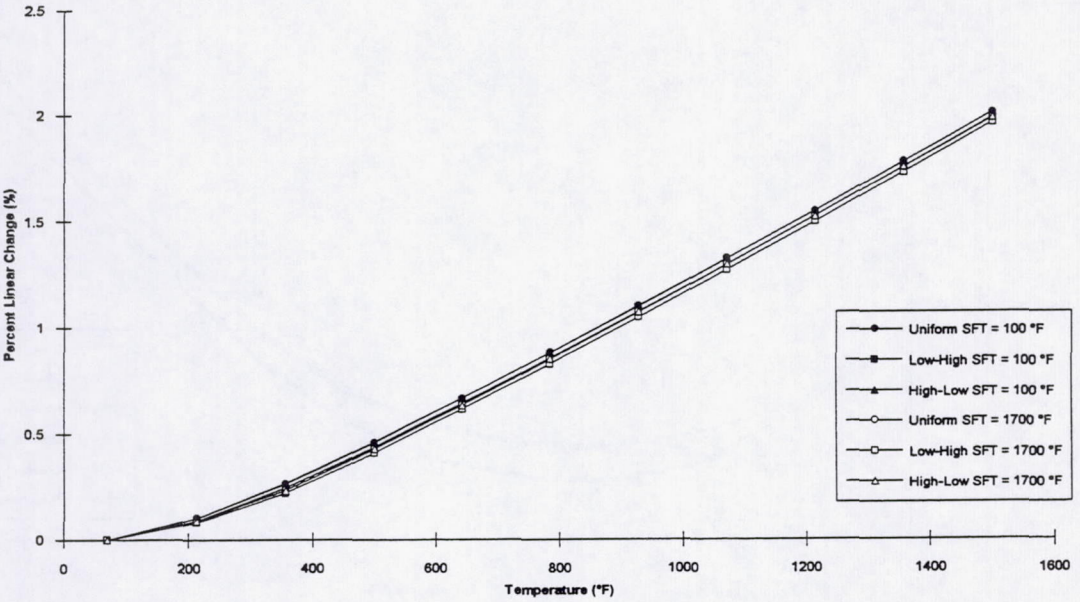

Figure 4.16: Transverse thermal expansion of 55 v/o P100 Gr/Cu with the fiber Young's modulus taken to be isotropic. Uniform fiber distribution and the two cylinder arrangements are shown for stress-free temperatures of 100 °F and 1700 °F.

The fiber CTE rather than the Young's modulus was then taken to be isotropic using the axial value. This causes a large transverse CTE mismatch between the fiber and the matrix. The thermal expansion curves for this case are shown in Figures 4.17 and 4.18. The curves are similar to those generated assuming that the fiber Young's modulus is isotropic. In the longitudinal direction, the effect of the nonuniform fiber distribution is small, but greater than for the transversely isotropic fiber case. In the transverse direction, the effect is more significant; on the order of the effect of the stress-free temperature.

The final case examined involved taking both the fiber Young's modulus and CTE to be isotropic using the axial values. The thermal expansion results are shown in Figures 4.19 and 4.20. The effect of the fiber distribution is much more significant in this case. It is mainly the Low-High configuration that shows the effect, and the effect is quite large for both stress-free temperatures. In the longitudinal direction the effect of the nonuniform fiber distribution is nearly as great as the effect of the stress-free temperature, while in the transverse direction, it is much greater. Since the effect of the nonuniform fiber

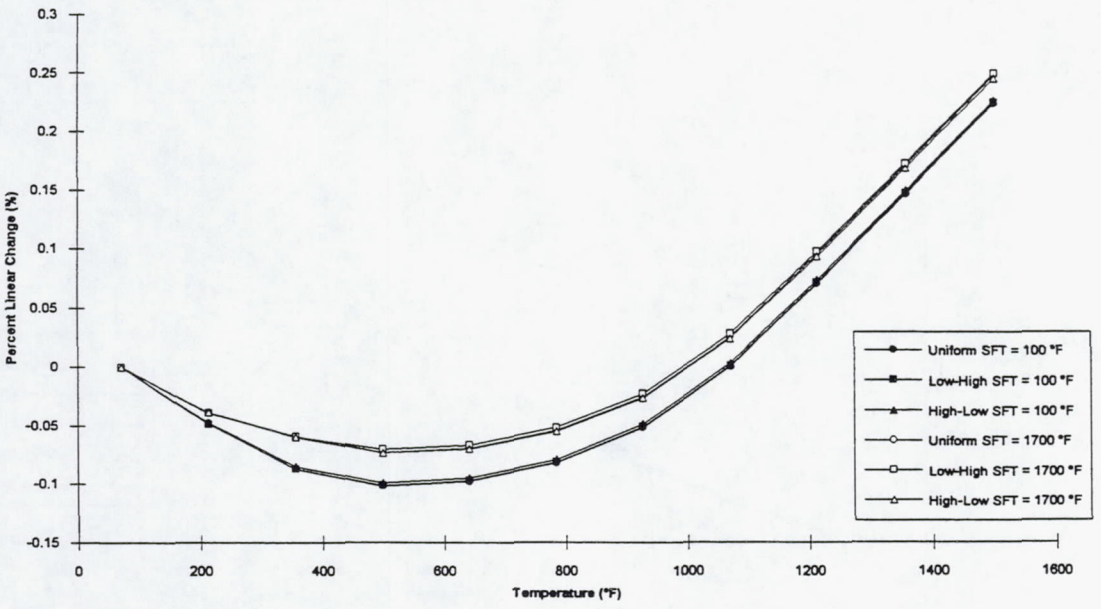

Figure 4.17: Longitudinal thermal expansion of 55 v/o P100 Gr/Cu with the fiber CTE taken to be isotropic. Uniform fiber distribution and the two cylinder arrangements are shown for stress-free temperatures of 100 °F and 1700 °F.

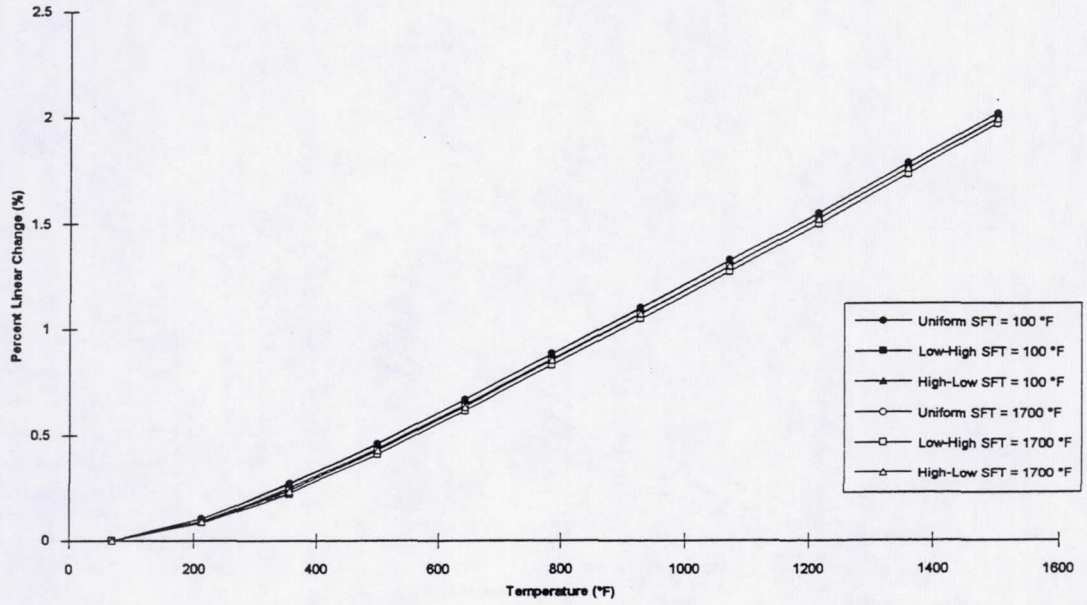

Figure 4.18: Transverse thermal expansion of 55 v/o P100 Gr/Cu with the fiber CTE taken to be isotropic. Uniform fiber distribution and the two cylinder arrangements are shown for stress-free temperatures of 100 °F and 1700 °F.

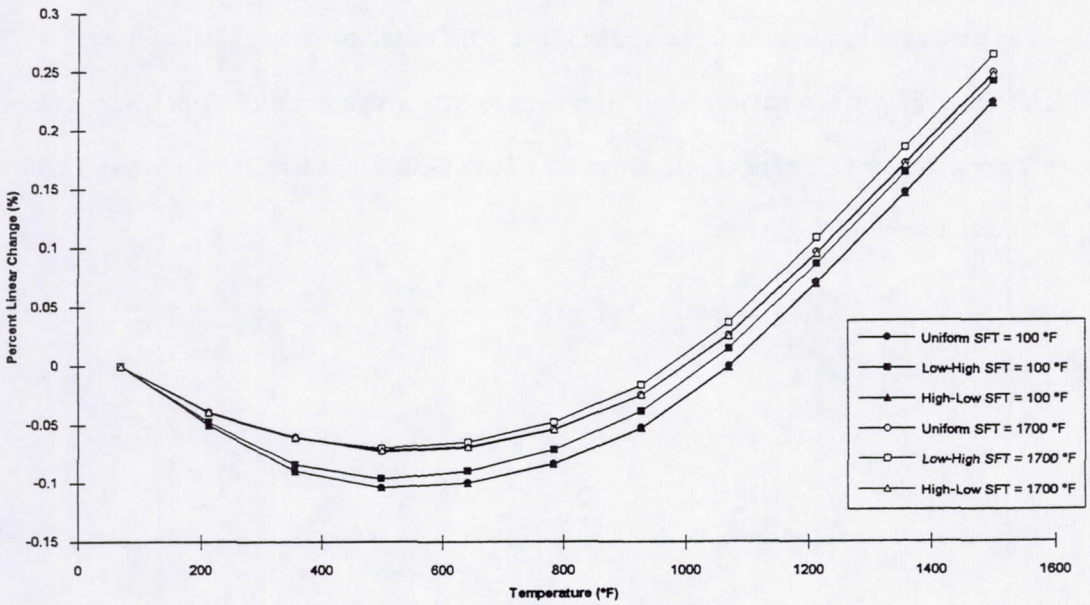

Figure 4.19: Longitudinal thermal expansion of 55 v/o P100 Gr/Cu with the fiber Young's Modulus and CTE taken to be isotropic. Uniform fiber distribution and the two cylinder arrangements are shown for stress-free temperatures of 100 °F and 1700 °F.

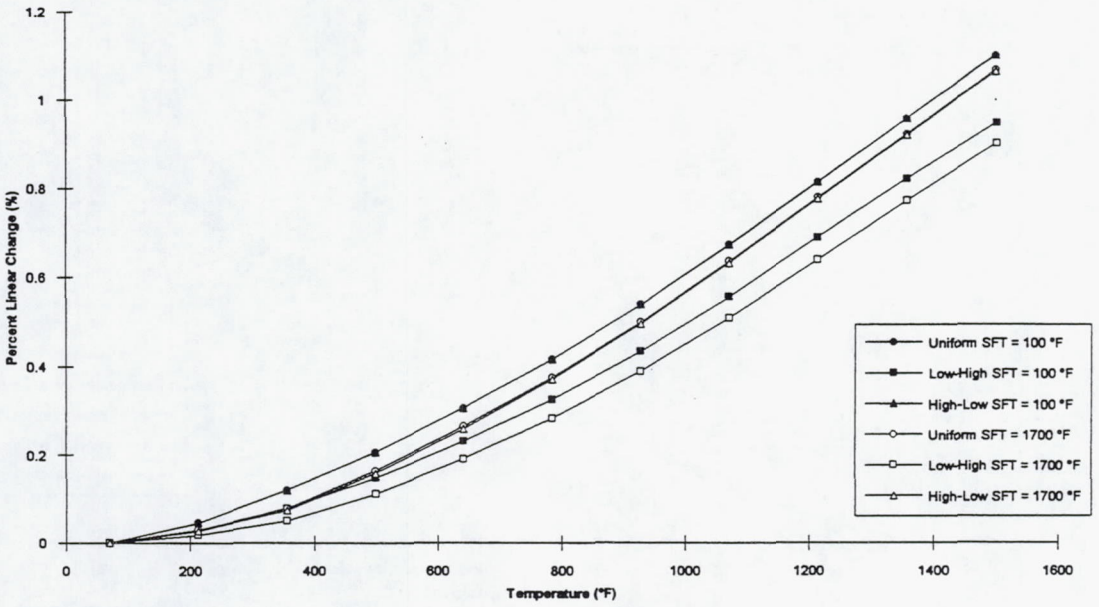

Figure 4.20: Transverse thermal expansion of 55 v/o P100 Gr/Cu with the fiber Young's Modulus and CTE taken to be isotropic. Uniform fiber distribution and the two cylinder arrangements are shown for stress-free temperatures of 100 °F and 1700 °F.

distribution was small when just the fiber Young's modulus or the fiber CTE were taken to be isotropic, it can be concluded that some sort of coupling between the transverse Young's modulus and CTE exists. In order for a radially nonuniform fiber distribution to have a significant effect on the thermal expansion behavior of the Gr/Cu composite, there must be a large mismatch in both the transverse Young's modulus and the transverse CTE.

4.4.2 MCLAM

One of the effects that MCLAM can be used to examine is variation in the fiber volume fraction of a composite laminate in the through-thickness direction. As was the case with CCMICRON, an arbitrary number of layers can be used, so the variation in fiber volume fraction can be as continuous as desired. To examine the effect that this type of through-thickness fiber distribution nonuniformity has on the thermal expansion, it is necessary to compare the thermal expansion of a nonuniform composite with a uniform composite with the same average fiber volume fraction. To this end, the first six laminates shown in Figure 4.21 were considered (the last two will be addressed in Section 4.5).

The laminates Lam 1 through Lam 6 were divided into layers with 0.1931 and 0.9069 fiber volume fractions such that the average laminate fiber volume fraction was 0.55 in all six cases. As before, 0.9069 was chosen because it is an upper bound on the fiber volume fraction of a composite with unidirectional cylindrical fibers, while 0.1931 was chosen to produce a composite with an average fiber volume fraction of 0.55 when the composite was divided into equal parts of each fiber volume fraction. These fiber volume fractions represent an extreme case since a region cannot have a fiber volume fraction greater than 0.9069, and a fiber volume fraction of 0.1931 is quite low for a material such as Gr/Cu. Lam 4 has additional layers with fiber volume fractions of 0.65 and 0.45 separating the layers with the two extreme fiber volume fractions in order to simulate a more gradual change in the fiber distribution.

Lam 1 represents the most extreme case examined. The regions with high and low fiber volume fractions are large and continuous, and the change in fiber volume fraction is abrupt. In Lam 2 and Lam 3, the transitions from regions of high and low fiber volume fraction are equally as abrupt, but the regions are separated into four and six alternating layers rather than just two. On the macro scale, Lam 2 and Lam 3 appear much more uniform than does Lam 1. It should be noted that these three laminates are non symmetric, with non-zero B matrices (see equation 3.27). Thus bending-stretching coupling will occur when the laminates are subjected to a temperature change.

Predicted longitudinal and transverse thermal expansion curves for Lam 1, Lam 2, and Lam 3 are shown in Figures 4.22 and 4.23 along with the uniformly distributed 0.55 fiber volume fraction case. Since bending does occur, the average change in length is reported. Figure 4.22 shows that the

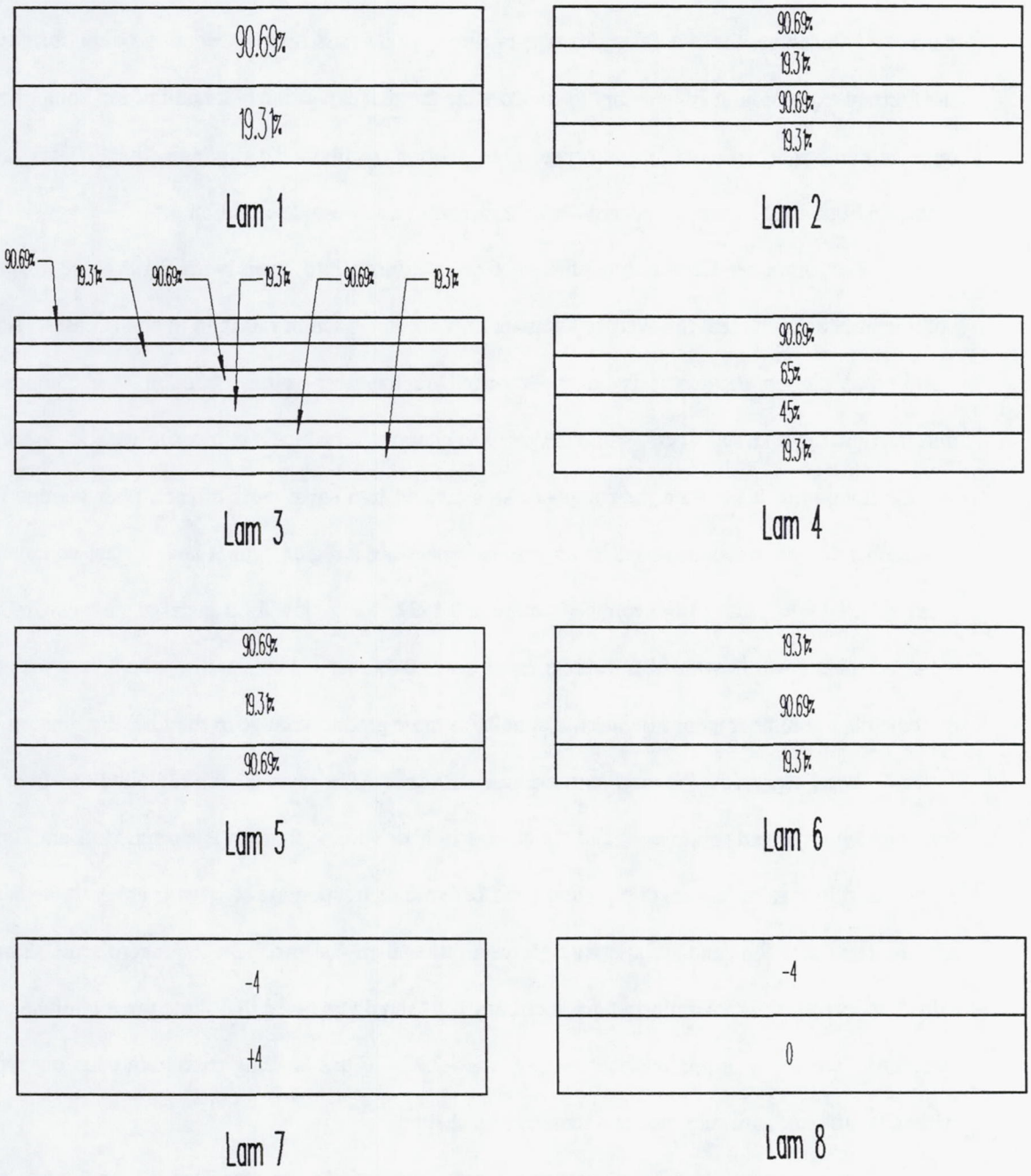

Figure 4.21: Laminate configurations.

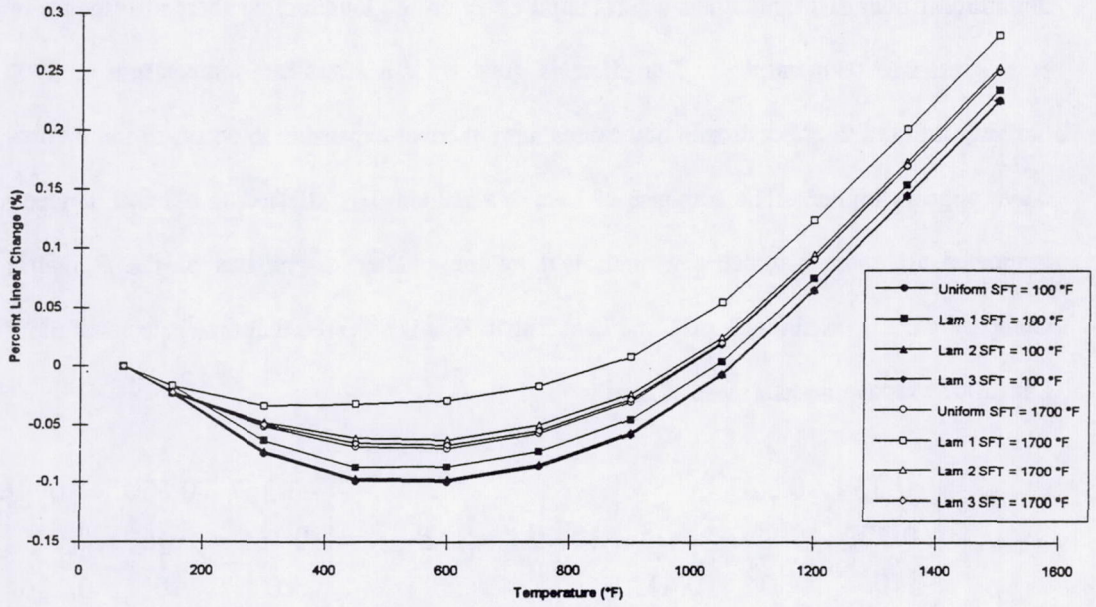

Figure 4.22: Longitudinal thermal expansion of 55 v/o P100 Gr/Cu. Uniform fiber distribution and laminate configurations with one, two, and three sets of high V_f and low V_f laminae are shown.

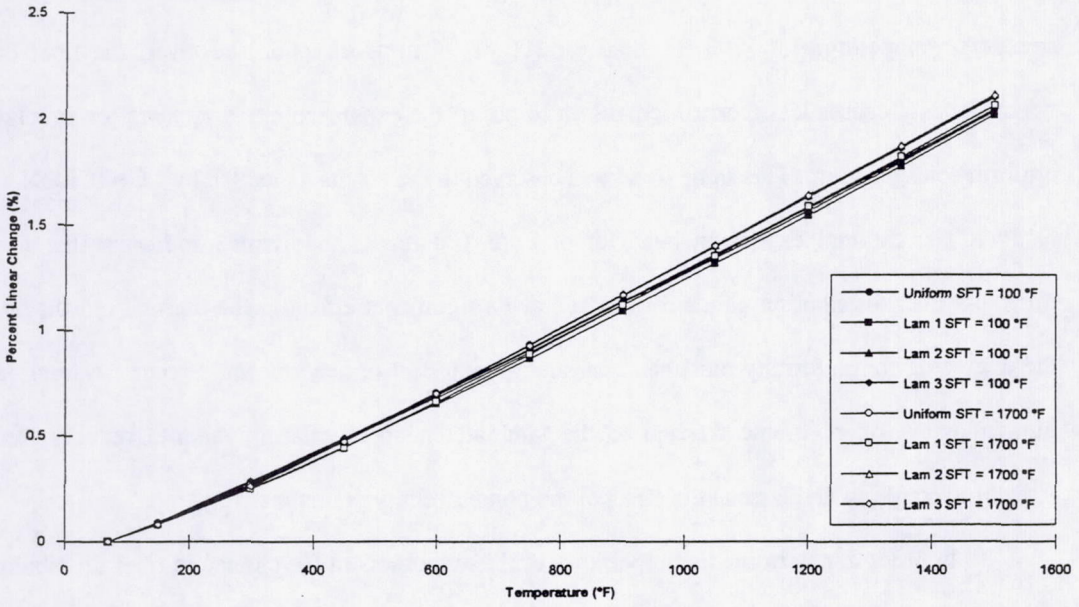

Figure 4.23: Transverse thermal expansion of 55 v/o P100 Gr/Cu. Uniform fiber distribution and laminate configurations with one, two, and three sets of high V_f and low V_f laminae are shown.

nonuniform fiber distribution has a substantial effect on the longitudinal thermal response of Lam 1 for both stress-free temperatures. The effect is greater for a stress-free temperature of 1700 °F. The nonuniformity in the fiber distribution causes more thermal expansion to occur, so the thermal expansion curve appears higher. The response of Lam 2 and Lam 3 is affected to a lesser degree since these laminates are more symmetric as indicated by the smaller magnitudes of the B matrix elements. Comparing the B matrix for Lam 1 and Lam 2 at 70 °F it is observed that the elements of the B matrix for Lam 2 are exactly one-half those of Lam 1:

$$B_{Lam1} = \begin{bmatrix} -7.134 & 0.320 & 0 \\ 0.320 & 0.920 & 0 \\ 0 & 0 & 0.412 \end{bmatrix} \cdot 10^6 \ lb_f \qquad B_{Lam2} = \begin{bmatrix} -3.567 & 0.160 & 0 \\ 0.160 & 0.460 & 0 \\ 0 & 0 & 0.206 \end{bmatrix} \cdot 10^6 \ lb_f .$$

However, as shown in Figures 4.22 and 4.23, the effect of this difference on the thermal expansion is much more than a factor of two. For a stress-free temperature of 100 °F, the predicted thermal expansion curves for Lam 2 and Lam 3 show almost no difference from the uniform case.

In the transverse direction (Figure 4.23), the trend is similar. Lam 1 exhibits a noticeable deviation from the uniform case, whereas Lam 2 and Lam 3 do not. The effect is more noticeable for a stress-free temperature of 1700 °F than for 100 °F. In this direction, however, the fiber distribution nonuniformity causes less thermal expansion to occur; the expansion curve appears lower relative to the uniform configuration. This same trend was observed in the results generated by CCMICRON.

The thermal expansion behavior of Lam 1, Lam 2, and Lam 3 indicates that for through-thickness fiber distribution nonuniformity to have a significant effect on the thermal expansion behavior, the degree of nonuniformity must be great, and a great deal of bending must occur. Adding layers with high and low fiber volume fraction to the laminate in an alternating manner reduces the bending-stretching coupling and lessens the effect of the nonuniformity dramatically.

In order to determine the importance of the abruptness in the change in fiber distribution, Lam 4 was considered. It represents the same overall fiber volume fraction, and the same overall change in fiber volume fraction as Lam 1, but the change is more gradual. The thermal expansion of Lam 4 is shown in

Figures 4.24 and 4.25. The thermal expansion of the uniform laminate and Lam 1 are also plotted for comparison. The figures show that the effect of the nonuniform fiber distribution is lessened when the change is more gradual, but the effect is still significant. Examining the elements of the B matrix for Lam 4 at 70 °F shows that they are approximately 80% as large as the elements of the B matrix for Lam 1:

$$B_{Lam\,4} = \begin{bmatrix} -5.851 & 0.261 & 0 \\ 0.261 & 0.749 & 0 \\ 0 & 0 & 0.336 \end{bmatrix} \cdot 10^6 \; lb_f .$$

Thus, introducing layers to create a more gradual change in the fiber distribution produces a substantially different result than refining the microstructure by adding increasingly thinner layers in an alternating fashion, as was the case with Lam 2 and Lam 3.

To determine what effect nonuniform fiber distribution has on the thermal expansion of symmetric Gr/Cu laminates, Lam 5 and Lam 6 were considered. Lam 5 has low fiber volume fraction in

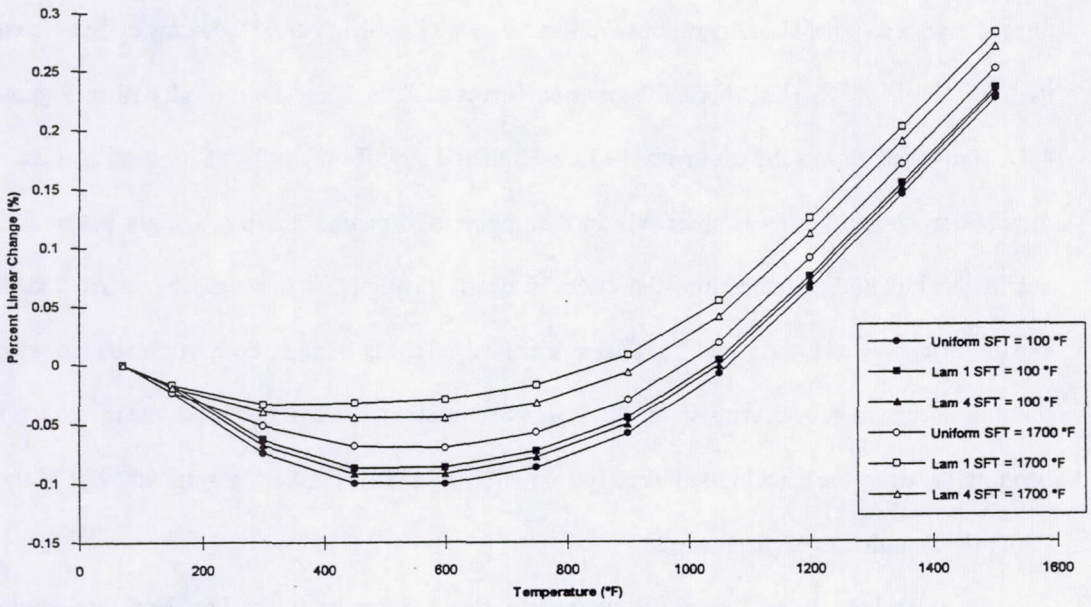

Figure 4.24: Longitudinal thermal expansion of 55 v/o P100 Gr/Cu. Uniform fiber distribution and laminate configurations with an abrupt change in V_f, and a more gradual change in V_f are shown.

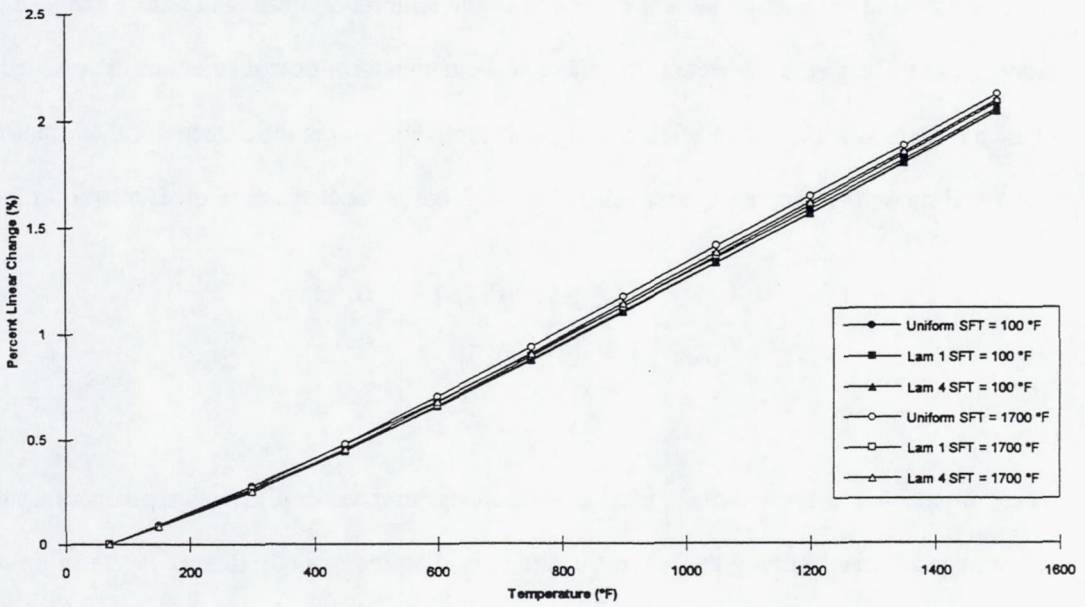

Figure 4.25: Transverse thermal expansion of 55 v/o P100 Gr/Cu. Uniform fiber distribution and laminate configurations with an abrupt change in $V_{f,}$ and a more gradual change in V_f are shown.

the middle plies and high fiber volume fraction in the outer plies, while in Lam 6 the arrangements of the plies is reversed. These configurations are similar to the Low-High and High-Low cylinder configurations used in CCMICRON. The thermal expansion curves of Lam 5 and Lam 6, plotted in Figures 4.26 and 4.27, show that, as was the case with the Low-High and High-Low configurations, little effect of the fiber distribution nonuniformity is observed. In the transverse direction, there is a slight but noticeable effect, but in the longitudinal direction, the effect is nearly negligible. It should be noted that the thermal expansion curves of Lam 5 and Lam 6 are identical. This is because both laminates are symmetric, so there is no bending, and because all the layers are unidirectional, there is no shear. Since there is no bending or shear, the stacking sequence has no effect on the thermal expansion behavior of the laminates under the assumption of plane stress.

Since Lam 5 and Lam 6 are symmetric, they are similar to the Low-High and High-Low cases respectively, generated with CCMICRON. Figures 4.28 - 4.31 compare Lam 5 and Lam 6 to the Low-High and High-Low cases. As the figures show, the thermal expansion response of these cases are very

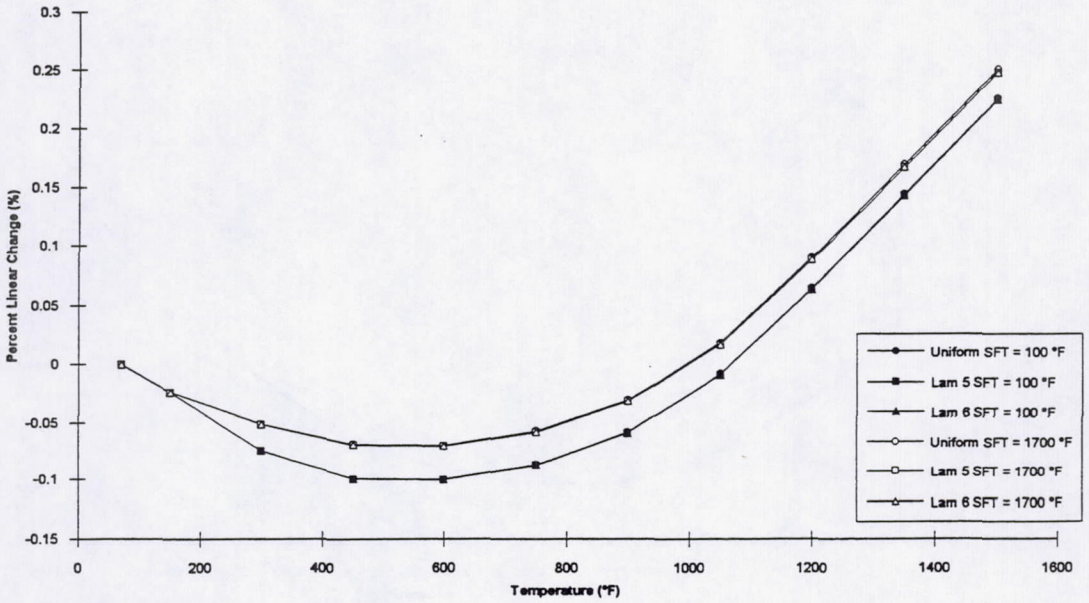

Figure 4.26: Longitudinal thermal expansion of 55 v/o P100 Gr/Cu laminates with uniform and symmetrically arranged fiber distribution.

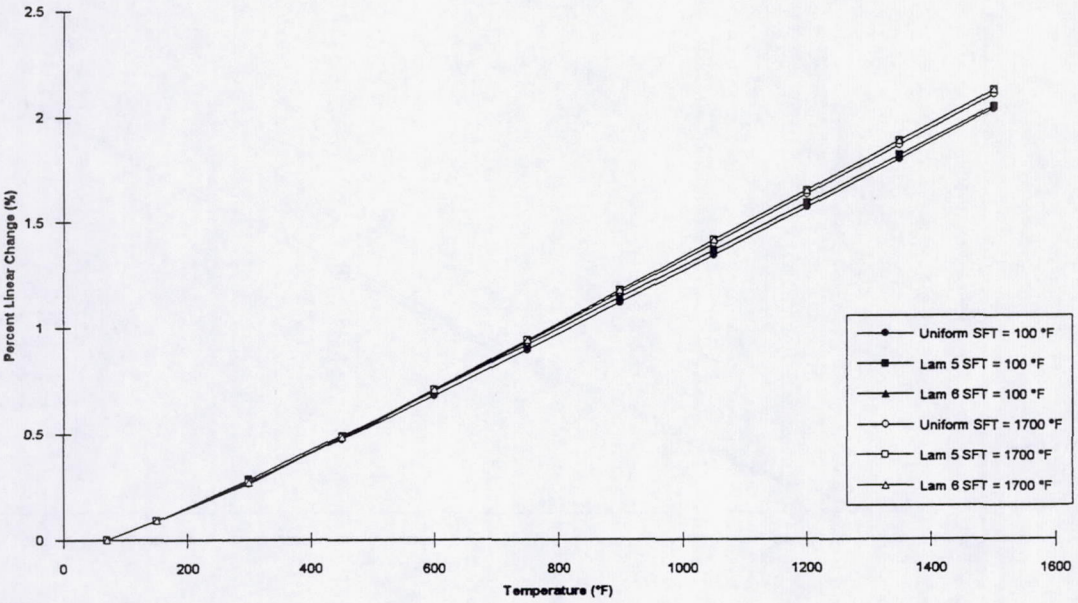

Figure 4.27: Transverse thermal expansion of 55 v/o P100 Gr/Cu laminates with uniform and symmetrically arranged fiber distribution.

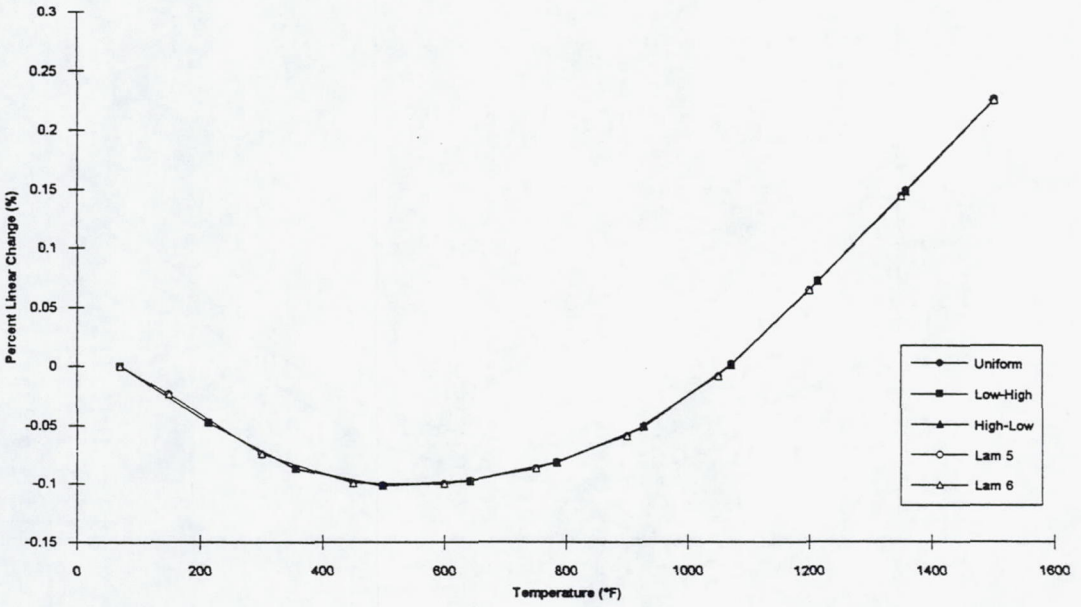

Figure 4.28: Longitudinal thermal expansion of 55 v/o P100 Gr/Cu using a stress-free temperature of 100 °F. Uniform, Low-High, and High-Low cases generated with CCMICRON are shown along with two symmetric cases generated with MCLAM.

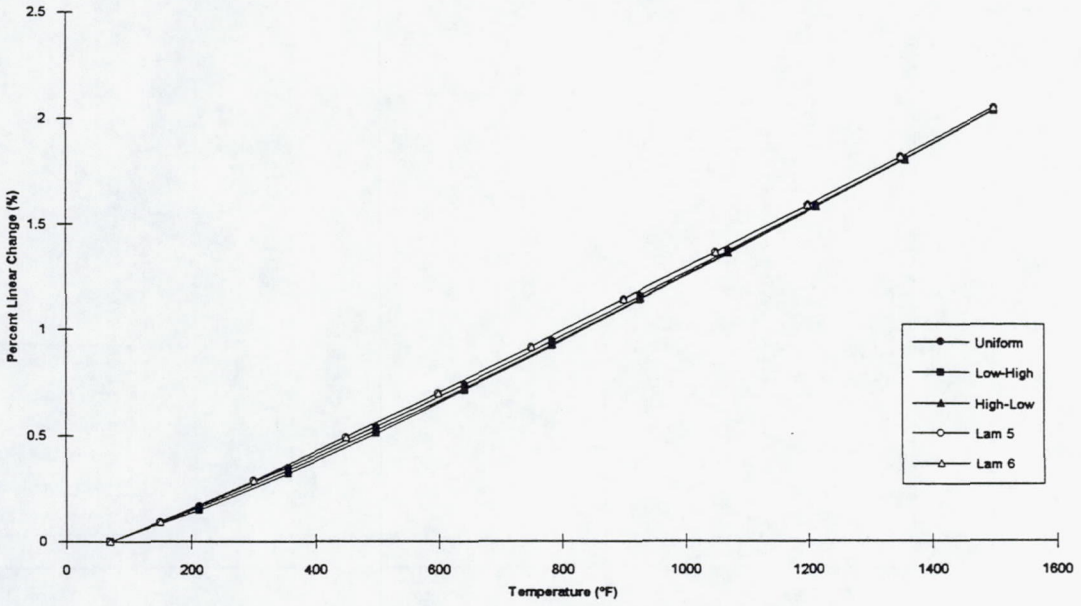

Figure 4.29: Transverse thermal expansion of 55 v/o P100 Gr/Cu using a stress-free temperature of 100 ° F. Uniform, Low-High, and High-Low cases generated with CCMICRON are shown along with two symmetric cases generated with MCLAM.

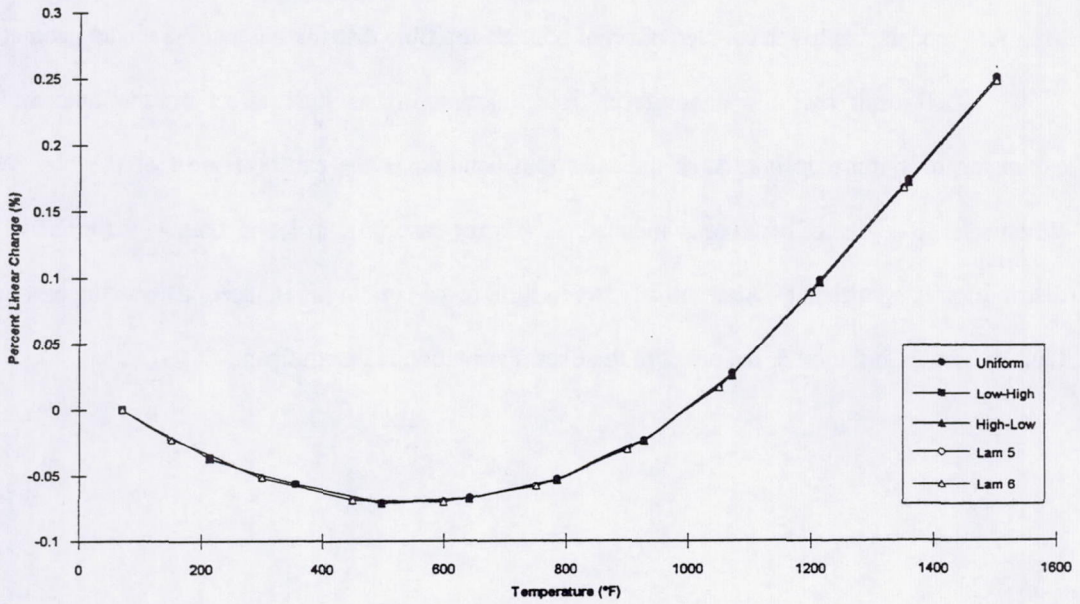

Figure 4.30: Longitudinal thermal expansion of 55 v/o P100 Gr/Cu using a stress-free temperature of 1700 °F. Uniform, Low-High, and High-Low cases generated with CCMICRON are shown along with two symmetric cases generated with MCLAM.

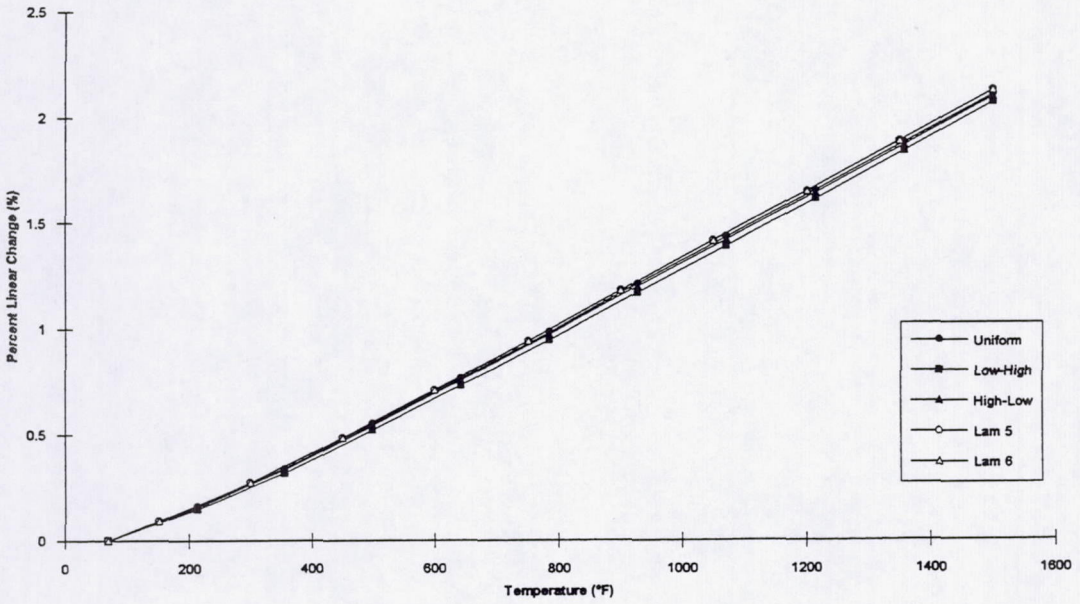

Figure 4.31: Transverse thermal expansion of 55 v/o P100 Gr/Cu using a stress-free temperature of 1700 ° F. Uniform, Low-High, and High-Low cases generated with CCMICRON are shown along with two symmetric cases generated with MCLAM.

similar. The slight differences are due to the different states of stress predicted by the CCMICRON and MCLAM models due to the coupled effect of nonuniform fiber distribution and the model geometries

The result that the nonuniform fiber distribution has little effect on the predicted thermal expansion of symmetric laminates indicates that bending is the cause of most of the observed effect. When a large degree of bending is induced, as was the case in Lam 1 and Lam 4, the effect of the fiber distribution is significant. Alternatively, when little or no bending is induced, as was the case in Lam 2, Lam 3, Lam 5, and Lam 6, the effect of the fiber distribution is insignificant.

4.5 Effect of Fiber Misalignment

The laminates Lam 7 and Lam 8 shown in Figure 4.21 were considered in order to examine the effect of a slight fiber misalignment or rotation in a layer thought to be a 0° layer. Figures 4.32 and 4.33 show the thermal expansion of these laminates. In the longitudinal direction, the thermal expansion of both configurations is noticeably different from that of the uniform laminate for a stress-free temperature of 1700 °F. These laminates exhibit more longitudinal expansion than the uniform laminate because the fibers are not providing as much restraint in the longitudinal direction due to the slight misalignment. The effect becomes much less noticeable for a stress-free temperature of 100 °F.

In the transverse direction, the effect of the angle misalignment becomes more noticeable at a stress-free temperature of 100 °F. For a stress-free temperature of 1700 °F, the effect is negligible. This is the reverse of the trend in the longitudinal direction. In addition, the transverse response indicates that the [±4°] configuration of Lam 7 has a greater effect than the [-4°/0°] configuration of Lam 8. This

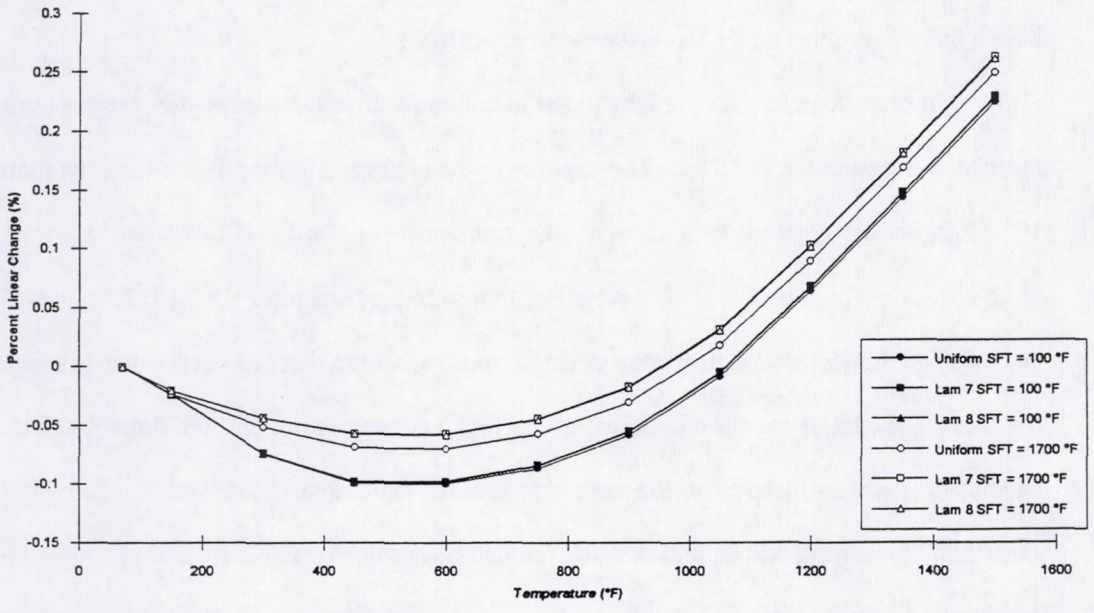

Figure 4.32: Longitudinal thermal expansion of 55 v/o P100 Gr/Cu. Uniform fiber distribution and two laminates with slight fiber misalignment are shown.

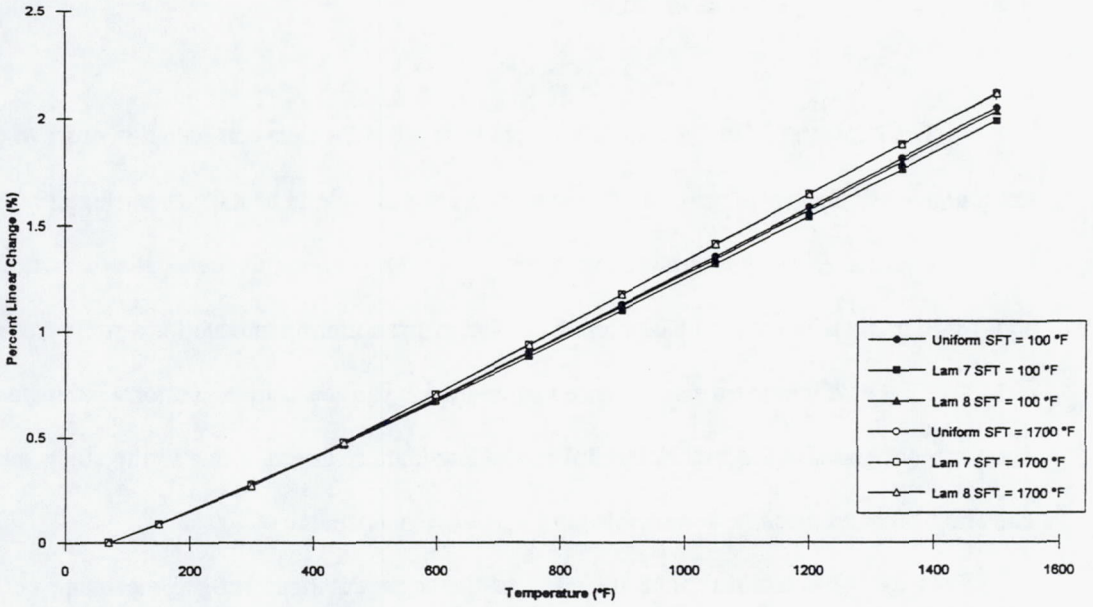

Figure 4.33: Transverse thermal expansion of 55 v/o P100 Gr/Cu. Uniform fiber distribution and two laminates with slight fiber misalignment are shown.

differs from the longitudinal response in which the thermal expansion curves of Lam 7 and Lam 8 are nearly identical. Clearly, Figures 4.32 and 4.33 indicate that in some cases slight angle misalignment can have a noticeable effect on the thermal expansion of Gr/Cu.

In order to better explain why in the longitudinal direction a stress-free temperature of 1700 °F resulted in a greater deviation from the response of the uniform laminate than a stress-free temperature of 100 °F, with the opposite being true in the transverse direction, MCLAM was used to model five symmetric angle-ply laminates. The laminates that were modeled are $[\pm 15°]_S$, $[\pm 30°]_S$, $[\pm 45°]_S$, $[\pm 60°]_S$, and $[\pm 75°]_S$. In addition, a component of the thermal expansion that has not previously been addressed is the through-thickness expansion. In cases in which no shear is present, the through-thickness thermal expansion is almost identical to the transverse thermal expansion. However, in angle-ply laminates, a great deal of shearing occurs, and thus the through-thickness thermal expansion for these laminates will be presented as well.

Figures 4.34 and 4.35 show the longitudinal thermal expansion for the symmetric laminates for the two stress-free temperatures. Figure 4.34 shows that for a stress-free temperature of the 100 °F, the longitudinal thermal expansion is relatively insensitive to changes in the angle for the lower angle-ply configurations. Figure 4.35 shows that the same is true for a stress-free temperature of 1700 °F, but there is clearly more of an effect at these lower ply angles than for a stress-free temperature of 100 °F. At the higher ply angles, the reverse is true. The thermal expansion behavior generated using a stress-free temperature of 100 °F is more sensitive to changes in the off-axis angle for these higher ply angles. This explains why for a small angle misalignment a greater effect was observed in the longitudinal direction than the transverse direction for a stress-free temperature of 1700 °F, while the opposite was observed for a stress-free temperature of 100 °F.

Figures 4.36 and 4.37 show the through-thickness thermal expansion of the laminates for the two stress-free temperatures. It should be noted that the through-thickness response of a $[\pm\theta]_S$ laminate is the same as the response of a $[\pm(90\text{-}\theta)]_S$. This is because these laminates are identical in the through-

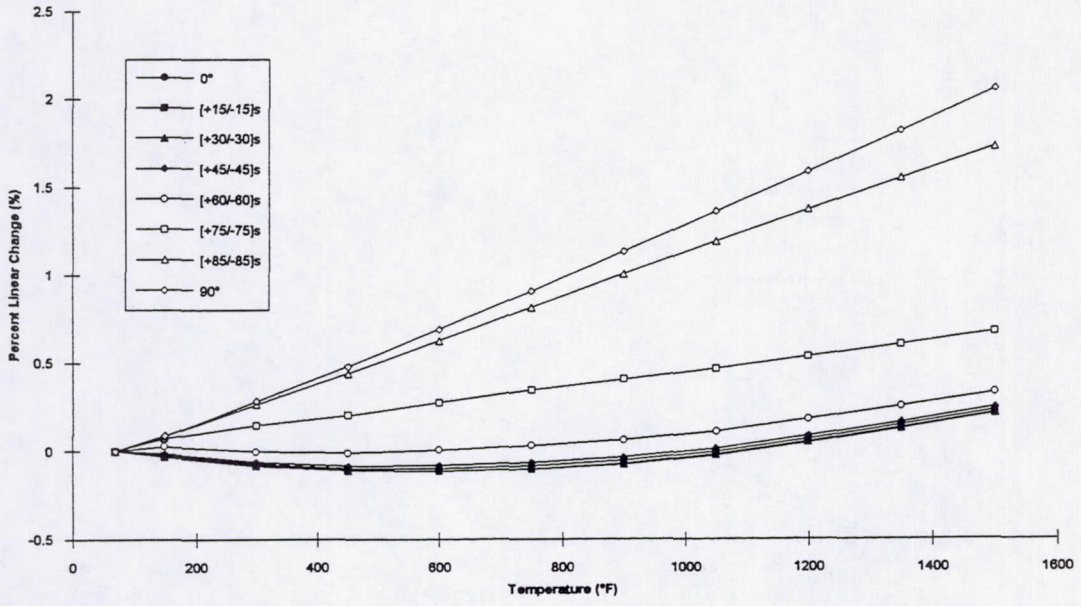

Figure 4.34: Longitudinal thermal expansion of 50 v/o symmetric angle ply P100 Gr/Cu using a stress-free temperature of 100 °F.

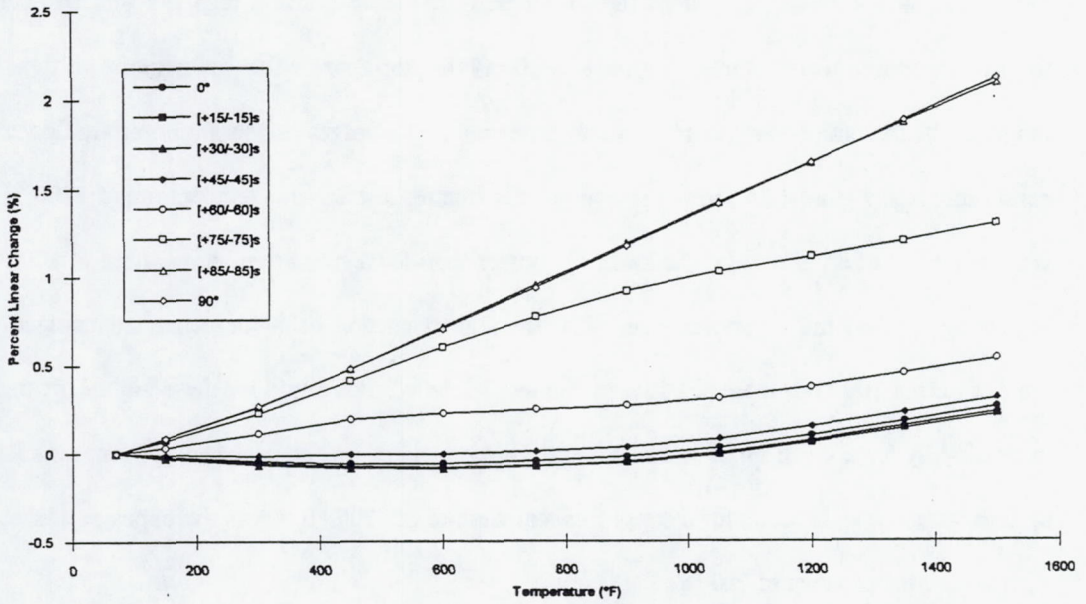

Figure 4.35: Longitudinal thermal expansion of 50 v/o symmetric angle ply P100 Gr/Cu using a stress-free temperature of 1700 °F.

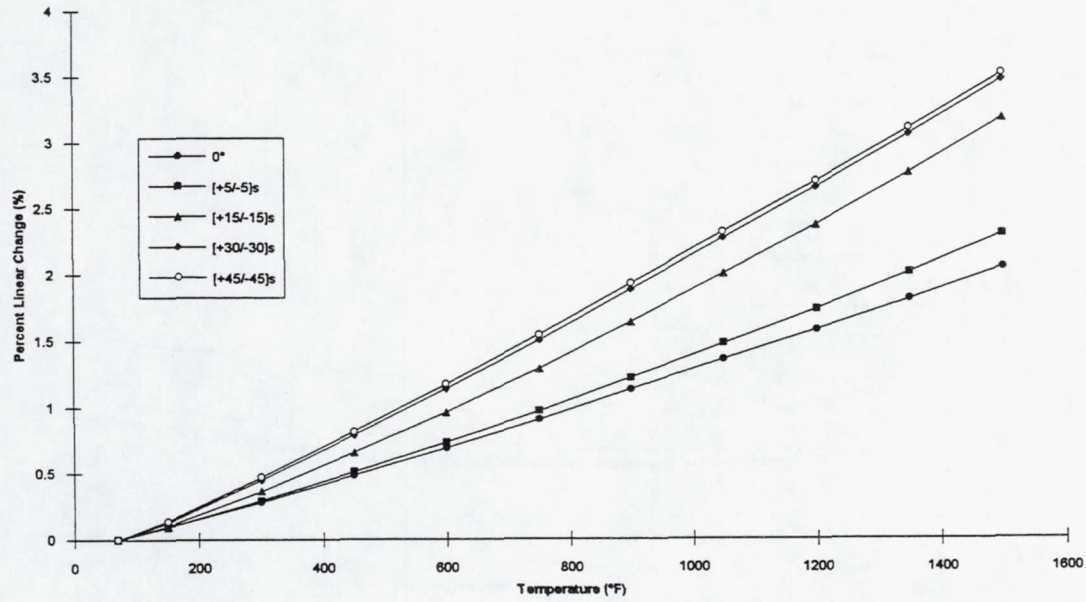

Figure 4.36: Through-thickness thermal expansion of 50 v/o symmetric angle ply P100 Gr/Cu using a stress-free temperature of 100 °F.

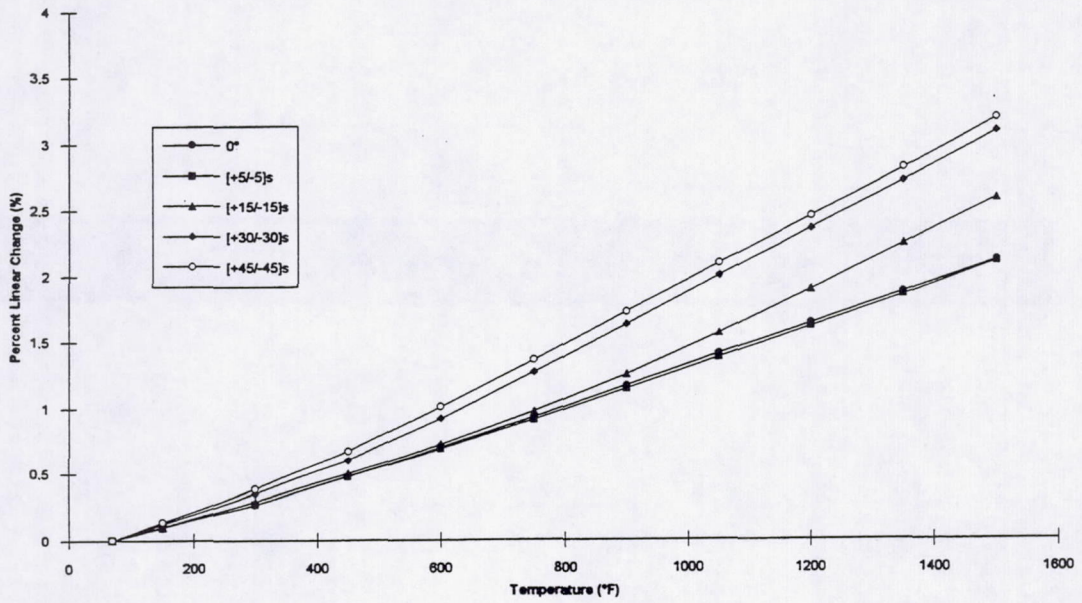

Figure 4.37: Through-thickness thermal expansion of 50 v/o symmetric angle ply P100 Gr/Cu using a stress-free temperature of 1700 °F.

thickness direction. Thus, for example, the response of the $[\pm 15]_S$ laminate also represents the response of a $[\pm 75]_S$ laminate.

Unlike the longitudinal thermal expansion, the through-thickness thermal expansion of each laminate is greater for a stress-free temperature of 100 °F than it is for 1700 °F. For both stress-free temperatures, the through-thickness thermal expansion is low for high and low ply angles, and it attains a maximum at a ply angle value of 45°. At this peak value, the through-thickness thermal expansion is much greater than the transverse thermal expansion of the 0° configuration, which is the same in the through-thickness direction. In addition, significant changes in the through-thickness thermal expansion occur with relatively small changes in the ply angle for the lower angle ply configurations.

5. Correlation with Experiment

It has been shown in the previous chapter that matrix plasticity, choice of stress-free temperature, nonuniform fiber distribution, and fiber misalignment affect the thermal expansion of Gr/Cu to various degrees. This chapter presents comparison between the predicted response obtained from the developed models in the presence of these effects and experimentally-measured thermal expansion data. Since the actual microstructure of Gr/Cu is better modeled as a laminate with layers of different fiber volume fraction than an assemblage of cylinders, MCLAM will be used exclusively in this chapter.

In addition to monotonic thermal loading, a comparison is also made between the predicted and experimental cyclic thermal expansion of Gr/Cu. A discussion of potential factors that may be causing discrepancy between the predicted and measured response of the composite is also included.

5.1 Monotonic Thermal Expansion

One of the objectives of this investigation was to develop models to simulate the experimentally observed thermal expansion of Gr/Cu in the presence of nonuniform fiber distribution. It was shown in Chapter 4 that the radial fiber distribution nonuniformity modeled with CCMICRON did not have a significant effect on the thermal expansion behavior of Gr/Cu. Furthermore, as will be shown, the actual fiber distribution in Gr/Cu does not exhibit radial character. Thus modeling actual Gr/Cu thermal expansion specimens using CCMICRON is not appropriate for this particular composite system. In real Gr/Cu, areas of high and low fiber volume fraction can be approximated by layers or plies. This is one of the reasons that MCLAM was developed; to model the actual microstructure of Gr/Cu thermal expansion specimens.

For the purpose of this investigation, three longitudinal and two transverse thermal expansion specimens were tested. The tests were performed by S.M. DeVincent at NASA Lewis Research Center. A single push-rod dilatometer was used. Micrographs of the cross sections of the specimens perpendicular to the fiber direction are shown in Figures 5.1 - 5.5. While the entire cross section is shown for the longitudinal specimens, only a portion of the cross section is displayed for the transverse specimens. The longitudinal specimens are designated d7-0, d8-0, and d10-0, and the transverse specimens are designated d1-90 and d2-90.

The longitudinal specimens exhibit a great deal of fiber distribution nonuniformity. The large white areas in Figures 5.1, 5.2, and 5.3 are regions of pure copper where there are literally no fibers. In contrast, the two transverse specimens have a much more uniform fiber distribution. This is due to the fact that the longitudinal and transverse specimens were cut from different Gr/Cu plates. Clearly, the longitudinal specimens lend themselves much more readily to be modeled as laminates rather then concentric cylinders. It should be noted that 0.1 weight percent of chromium was added to the copper matrix to ensure a good bond between the fiber and matrix. It was determined that this chromium, which collects at the interface, does not significantly affect the properties of the individual phases.

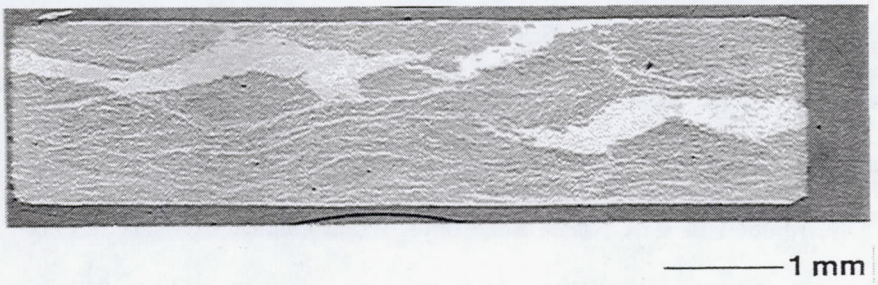

Figure 5.1: Micrograph of specimen d7-0. Courtesy of S.M. DeVincent.

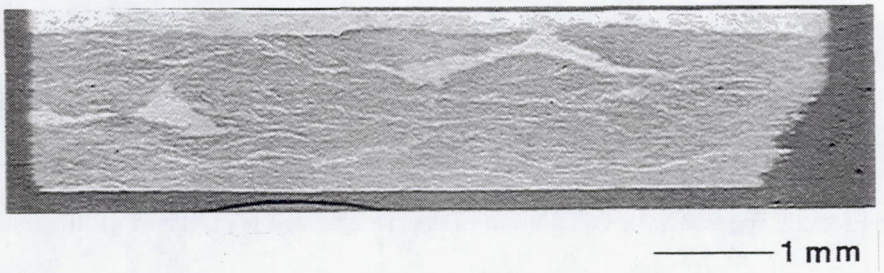

Figure 5.2: Micrograph of specimen d8-0. Courtesy of S.M. DeVincent.

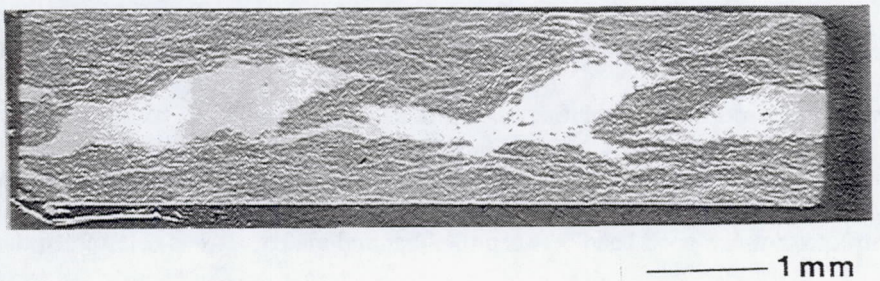

Figure 5.3: Micrograph of specimen d10-0. Courtesy of S.M. DeVincent.

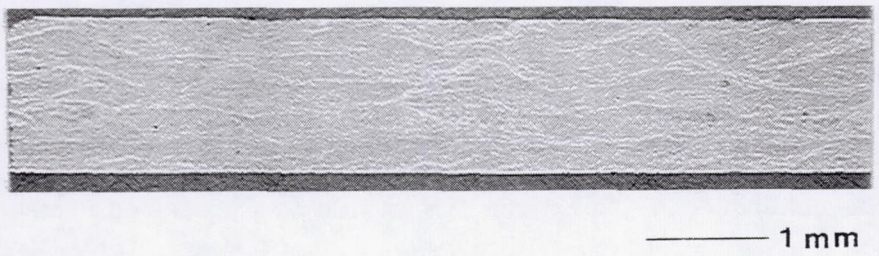

Figure 5.4: Micrograph of a portion of specimen d1-90. Courtesy of S.M. DeVincent.

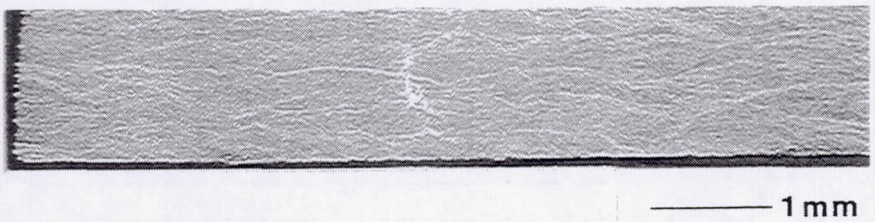

Figure 5.5: Micrograph of a portion of specimen d2-90. Courtesy of S.M. DeVincent.

Figure 5.6 indicates how the longitudinal specimens were partitioned into layers for modeling purposes. The thickness and fiber volume fraction of each layer are indicated in the figure. The layer dimensions are based on a total laminate thickness of unity. The method by which the longitudinal specimens were divided into layers was visual. An attempt was made to isolate layers with large regions of pure copper. After each specimen was partitioned, layers without any large regions of copper were taken to have a fiber volume fraction of 0.75. This value approximates the maximum fiber volume fraction that has been achieved for Gr/Cu with pressure infiltration casting. The fiber volume fractions of all but one of the remaining layers were then estimated, and the fiber volume fraction of the remaining layer was calculated based on the known overall fiber volume fraction of the specimen determined in the manner described below. This process does not yield exact values for the fiber volume fraction of each layer, however, as shown in Chapter 4, small changes in the fiber volume fraction of a single layer do not significantly affect the predicted thermal expansion of the composite when the overall fiber volume fraction of the composite is maintained. Future work may use optical techniques to obtain more precise estimates for the layer fiber volume fractions.

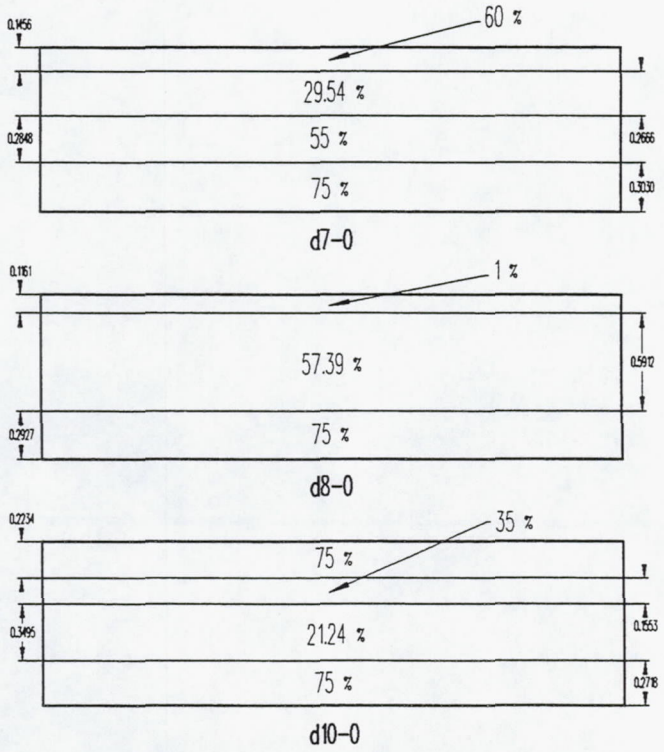

Figure 5.6: Actual specimens simulated as laminates for use with MCLAM.

The overall fiber volume fractions of the specimens are given in Table 5.1.

Specimen	Fiber Volume Fraction
d7-0	0.55
d8-0	0.56
d10-0	0.50
d1-90	0.66
d2-90	0.66

Table 5.1: Fiber volume fractions of the experimental specimens

The fiber volume fractions were calculated from the mass balance,

$$\rho_C V_C = \rho_f V_f + \rho_m \left(1 - V_f\right) \tag{5.1}$$

where ρ_C, ρ_f, and ρ_m are the densities of the composite, fiber, and matrix, respectively, and where V_C and V_f are the composite and the fiber volumes, respectively. The mass and volume of the composite can be measured, and the density of the fiber and the matrix are known, so V_f can be calculated. This is divided by the volume of the composite to yield the fiber volume fraction.

The measured thermal expansion for the Gr/Cu specimens is shown in Figure 5.7 and Figure 5.8. The cause of the oscillatory nature of the longitudinal thermal expansion curves in Figure 5.7 has not been conclusively determined, however, ignoring the oscillations, the data has been shown to be accurate (Ellis, 1994). The longitudinal specimens show reasonably good repeatability as do the transverse specimens. It should be noted that specimen d1-90 showed evidence of cracking (not shown in Figure 5.4).

MCLAM was used to predict the thermal expansion behavior of the laminates shown in Figure 5.6 which simulate the actual microstructure of the longitudinal specimens. The results are given in Figures 5.9, Figure 5.10, and Figure 5.11 for the d7-0, d8-0, and d10-0 specimens, respectively. The thermal expansion curves are plotted for stress-free temperatures of 100 °F and 1700 °F for three cases, namely: a uniform fiber distribution; the simulation of the actual specimen microstructure; and the simulation of the actual microstructure with slight fiber misalignment. The slight fiber misalignment was

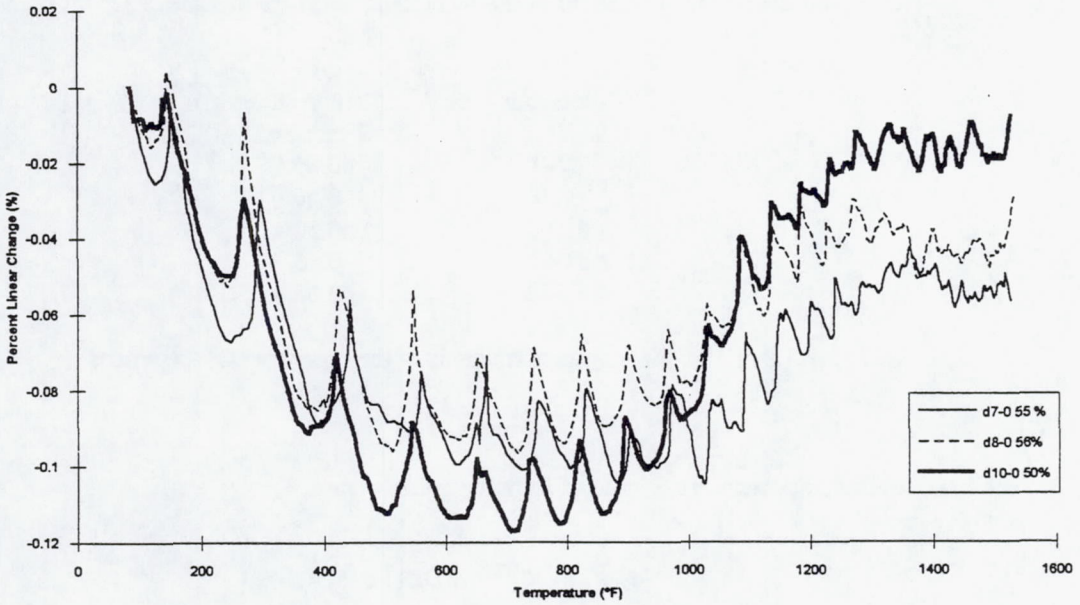

Figure 5.7: The measured longitudinal thermal expansion of P100 Gr/Cu - 0.1 Cr.

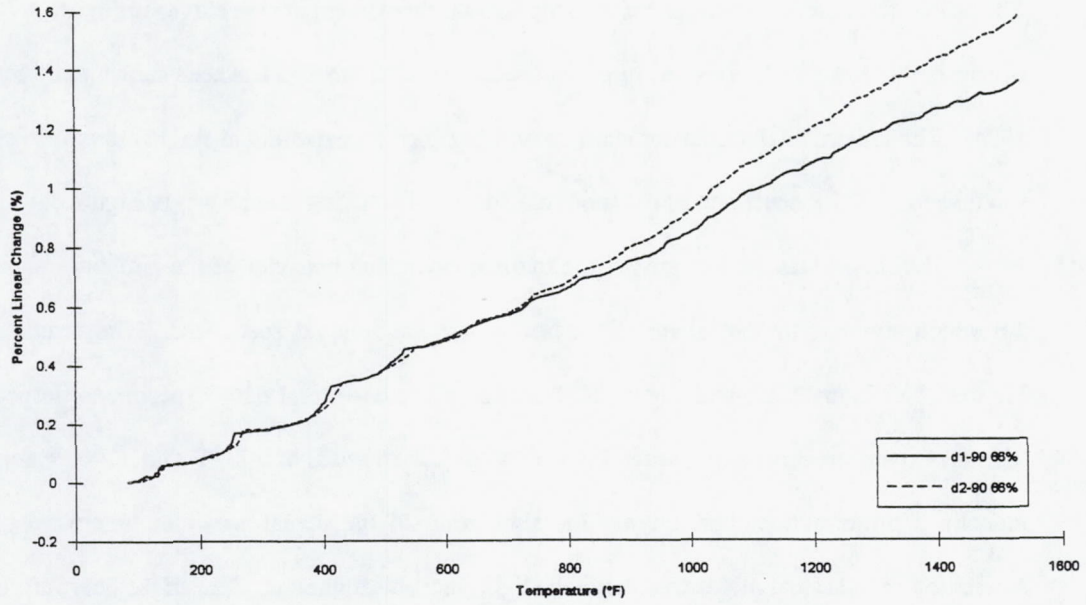

Figure 5.8: The measured transverse thermal expansion of P100 Gr/Cu - 0.1 Cr.

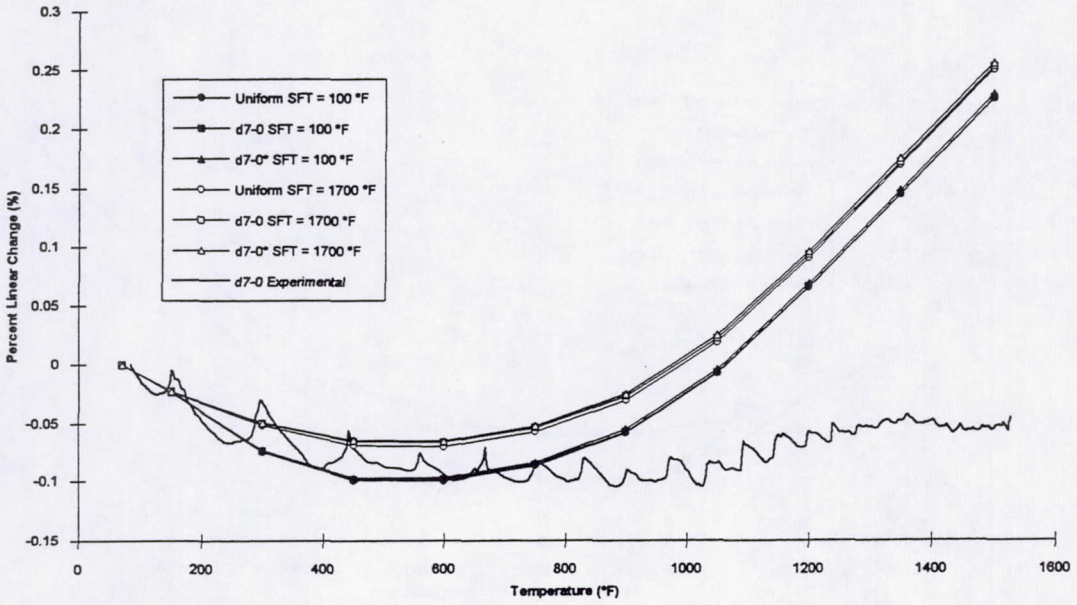

Figure 5.9: Longitudinal thermal expansion of 55 v/o P100 Gr/Cu. Uniform fiber distribution, a simulation of thermal expansion specimen d7-0, a simulation of thermal expansion specimen d7-0 with slight fiber misalignment (d7-0*), and experimental results are shown.

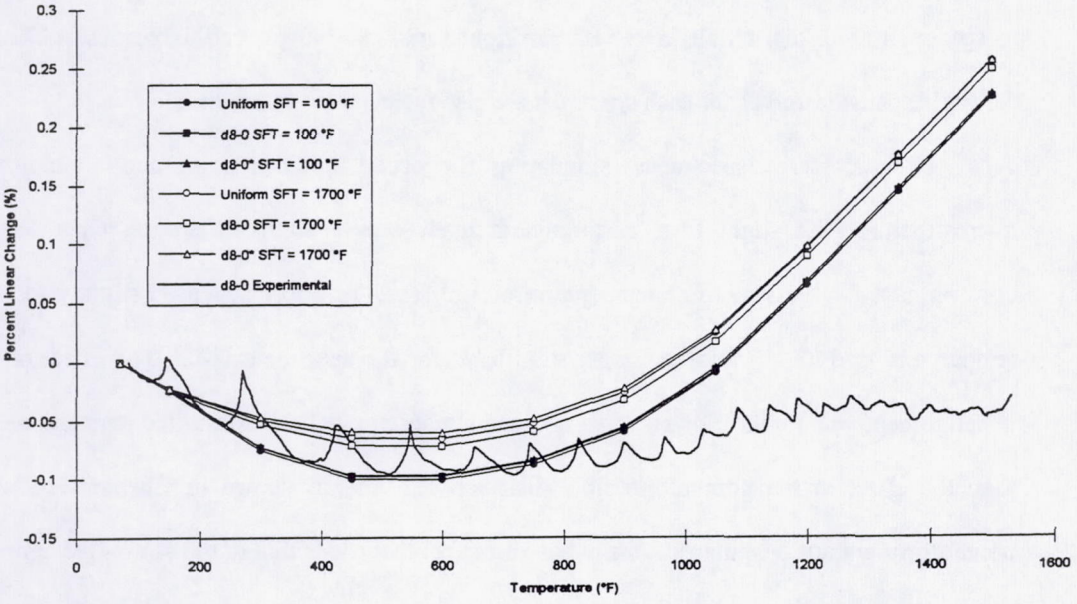

Figure 5.10: Longitudinal thermal expansion of 56 v/o P100 Gr/Cu. Uniform fiber distribution, a simulation of thermal expansion specimen d8-0, a simulation of thermal expansion specimen d8-0 with slight fiber misalignment (d8-0*), and experimental results are shown.

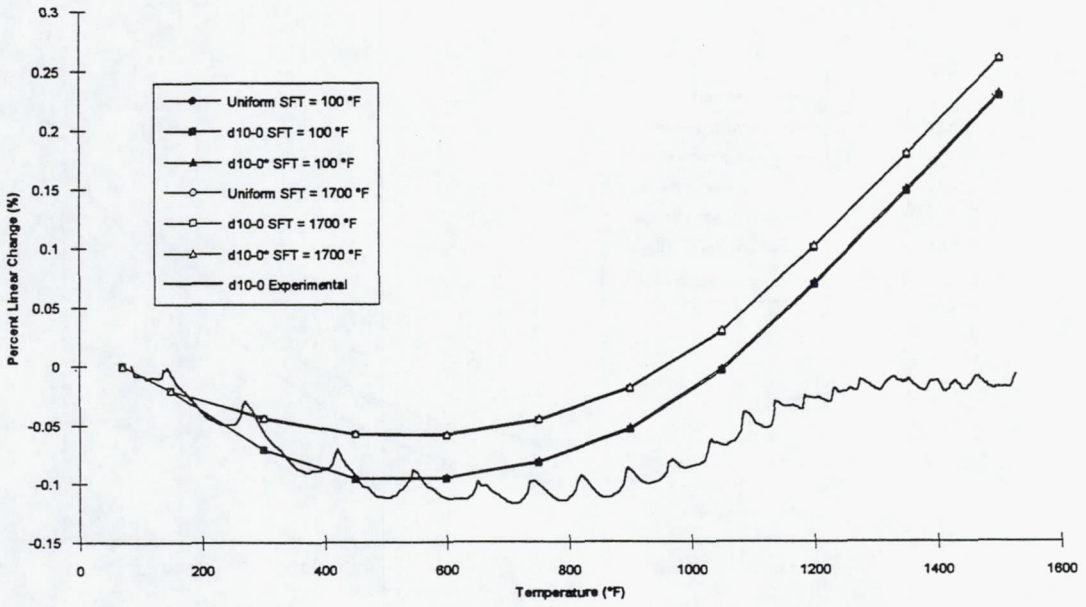

Figure 5.11: Longitudinal thermal expansion of 50 v/o P100 Gr/Cu. Uniform fiber distribution, a simulation of thermal expansion specimen d10-0, a simulation of thermal expansion specimen d10-0 with slight fiber misalignment (d10-0*), and experimental results are shown.

introduced by setting the fiber angle to 4° in the lower two layers of each laminate shown in Figure 5.6. In specimen d8-0, the middle layer was partitioned into two halves for this purpose. The experimental thermal expansion curves for each specimen are also included for comparison.

For all three specimens, simulating the actual microstructure and simulating the actual microstructure with slight fiber misalignment made only a slight difference when compared to the uniform case for the stress-free temperature of 100 °F. The effect increased slightly for the stress-free temperature of 1700 °F and was most significant for the specimen d8-0. The effect of a slight fiber misalignment was small. For all three specimens, the effect of the stress-free temperature is far greater than the effect of the nonuniform fiber distribution. As was shown in Chapter 4, fiber distribution nonuniformity must be quite extreme to have an effect that rivals that of the stress-free temperature. Thus little is gained in the attempt to accurately model the thermal expansion of Gr/Cu by simulating the specimen microstructure for the cases examined.

Since the effect of the nonuniform fiber distribution is so small, taking nonuniform fiber distribution into account does not improve the experimental/analytical correlation. Thus the effect of the fiber distribution will not be discussed further. It should be noted that CCMICRON and MCLAM both reduce to the method of cells with classical incremental plasticity for the uniform case, producing identical results. Therefore only one model must be used to generate the results for the uniform cases (MCLAM was used). Figure 5.9, Figure 5.10, and Figure 5.11 indicate that for the longitudinal thermal response the differences between the two stress-free temperatures is on the order of the oscillatory effects in the experimental results. Thus, the stress-free temperature will be ignored in the discussion of the monotonic longitudinal response, but in modeling the cyclic longitudinal response, both stress-free temperatures will be used.

The models predict the longitudinal thermal expansion quite well up to a temperature of approximately 700 °F, at which point the model predicts that the composite will expand rapidly, whereas the measured response remains quite flat. This rapid expansion is predicted because the composite longitudinal thermal response is fiber dominated. The axial CTE input data for the fiber indicates that the fiber itself expands rapidly in the longitudinal direction at higher temperatures (see Figure 4.1). The poor experimental/analytical correlation at the higher temperatures indicates that the axial CTE data for the fiber may be inaccurate for temperatures above 700 °F. If, for example, the axial fiber CTE is set to the value at 700 °F for all temperatures above 700 °F, the predicted thermal expansion shown in Figure 5.12 is obtained for a composite with uniform fiber distribution. This case is plotted for a fiber volume fraction of 0.55 and a stress-free temperature of 100 °F along with the experimental results. Obviously, CCMICRON and MCLAM produce much better predictions for this case.

The transverse thermal expansion of d1-90 and d2-90 specimens was modeled treating the specimens as uniform since the specimens show little fiber distribution nonuniformity (see Figures 5.4 and 5.5). The results are presented in Figure 5.13. The models overpredict the transverse thermal expansion substantially. The measured thermal expansion curves for the two transverse specimens are closer to the response of the fiber and the matrix. As discussed in Section 4.2, the predicted response is above the response of the fiber and matrix because of the Poisson's effect that occurs due to compressive stress in the

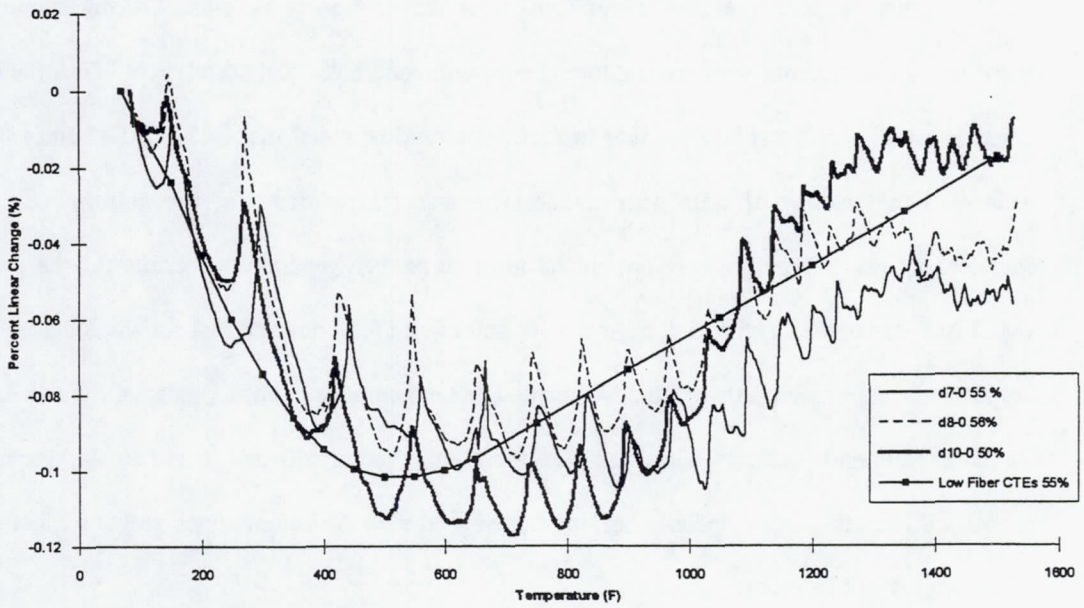

Figure 5.12: The measured longitudinal thermal expansion of P100 Gr/Cu - 0.1 Cr and the predicted thermal expansion for the case where the axial fiber CTEs are set to the value at 700 °F at every temperature above 700 °F. A stress-free temperature of 100 °F was used.

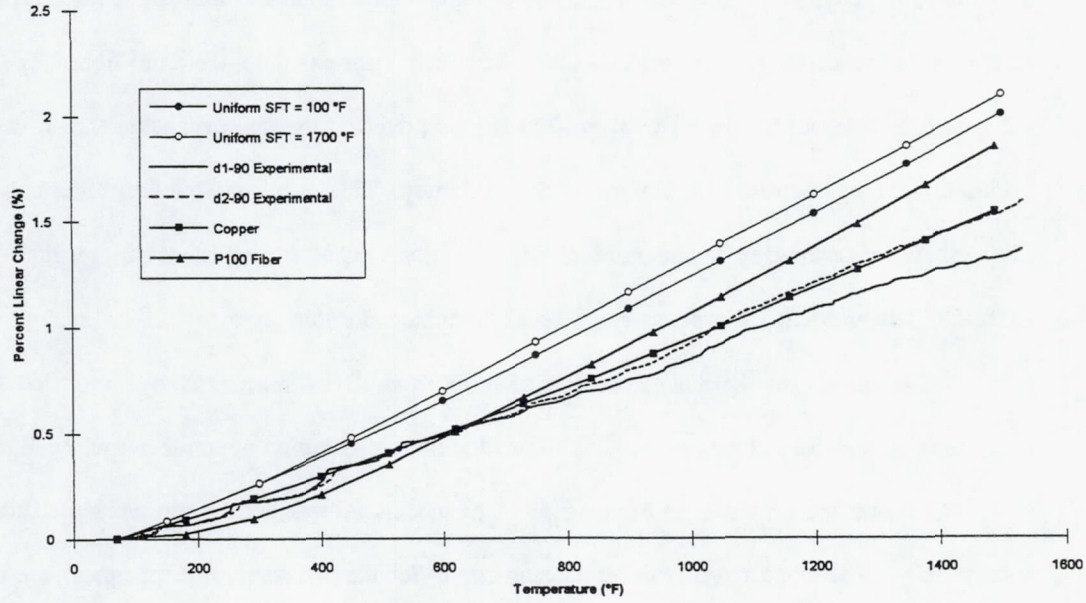

Figure 5.13: Transverse thermal expansion of 66 v/o P100 Gr/Cu. Uniform fiber distribution and experimental results are shown along with the response of the fiber and the matrix.

matrix in the longitudinal direction. The experimental results indicate that this effect is overpredicted.

To determine if the overprediction is due to stress relaxation occurring in the matrix of the actual specimen which is not taken into account by classical incremental plasticity, the model of Williams and Pindera (1994a) with Freed-Walker viscoplasticity (see Section 4.3), which allows stress relaxation in the matrix, was used. This model predicts the transverse thermal expansion of specimens d1-90 and d2-90 to be similar to the prediction of classical incremental plasticity. This is shown in Figure 5.14. Thus taking stress relaxation effects into account does not significantly improve the experimental/analytical correlation for the transverse thermal expansion response.

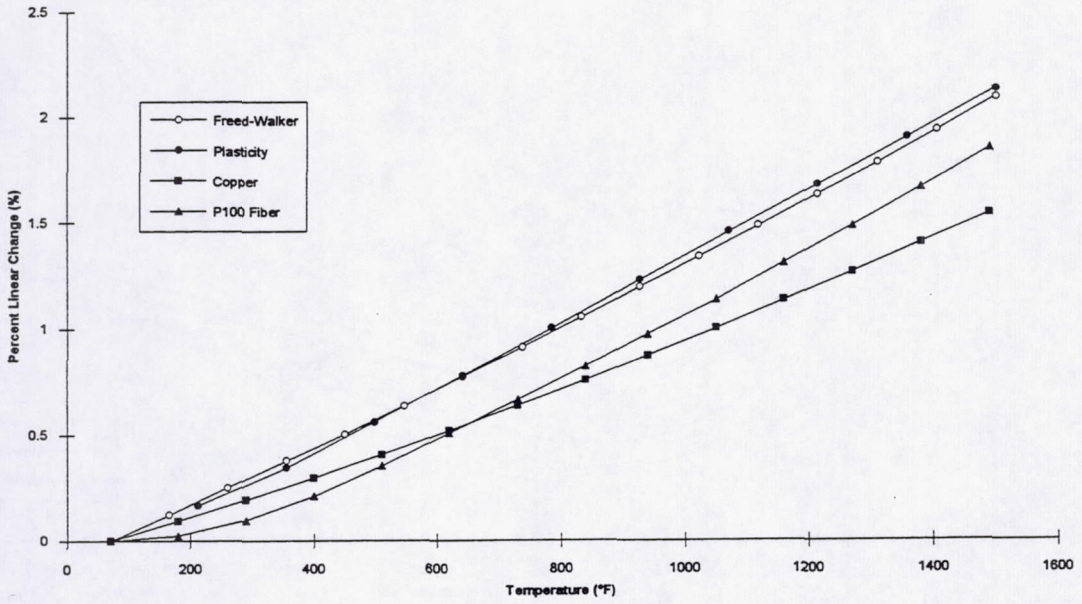

Figure 5.14: Transverse thermal expansion of 55 v/o P100 Gr/Cu. Predictions are shown using Freed-Walker viscoplasticity and classical incremental plasticity along with the response of the fiber and the matrix.

5.2 Cyclic Thermal Expansion

When a composite undergoes plastic deformation during thermal loading, the thermal expansion curve will not necessarily retrace the same path or return to the initial configuration if the thermal loading is reversed. Plastic deformation is not a reversible process. Thus when Gr/Cu is heated to a temperature beyond which plastic deformation occurs and then cooled, the thermal expansion curve forms hysteresis a loop. This can be seen in Figure 5.15. The experimental thermal expansion curve for specimen d7-0 is low during heating and high during cooling. It is desirable to have the ability to predict not only the thermal expansion during heating, but also the thermal expansion during cooling and subsequent heating-cooling cycles.

The predicted cyclic thermal expansion for a Gr/Cu composite with uniform fiber distribution and the predicted cyclic thermal expansion for a Gr/Cu composite with the nonuniform fiber distribution of Lam 1 (see Figure 4.23) are also shown in Figure 5.15. Lam 1 is included to show an upper bound of

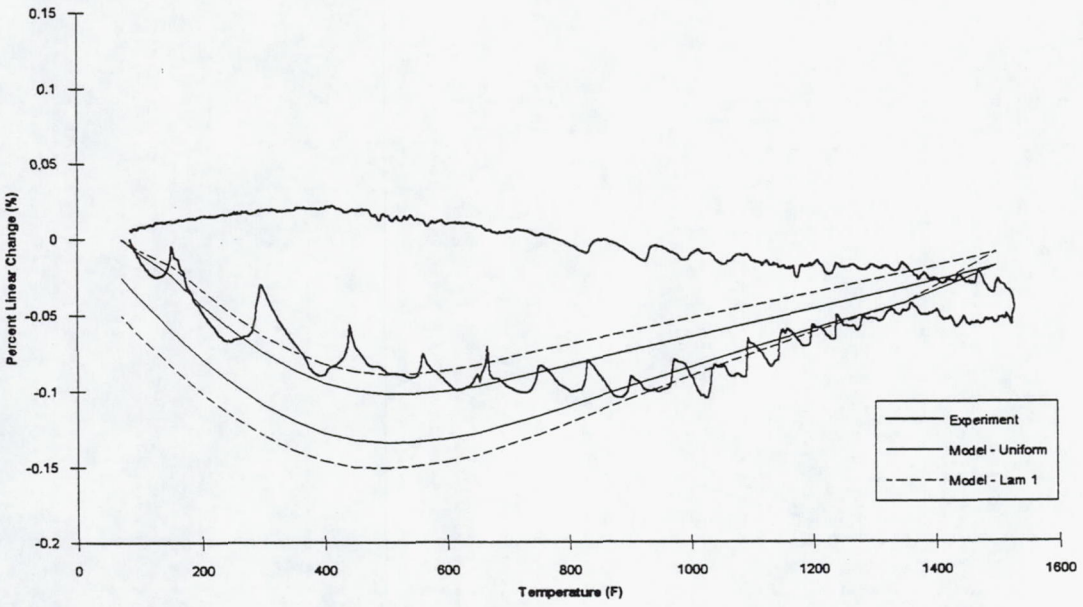

Figure 5.15: Cyclic longitudinal thermal expansion of 55 v/o P100 Gr/Cu. Experimental data for d7-0, the predicted response for the uniform case, and the predicted response of the Lam 1 configuration are shown. A stress-free temperature of 100 °F was used.

the effect that nonuniform fiber distribution has on the cyclic thermal expansion of Gr/Cu. The predicted curves were generated with MCLAM, and as discussed in Section 5.1, the axial CTE of the fiber was set equal to the value at 700 °F for every temperature above 700 °F. This was shown to more accurately model the heating thermal expansion curves for the specimens that were tested. A stress-free temperature of 100 °F was used to generate the predicted curves in Figure 5.15.

As was shown in Section 5.1, the uniform model with the altered fiber CTEs compares reasonably well with the experimental results for the heating portion of the curve. The heating curve for the Lam 1 configuration is raised slightly and thus compares more favorably with experiment at low temperature and less favorably at high temperature. In both cases, the model predicts that the cooling curve for the cycle will be lower than the heating curve of the cycle. This conflicts with the experimental data, and the predicted cooling curves for the cycle are vastly different from what is observed experimentally. The predicted cooling curve for the Lam 1 configuration is lower than that of the uniform case and is thus even further from the experimental cooling curve. Furthermore, the experimental data shows that after the thermal cycle, the specimen nearly returns to its original length while the model predicts a substantial negative change in length for both cases.

Figures 5.16 and 5.17 show the predicted longitudinal thermal expansion for three cycles for the uniform case and the Lam 1 configuration, respectively, using a stress-free temperature of 100 °F. Both cases exhibit an increasing amount of deformation at 1500 °F with each additional cycle. This "ratcheting" behavior causes the thermal expansion curve of each subsequent cycle to appear higher at the high temperatures. This sort of behavior has been observed experimentally in Gr/Cu with no chromium added to the matrix (DeVincent, 1994a). The effect was reduced significantly by adding chromium to the matrix, and thus is thought to be the result of debonding. Figures 5.16 and 5.17 indicate that cyclic ratcheting may occur in the presence of perfect bonding. Comparing the cyclic response of the uniform case and the Lam 1 configuration indicates that the ratcheting effect can be greater for composites with nonuniform fiber distribution.

Figures 5.18 - 5.20 differ from Figures 5.15 - 5.17 only in that the stress-free temperature used in the latter set of figures is 1700 °F rather than 100 °F. Figure 5.18 shows that the predicted heating

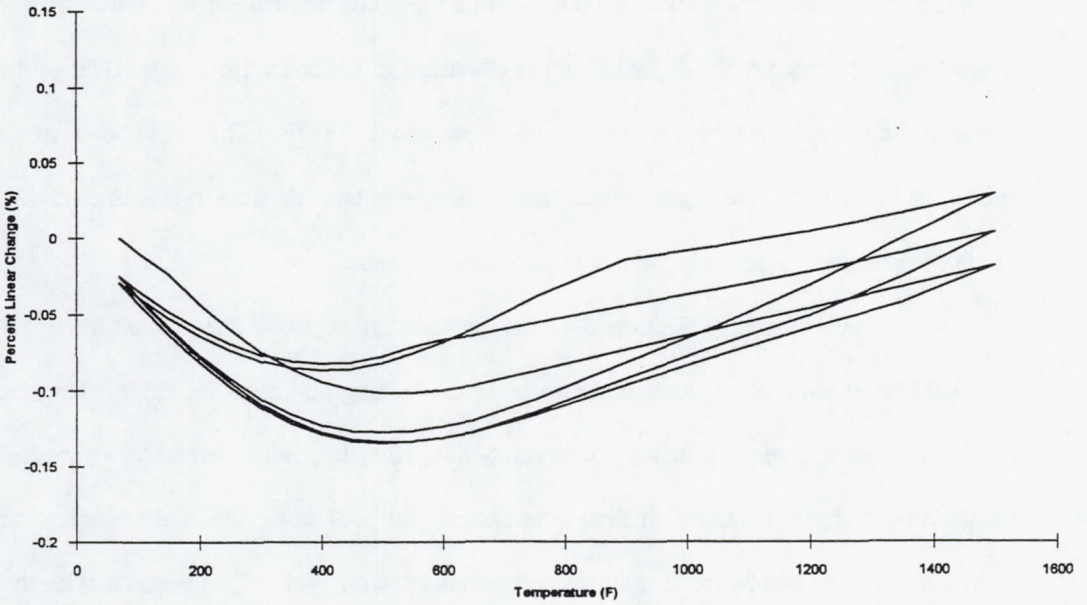

Figure 5.16: Cyclic longitudinal thermal expansion of 55 v/o P100 Gr/Cu. The predicted response for the uniform case using a stress-free temperature of 100 °F is shown.

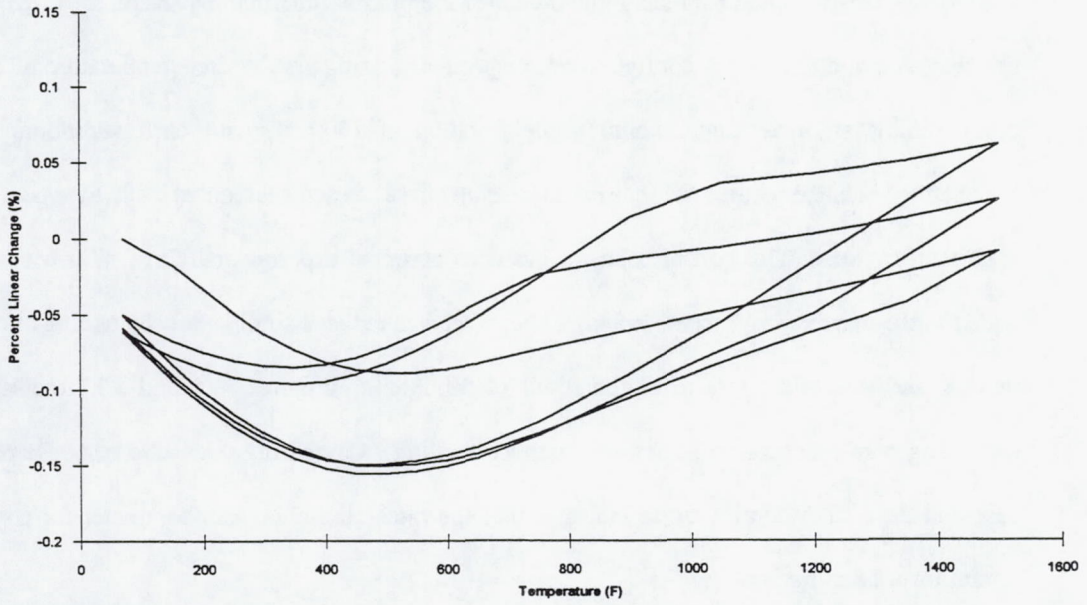

Figure 5.17: Cyclic longitudinal thermal expansion of 55 v/o P100 Gr/Cu. The predicted response for the Lam 1 configuration using a stress-free temperature of 100 °F is shown.

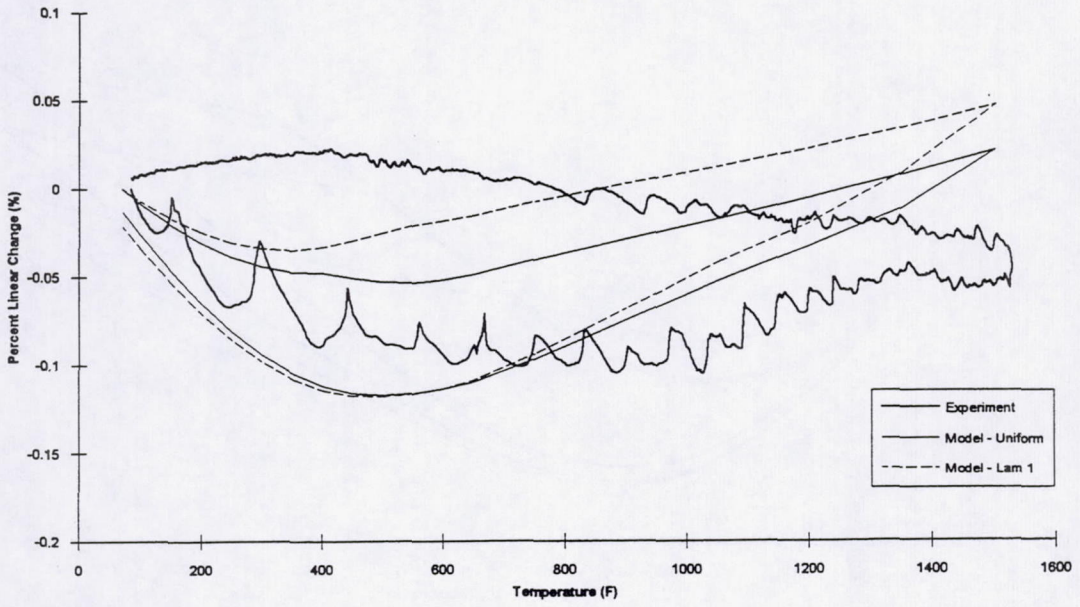

Figure 5.18: Cyclic longitudinal thermal expansion of 55 v/o P100 Gr/Cu. Experimental data for d7-0, the predicted response for the uniform case, and the predicted response of the Lam 1 configuration are shown. A stress-free temperature of 1700 °F was used.

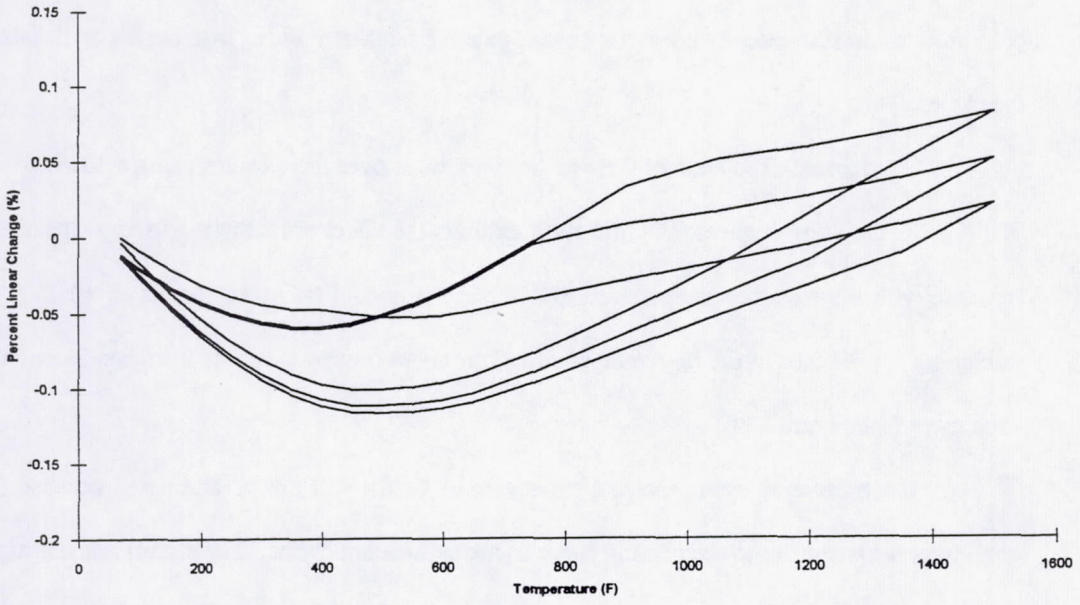

Figure 5.19: Cyclic longitudinal thermal expansion of 55 v/o P100 Gr/Cu. The predicted response for the uniform case using a stress-free temperature of 1700 °F is shown.

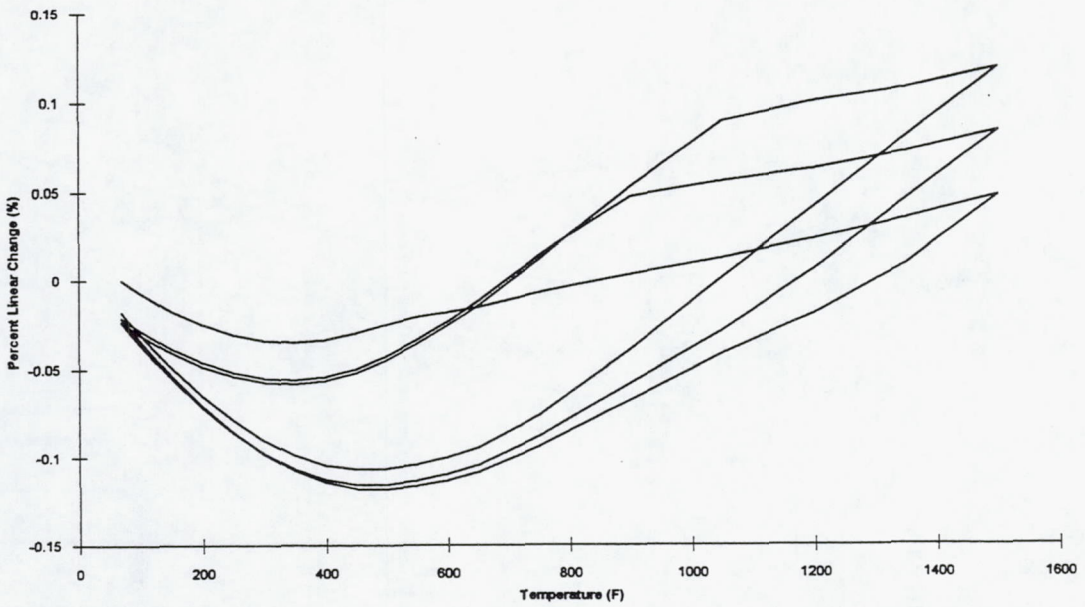

Figure 5.20: Cyclic longitudinal thermal expansion of 55 v/o P100 Gr/Cu. The predicted response for the Lam 1 configuration using a stress-free temperature of 1700 °F is shown.

portion of the thermal expansion curves for a stress-free temperature of 1700 °F does not agree with experiment as well as for a stress-free temperature of 100 °F. Also, the predicted response for the Lam 1 configuration in this case deviates to a greater extent from the uniform case during the heating portion of the cycle.

The thermal expansion of the two configurations over three cycles using a stress-free temperature of 1700 °F, shown in Figures 5.19 and 5.20, exhibits the effect of ratcheting to a greater extent than was the case with a stress-free temperature of 100 °F. It should be noted that even when a great deal of ratcheting is predicted at the high temperatures, the curve returns to nearly the same location at the end of each cycle (see Figure 5.20).

The transverse cyclic thermal expansion of Gr/Cu will not be addressed because the transverse cooling curve is similar to the heating curve as are subsequent cycles. The significant observation that can be taken from this examination of cyclic thermal expansion is that the model predicts the thermal expansion loop of Gr/Cu to have the opposite direction of the loop observed experimentally. Thus a

mechanism that is not taken into account in MCLAM must be present. Further research is warranted in this area.

6. Summary and Conclusions

Two micromechanical models were developed for characterizing the thermal expansion of Gr/Cu composites with nonuniform fiber distributions. A previously developed multiple concentric cylinder model was further extended to allow each cylinder to be modeled as a two-phase composite. This model (CCMICRON) was used to simulate the thermal expansion behavior of Gr/Cu with a radially nonuniform microstructure by assigning each concentric cylinder an independent fiber volume fraction. The second model developed (MCLAM) consisted of an extension of classical lamination theory to include inelastic behavior of the matrix phase. Since the fiber volume fraction of each lamina is user-defined in MCLAM, this model was used to examine the thermal expansion behavior of Gr/Cu with nonuniform microstructure in the through-thickness direction. Additionally, MCLAM includes a user-defined fiber orientation in each lamina which is taken into account by the lamination theory equations, thus allowing one to investigate the effect of fiber misalignment on the thermal expansion.

The features of both CCMICRON and MCLAM are quite similar. In both models, the method of cells micromechanics model is used to evaluate the effective temperature-dependent properties of the uniform regions. In addition, the inelastic constitutive theory (classical incremental plasticity theory) is applied to the matrix phase at the micro-level in both cases. Thus for uniform fiber distributions

CCMICRON and MCLAM reduce to the method of cells with classical incremental plasticity. Because of the presence of inelastic strains in the matrix, the governing set of simultaneous equations in the models are implicit and thus must be solved iteratively. The iterative solution procedure developed by Mendelson (1983) is thus used.

Incorporating plastic behavior of the matrix into the models results in a more difficult analytical solution and increased computational time. However, it was shown in Section 4.2 that the effect of matrix inelasticity on the thermal expansion of Gr/Cu is significant. Disregarding yielding and subsequent plastic flow in the matrix results in unreliable predictions.

To account for residual stresses in the composite and processing-induced yielding in the matrix, the concept of a stress-free temperature was employed during the implementation of both models. The procedure involved simulating a cool-down from an assumed stress-free temperature prior to beginning the simulation of a thermal expansion test. It was found that, like matrix plasticity, the assumed stress-free temperature has a major effect on the thermal expansion of Gr/Cu. Actual values for the stress-free temperature could not be determined. Thus 1700 °F and 100 °F were chosen as approximate upper and lower bounds on the true stress-free temperature.

In order to examine the effect of radially nonuniform fiber distribution on the thermal expansion of Gr/Cu, two extreme cases were considered using CCMICRON. The first case was a core with a low fiber volume fraction surrounded by a cylinder with the highest possible fiber volume fraction for composites reinforced with continuous cylindrical fibers. The second case was the opposite; a core with high fiber volume fraction surrounded by a cylinder with low fiber volume fraction. These cases represented an extreme because the change in fiber volume fraction was large and abrupt.

Results indicated that for the thermal expansion of Gr/Cu, radially nonuniform fiber distribution was not significant, even in the most extreme cases mentioned above. Through further investigation it was found that treating the fiber as isotropic rather than transversely isotropic by setting the transverse CTE and Young's modulus to the axial values increased the effect of the nonuniform fiber distribution considerably. Thus the thermal expansion behavior of a composite with a large transverse CTE mismatch

and a large transverse Young's modulus mismatch could be significantly affected by radially nonuniform fiber distribution.

MCLAM was used to examine the effect of fiber distribution nonuniformity in the through-thickness direction on the thermal expansion of Gr/Cu. This type of fiber distribution more closely approximates the situation in real Gr/Cu composites. Several laminate configurations were considered using MCLAM. The one that exhibited the largest effect of the fiber distribution nonuniformity was an unsymmetric two-ply laminate with one ply having high fiber volume fraction and one ply having low fiber volume fraction. Like the cases examined using MCLAM, this case represents a large and abrupt change in fiber volume fraction. In addition, since this laminate is unsymmetric, bending occurs when it is subjected to thermal loading.

Results for MCLAM indicated that when there is significant bending, as there is for the laminate described above, the effect of the nonuniform fiber distribution on the thermal expansion is significant. Reducing or eliminating the bending significantly reduces the observed effect. For the cases in which bending is induced, the effect of the nonuniform fiber distribution is of approximately the same magnitude as the effect of the choice of stress-free temperature

Slight fiber misalignment proved to have different effects on the thermal expansion depending on the stress-free temperature used. For a low stress-free temperature, the fiber misalignment had little effect on the longitudinal thermal expansion but a noticeable effect on the transverse thermal expansion. For a high stress-free temperature, the opposite was true. This was explained by examining the thermal expansion of several symmetric angle-ply composites at high and low stress-free temperatures. It was found that for a low stress-free temperature the longitudinal thermal expansion at low ply angles was less sensitive to changes in the ply angle than was the case for a high stress-free temperature. At high ply angles, the low stress-free temperature case was more sensitive to changes in the ply angle than the high stress-free temperature case. Thus, when considering slight fiber misalignment, using a low stress-free temperature causes greater sensitivity in the transverse direction (which is the same as a slight change in ply angle at a high ply angle) while using a high stress-free temperature cause greater sensitivity in the longitudinal direction.

Experimental thermal expansion data were generated for three longitudinal and two transverse specimens. The actual microstructure of the longitudinal specimens was inhomogeneous while the transverse specimens exhibited nearly uniform fiber distribution. Results generated using MCLAM indicated that the simulated microstructure of the longitudinal specimens had little effect on the predicted thermal expansion of those specimens. Adding slight fiber misalignment likewise had little effect. Oscillations in the experimental data were much greater than the effect of the nonuniform fiber distribution and even the choice of stress-free temperature.

The model with uniform fiber distribution agreed reasonably well with experiment in the longitudinal direction up to a temperature of approximately 700 °F at which point the predicted response increased rapidly while the measured response remained reasonably flat. This discrepancy called into question the reliability of the high temperature axial CTEs of the graphite fibers since at these temperatures the measured longitudinal thermal expansion of the composite was far less than that of both the fiber and the matrix. To compensate, the axial fiber CTEs were set to the value of the fiber axial CTE at 700 °F, and much better agreement was obtained. The predicted transverse thermal expansion curve for Gr/Cu was significantly higher than the experimental curve for reasons that have not been determined.

The longitudinal cyclic thermal expansion of Gr/Cu was modeled using the altered high temperature axial fiber CTEs and compared to the single cycle experimental response. While the heating portion of the predicted response was in good agreement with the experimental response, the cooling portion was incorrectly predicted. In particular, experiment shows that the direction of the cyclic thermal expansion loop is the reverse of what is predicted. Thus a mechanism that is unaccounted for in the model may be operative. This requires further investigation. Additional cycles were generated, and the predicted response exhibited "ratcheting" behavior that has been observed experimentally in Gr/Cu.

References

Aboudi, J. (1989) "Micromechanical Analysis of Composites by the Method of Cells" Applied Mechanics Reviews. Vol. 42, No. 7, p. 193-221.

Aboudi, J. (1991) Mechanics of Composite Materials A Unified Micromechanical Approach. Elsevier, New York.

Adams, D.F. and Doner, D.R. (1967a) "Transverse Normal Loading of a Unidirectional Composite" Journal of Composite Materials. Vol. 1, p. 152-164.

Adams, D.F. and Doner, D.R. (1967b) "Longitudinal Shear Loading of a Unidirectional Composite" Journal of Composite Materials. Vol. 1, p. 4-17.

Adams, D.F. (1970) "Inelastic Analysis of a Unidirectional Composite Subjected to Transverse Normal Loading" Journal of Composite Materials. Vol. 4, p. 310-328.

Ashby, M.F. and Jones, D.R.H. (1980) Engineering Materials 1 An Introduction to Their Properties and Applications. Pergamon Press, New York.

Bigelow, C.A. (1992) "The Effects of Uneven Fiber Spacing on Thermal Residual Stresses in a Unidirectional SCS-6/Ti-15-3 Laminate" Journal of Composites Technology and Research. Vol. 14, No. 4, p. 211-220.

Böhm, H.J., Rammerstorfer, F.G., and Weissenbek, E. (1993) "Some Simple Models for Micromechanical Investigations of Fiber Arrangement Effects" Computational Materials Science. Vol. 1, p. 177-194.

Brockenbrough, J.R. and Suresh, S. (1990) "Plastic Deformation of Continuous Fiber-Reinforced Metal-Matrix Composites: Effects of Fiber Shape and Distribution" Scripta Metallurgica et Materialia. Vol. 24, p. 325-330.

Brockenbrough, J.R., Suresh, S., and Wienecke, H.A. (1991) "Deformation of Metal-Matrix Composites with Continuous Fibers: Geometrical Effects of Fiber Distribution and Shape" Acta Metallurgica et Materialia. Vol. 39, No. 5, p. 735-752.

Chang, C.S. and Conway, H.D. (1968) "Bond Stresses in Fiber Reinforced Composites Subjected to Uniform Tension" Journal of Composite Materials. Vol. 2, No. 2, p. 168-185.

Christman, T., Needleman, A., and Suresh, S. (1989) "An Experimental and Numerical Study of Deformation in Metal-Ceramic Composites" Acta Metallurgica et Materialia. Vol. 37, No. 11, p. 3029-3050.

DeVincent, S.M. (1994a) "Interfacial Effects on the Thermal and Mechanical Properties of Graphite/Copper Composites" Case Western Reserve University, PhD. Dissertation.

DeVincent, S.M. (1994b) Personal Communication.

Dragone, T.L. and Nix, W.D. (1990) "Geometric Factors Affecting the Internal Stress Distribution and High Temperature Creep Rate of Discontinuous Fiber Reinforced Metals" Acta Metallurgica et Materialia. Vol. 38, No. 10, p. 1941-1953.

Ellis, D.L. (1992) "Properties of Graphite Fiber Reinforced Copper Matrix Composites for Space Power Applications" NASA Contractor Report 191026.

Ellis, D.L. (1994) Personal Communication.

Freed, A.D., Walker, K.P., and Verrilli, M.J. (1993) "Extending the Theory of Creep to Viscoplasticity" Invited paper for the 1993 ASME Pressure Vessel and Piping Conference.

Hashin, Z. and Rosen, B.W. (1964) "The Elastic Moduli of Fiber-Reinforced Materials" Journal of Applied Mechanics. Vol. 31E, p. 223.

Hiemstra, D.L. and Sottos, N.R. (1993) "Thermally Induced Interfacial Microcracking in Polymer Matrix Composites" Journal of Composite Materials. Vol. 27, No. 10, p. 1030-1051.

Jones, R.M. (1975) Mechanics of Composite Materials. Hemisphere Publishing Corp., New York.

Karbhari, V.M. and Wilkins, D.J. (1991) "Constituent Scale and Property Effects on Fibre-Matrix Debonding and Pull-Out" Journal of Materials Science. Vol. 26, p. 5888-5898.

Komenda, J. and Henderson, P.J. (1993) "Quantification of Fibre Distribution in a Metal Matrix Composite and Its Effect on Creep Rupture Properties" Scripta Metallurgica et Materialia. Vol. 28, p. 553-558.

MacKay, R. (1990) "Effect of Fiber Spacing on Interfacial Damage in a Metal Matrix Composite" Scripta Metallurgica et Materialia. Vol. 24, p. 167-172.

Martin, A.F. and Leissa, A.W. (1989) "Application of the Ritz Method to Plane Elasticity Problems for Composite Sheets with Variable Fiber Spacing" International Journal for Numerical Methods in Engineering. Vol. 28, p. 1813-1825.

McHugh, P.E., Asaro, R.J., and Shih, C.F. (1993) "Computational Modeling of Metal Matrix Composite Materials-I. Isothermal Deformation Patterns in Ideal Microstructures" Acta Metallurgica et Materialia. Vol. 41, No. 5, p. 1461-1476.

Mendelson, A. (1983) Plasticity: Theory and Applications. Robert E. Krieger Publishing Co., Makabar, FL.

Mueller, A.C. (1994) "A Finite Element Method for Microstructural Analysis" Composites Engineering. Vol. 4, No. 3, p. 361-376.

Nakamura, T. and Suresh, S. (1993) "Effects of Thermal Residual Stresses and Fiber Packing on Deformation of Metal Matrix Composites" Acta Metallurgica et Materialia. Vol. 41, No. 6, p. 1665-1681.

NASA Lewis Research Center (1992), Unpublished Data.

Ochiai, S. and Osamura, K. (1989a) "Stress Disturbance Due to Broken Fibres in Metal Matrix Composites with Non-Uniform Fibre Spacing" Journal of Materials Science. Vol. 24, p. 3865-3872.

Ochiai, S., and Osamura, K. (1989b) "Tensile Strength of Fiber Reinforced Metal Matrix Composites with Non-Uniform Fibre Spacing" Journal of Materials Science. Vol. 24, p. 3536-3540.

Pagano, N.J., and Brown, H.W. III (1993) "The Full-Cell Cracking Mode in Unidirectional Brittle-Matrix Composites" Composites. Vol. 24, No. 2, p. 63-83.

Pandey, M.D. and Sherbourne, A.N. (1993) "Influence of the Prebuckling Stress Field on The Critical Loads of Inhomogeneous Composite Laminates" Composite Structures. Vol. 25, No. 1-4, p. 363-369.

Pickett, G. (1968) "Elastic Moduli of Fiber Reinforced Plastic Composites" Fundamentals Aspects of Fiber Reinforced Plastic Composites. Schwartz, R.T. and Schwartz, H.S. eds., New York: Interscience Publishing.

Pindera, M-J. and Freed, A.D. (1992) "The Effect of Matrix Microstructure on the Evolution of Residual Stresses in Titanium Aluminide Composites" ASME Constitutive Behavior of High-Temperature Composites. Vol. 40, p. 37- 52.

Pindera, M-J., Freed, A.D., and Arnold, S.M. (1992) "Effects of Fiber and Interfacial Layer Architectures on the Thermoplastic Response of Metal Matrix Composites" NASA Technical Memorandum 105802.

Pindera, M-J., Freed, A.D., and Arnold, S.M. (1993) "Effects of Fiber and Interfacial Layer Morphologies on the Thermoplastic Response of Metal Matrix Composites" International Journal of Solids Structures. Vol. 30, No. 9, p. 1213-1234.

Raghava, R.S., (1988) Polymer Composites. Vol. 9, No. 1, p. 1.

Rocketdyne Materials Properties Manual (1987).

Siegmund, T., Weissenbek, E., Fischer, F.D., and Rammerstorfer, F.G. (1992) "Micromechanical Consideration of Topological Aspects Regarding Thermocyclic Behaviour" The Processing, Properties and Applications of Metallic and Ceramic Materials. Vol. 2, Conference Proc., Loretto, M.H. and Beevers, C.J. eds.

Shiau, L.C. and Lee, G.C. (1993) "Stress-Concentration Around Holes in Composite Laminates with Variable Fiber Spacing" Composite Structures. Vol. 24, No. 2, p. 107-115.

Tvergaard, V. (1990) "Analysis of Tensile Properties for a Whisker-Reinforced Metal-Matrix Composite" Acta Metallurgica et Materialia. Vol. 38, No. 2, p. 185-194.

Upadhya, K. (1992) "Ceramics and Composites for Rocket Engines and Space Structures" Journal of Mechanics. May, 1992.

Volk, D. *et. al.* (1991) "Material Behavior and Structural Applications of Glass Matrix Composites" Presented at: 15th Annual Conference on Composites, Materials and Structures, Cocoa Beach, FL.

Weissenbek, E., Böhm, H.J., and Rammerstorfer, F.G. (1993) "Microgeometrical Effects on the Elastoplastic Behavior of Particle Reinforced MMCs" Metal Matrix Composites. Proc. Ninth International Conference on Composite Materials, Miravete, Antonio ed.

Weissenbek, E. and Rammerstorfer, F.G. (1993) "Influence of the Fiber Arrangement on the Mechanical Behavior and Thermo-Mechanical Behavior of Short Fiber Reinforced MMCs" Acta Metallurgica et Materialia. Vol. 41, No. 10, p. 2833-2843.

Williams, T.O. and Pindera, M-J. (1994a), Personal Communication.

Williams, T. O. and Pindera, M-J. (1994b), "Multiple Concentric Cylinder Model (MCCM) User's Guide" NASA CR 195299, NASA-Lewis Research Center, Cleveland, OH.

Wisnom, M.R. (1990) "Factors Affecting the Transverse Tensile Strength of Unidirectional Continuous Silicon Carbide Fibre Reinforced 6061 Aluminum" Journal of Composite Materials. Vol. 24, p. 707-726.

Zhenhai, X., Zhiying, M., and Yaohe, Z. (1991) "Effect of Fiber Distribution on Infiltration Processing Fracture Behaviour of Carbon Fibre-Reinforced Aluminum Composites" Zeitschrift fur Metallkunde. Vol. 8, No. 10, p. 766-768.

Appendix A: Multiple Concentric Cylinder Model Equations

Transversely Isotropic Elastic Layers

$$k_{11} = \frac{(C_{\theta r} + C_{rr})r_{k-1} - (C_{\theta r} - C_{rr})\dfrac{r_k^2}{r_{k-1}}}{r_k^2 - r_{k-1}^2}$$

$$k_{12} = \frac{-2C_{rr}r_k}{r_k^2 - r_{k-1}^2}$$

$$k_{21} = \frac{-2C_{rr}r_{k-1}}{r_k^2 - r_{k-1}^2}$$

$$k_{22} = \frac{(C_{\theta r} + C_{rr})r_k - (C_{\theta r} - C_{rr})\dfrac{r_{k-1}^2}{r_k}}{r_k^2 - r_{k-1}^2}$$

$$k_{13} = -C_{x\theta}$$

$$k_{23} = C_{x\theta}$$

$$f_1 = C_{x\theta}\alpha_{xx} + (C_{\theta r} + C_{rr})\alpha_{rr}$$

$$f_2 = -\left[C_{x\theta}\alpha_{xx} + (C_{\theta r} + C_{rr})\alpha_{rr}\right]$$

$$\phi_{11} = -2\pi C_{x\theta}r_{k-1}$$

$$\phi_{22} = 2\pi C_{x\theta}r_k$$

$$\psi = \pi C_{xx}(r_k^2 - r_{k-1}^2)$$

$$\Omega = -\pi(C_{xx}\alpha_{xx} + 2C_{x\theta}\alpha_{rr})(r_k^2 - r_{k-1}^2)$$

Transversely Isotropic Inelastic Layers (elastic contributions same as above)

$$g_1 = \frac{2C_{\theta\theta}r_k G_k^+}{r_k^2 - r_{k-1}^2} - \overline{G}_k^-$$

$$g_2 = -\frac{\left[(C_{\theta r} + C_{rr})r_k - (C_{\theta r} - C_{rr})\dfrac{r_{k-1}^2}{r_k}\right]G_k^+}{r_k^2 - r_{k-1}^2} + \overline{G}_k^+$$

where,

$$G(r)=\frac{1}{2r}\int_{r_{k-1}}^{r}\sum_{i=x,\theta,r}\frac{(C_{ri}+C_{\theta i})}{C_{rr}}\varepsilon_{ii}^{in}r'dr'+\frac{r}{2}\int_{r_{k-1}}^{r}\sum_{i=x,\theta,r}\frac{(C_{ri}-C_{\theta i})}{C_{rr}}\varepsilon_{ii}^{in}\frac{dr'}{r'}+$$
$$\frac{1}{2}\sum_{i=x,\theta,r}\frac{C_{ri}}{C_{rr}}\varepsilon_{ii}^{in}(r_{k-1})r\left(\frac{r_{k-1}^2}{r^2}-1\right)$$

$$\overline{G}(r)=\frac{(C_{\theta r}-C_{\theta\theta})}{2r^2}\int_{r_{k-1}}^{r}\sum_{i=x,\theta,r}\frac{(C_{ri}+C_{\theta i})}{C_{rr}}\varepsilon_{ii}^{in}r'dr'+\frac{(C_{ri}+C_{\theta\theta})}{2}\int_{r_{k-1}}^{r}\sum_{i=x,\theta,r}\frac{(C_{ri}-C_{\theta i})}{C_{rr}}\varepsilon_{ii}^{in}\frac{dr'}{r'}+$$
$$\frac{1}{2}\sum_{i=x,\theta,r}\frac{C_{ri}}{C_{rr}}\varepsilon_{ii}^{in}(r_{k-1})\left[C_{\theta r}\left(\frac{r_{k-1}^2}{r^2}-1\right)-C_{rr}\left(\frac{r_{k-1}^2}{r^2}+1\right)\right]$$

$$\Pi=2\pi\int_{r_{k-1}}^{r_k}\sum_{i=x,\theta,r}C_{xi}\varepsilon_{ii}^{in}r'dr'$$

Orthotropic Elastic Layers

$$k_{11}=\frac{(C_{\theta r}+\lambda C_{rr})r_{k-1}^{2\lambda-1}-(C_{\theta r}-\lambda C_{rr})\dfrac{r_k^{2\lambda}}{r_{k-1}}}{r_k^{2\lambda}-r_{k-1}^{2\lambda}}$$

$$k_{12}=\frac{-2\lambda C_{rr}r_{k-1}^{\lambda-1}r_k^{\lambda}}{r_k^{2\lambda}-r_{k-1}^{2\lambda}}$$

$$k_{21}=\frac{-2\lambda C_{rr}r_{k-1}^{\lambda}r_k^{\lambda-1}}{r_k^{2\lambda}-r_{k-1}^{2\lambda}}$$

$$k_{22}=\frac{(C_{\theta r}+\lambda C_{rr})r_k^{2\lambda-1}-(C_{\theta r}-\lambda C_{rr})\dfrac{r_{k-1}^{2\lambda}}{r_k}}{r_k^{2\lambda}-r_{k-1}^{2\lambda}}$$

$$k_{13}=-\left[C_{xr}+(C_{\theta r}+C_{rr})H_1+\frac{(C_{\theta r}+\lambda C_{rr})(r_{k-1}^{2\lambda}-r_{k-1}^{\lambda-1}r_k^{\lambda+1})H_1}{r_k^{2\lambda}-r_{k-1}^{2\lambda}}+\frac{(C_{\theta r}-\lambda C_{rr})(r_{k-1}^{\lambda-1}r_k^{\lambda+1}-r_k^{2\lambda})H_1}{r_k^{2\lambda}-r_{k-1}^{2\lambda}}\right]$$

$$k_{23} = C_{xr} + (C_{\theta r} + C_{rr})H_1 + \frac{(C_{\theta r} + \lambda C_{rr})(r_{k-1}^{\lambda+1} r_k^{\lambda-1} - r_k^{2\lambda})H_1}{r_k^{2\lambda} - r_{k-1}^{2\lambda}} + \frac{(C_{\theta r} - \lambda C_{rr})(r_{k-1}^{2\lambda} - r_{k-1}^{\lambda+1} r_k^{\lambda-1})H_1}{r_k^{2\lambda} - r_{k-1}^{2\lambda}}$$

$$f_1 = C_{xr}\alpha_{xx} + C_{r\theta}\alpha_{\theta\theta} + C_{rr}\alpha_{rr} - (C_{\theta r} + C_{rr})H_2 - \frac{(C_{\theta r} + \lambda C_{rr})(r_{k-1}^{2\lambda} - r_{k-1}^{\lambda-1} r_k^{\lambda+1})H_2}{r_k^{2\lambda} - r_{k-1}^{2\lambda}} - \frac{(C_{\theta r} - \lambda C_{rr})(r_{k-1}^{\lambda-1} r_k^{\lambda+1} - r_k^{2\lambda})H_2}{r_k^{2\lambda} - r_{k-1}^{2\lambda}}$$

$$f_2 = -C_{xr}\alpha_{xx} - C_{r\theta}\alpha_{\theta\theta} - C_{rr}\alpha_{rr} - (C_{\theta r} + C_{rr})H_2 + \frac{(C_{\theta r} + \lambda C_{rr})(r_{k-1}^{\lambda+1} r_k^{\lambda-1} - r_k^{2\lambda})H_2}{r_k^{2\lambda} - r_{k-1}^{2\lambda}} + \frac{(C_{\theta r} - \lambda C_{rr})(r_{k-1}^{2\lambda} - r_{k-1}^{\lambda+1} r_k^{\lambda-1})H_2}{r_k^{2\lambda} - r_{k-1}^{2\lambda}}$$

$$\phi_{11} = \frac{2\pi}{r_k^{2\lambda} - r_{k-1}^{2\lambda}}\left[(C_{x\theta} - \lambda C_{xr})r_k^{2\lambda} r_{k-1}^{\lambda} \frac{(r_k^{1-\lambda} - r_{k-1}^{1-\lambda})}{1-\lambda} - (C_{x\theta} + \lambda C_{rr})r_{k-1}^{\lambda} \frac{(r_k^{1+\lambda} - r_{k-1}^{1+\lambda})}{1+\lambda}\right]$$

$$\phi_{22} = \frac{2\pi}{r_k^{2\lambda} - r_{k-1}^{2\lambda}}\left[(C_{x\theta} + \lambda C_{xr})r_k^{\lambda} \frac{(r_k^{\lambda+1} - r_{k-1}^{\lambda+1})}{1+\lambda} - (C_{x\theta} - \lambda C_{rr})r_{k-1}^{2\lambda} r_k^{\lambda} \frac{(r_k^{1-\lambda} - r_{k-1}^{1-\lambda})}{1-\lambda}\right]$$

$$\psi = \frac{2\pi H_1}{r_k^{2\lambda} - r_{k-1}^{2\lambda}}\left[(C_{x\theta} + \lambda C_{xr})(r_{k-1}^{\lambda+1} - r_k^{\lambda+1}) \frac{(r_k^{\lambda+1} - r_{k-1}^{\lambda+1})}{1+\lambda} + (C_{x\theta} - \lambda C_{xr}) \frac{(r_k r_{k-1}^{\lambda} - r_{k-1} r_k^{\lambda})^2}{1-\lambda}\right] + \pi\left[(C_{x\theta} + C_{xr})H_1\right](r_k^2 - r_{k-1}^2)$$

$$\Omega = \frac{2\pi H_2}{r_k^{2\lambda} - r_{k-1}^{2\lambda}}\left[(C_{x\theta} + \lambda C_{xr})(r_{k-1}^{\lambda+1} - r_k^{\lambda+1}) \frac{(r_k^{\lambda+1} - r_{k-1}^{\lambda+1})}{1+\lambda} + (C_{x\theta} - \lambda C_{xr}) \frac{(r_k r_{k-1}^{\lambda} - r_{k-1} r_k^{\lambda})^2}{1-\lambda}\right] + \pi\left[(C_{x\theta} + C_{xr})H_2 - \sum_{i=x,\theta,r} C_{xi}\alpha_{ii}\right](r_k^2 - r_{k-1}^2)$$

where $H_1 = \dfrac{C_{\theta x} - C_{rx}}{C_{rr} - C_{\theta\theta}}$ and $H_2 = \left(\dfrac{C_{ri} - C_{\theta i}}{C_{rr} - C_{\theta\theta}}\right)\alpha_{ii}$

Appendix B: Lamination Theory Equations

Reduced Stiffness Equations:

$$Q_{11}^k = \frac{E_1^k}{1 - \nu_{12}^k \, \nu_{21}^k}$$

$$Q_{22}^k = \frac{\nu_{21}^k \, E_1^k}{1 - \nu_{12}^k \, \nu_{21}^k}$$

$$Q_{12}^k = \frac{E_2^k}{1 - \nu_{12}^k \, \nu_{21}^k}$$

$$Q_{66}^k = G_{12}^k$$

Vector Rotation Equations:

$$\begin{bmatrix} \sigma_1 \\ \sigma_2 \\ \tau_{12} \end{bmatrix} = [T] \begin{bmatrix} \sigma_x \\ \sigma_y \\ \tau_{xy} \end{bmatrix}$$

$$\begin{bmatrix} \varepsilon_1^\xi \\ \varepsilon_2^\xi \\ \dfrac{\gamma_{12}^\xi}{2} \end{bmatrix} = [T] \begin{bmatrix} \varepsilon_x^\xi \\ \varepsilon_y^\xi \\ \dfrac{\gamma_{xy}^\xi}{2} \end{bmatrix} \qquad \text{where } \xi = T,\ p,\ total$$

$$[T] = \begin{bmatrix} \cos^2\theta & \sin^2\theta & 2\sin\theta\cos\theta \\ \sin^2\theta & \cos^2\theta & -2\sin\theta\cos\theta \\ -\sin\theta\cos\theta & \sin\theta\cos\theta & \cos^2\theta - \sin^2\theta \end{bmatrix}$$

Reduced Stiffness Rotation Equations:

$$\overline{Q}_{11}^k = Q_{11}^k \cos^4\theta + 2\left(Q_{12}^k + 2Q_{66}^k\right)\sin^2\theta\cos^2\theta + Q_{22}^k \sin^4\theta$$

$$\overline{Q}_{12}^k = \left(Q_{11}^k + Q_{22}^k - 4Q_{66}^k\right)\sin^2\theta\cos^2\theta + Q_{12}^k\left(\sin^4\theta + \cos^4\theta\right)$$

$$\overline{Q}_{22}^{k} = Q_{11}^{k}\sin^4\theta + 2\left(Q_{12}^{k} + 2Q_{66}^{k}\right)\sin^2\theta\cos^2\theta + Q_{22}^{k}\cos^4\theta$$

$$\overline{Q}_{16}^{k} = \left(Q_{11}^{k} - Q_{22}^{k} - 2Q_{66}^{k}\right)\sin\theta\cos^3\theta + \left(Q_{12}^{k} - Q_{22}^{k} + 2Q_{66}^{k}\right)\sin^3\theta\cos\theta$$

$$\overline{Q}_{26}^{k} = \left(Q_{11}^{k} - Q_{22}^{k} - 2Q_{66}^{k}\right)\sin^3\theta\cos\theta + \left(Q_{12}^{k} - Q_{22}^{k} + 2Q_{66}^{k}\right)\sin\theta\cos^3\theta$$

$$\overline{Q}_{66}^{k} = \left(Q_{11}^{k} + Q_{22}^{k} - 2Q_{66}^{k} - 2Q_{66}^{k}\right)\sin^2\theta\cos^2\theta + Q_{66}^{k}\left(\sin^4\theta + \cos^4\theta\right)$$

Appendix C: Method of Cells Equations

$$A_1 = C_{22}^m\left(1+\frac{h_2}{h_1}\right) \qquad A_2 = C_{23}^m\frac{l_1}{l_2} \qquad A_3 = C_{23}^m$$

$$A_4 = C_{22}^f + C_{22}^m\frac{h_1}{h_2} \qquad A_5 = C_{23}^f \qquad A_6 = C_{23}^m\frac{l_2}{l_1}$$

$$A_7 = C_{23}^f \qquad A_8 = C_{23}^m\frac{h_2}{h_1} \qquad A_9 = C_{22}^f + C_{22}^m\frac{l_1}{l_2}$$

$$A_{10} = C_{23}^m\frac{h_1}{h_2} \qquad A_{11} = C_{23}^m \qquad A_{12} = C_{22}^m\left(1+\frac{l_2}{l_1}\right)$$

$$J_1 = C_{22}^m\frac{h}{h_1}\bar{\varepsilon}_{22} + C_{23}^m\frac{l}{l_2}\bar{\varepsilon}_{33} - \left(C_{11}^m - C_{12}^m\right)\left(\varepsilon_{22}^{p\,(12)} - \varepsilon_{22}^{p\,(22)}\right)$$

$$J_2 = \left(C_{12}^m - C_{12}^f\right)\bar{\varepsilon}_{11} + C_{22}^m\frac{h}{h_2}\bar{\varepsilon}_{22} + C_{23}^m\frac{l}{l_1}\bar{\varepsilon}_{33} - \left(F_m^T - F_f^T\right)\Delta T - \left(C_{11}^m - C_{12}^m\right)\varepsilon_{22}^{p\,(21)} + \left(C_{11}^f - C_{12}^f\right)\varepsilon_{22}^{p\,(11)}$$

$$J_3 = \left(C_{12}^m - C_{12}^f\right)\bar{\varepsilon}_{11} + C_{23}^m\frac{h}{h_1}\bar{\varepsilon}_{22} + C_{22}^m\frac{l}{l_2}\bar{\varepsilon}_{33} - \left(F_m^T - F_f^T\right)\Delta T - \left(C_{11}^m - C_{12}^m\right)\varepsilon_{33}^{p\,(12)} + \left(C_{11}^f - C_{11}^m\right)\varepsilon_{33}^{p\,(11)}$$

$$J_4 = C_{23}^m\frac{h}{h_2}\bar{\varepsilon}_{22} + C_{22}^m\frac{l}{l_1}\bar{\varepsilon}_{33} - \left(C_{11}^m - C_{12}^m\right)\left(\varepsilon_{33}^{p\,(21)} - \varepsilon_{33}^{p\,(22)}\right)$$

where $F_i^T = C_{12}^i\alpha_1^i + \left(C_{22}^i + C_{23}^i\right)\alpha_2^i \qquad i = f, m$

$$DT_1 = -A_5A_8A_{12} - A_6A_9A_{11} \qquad DT_2 = A_2A_8A_{12} + A_3A_9A_{11} - A_1A_9A_{12}$$

$$DT_3 = A_1A_5A_{12} + A_2A_6A_{11} - A_3A_5A_{11} \qquad DT_4 = A_1A_6A_9 + A_3A_5A_8 - A_2A_6A_8$$

$$DT_5 = A_6A_9A_{10} + A_5A_7A_{12} - A_4A_9A_{12} \qquad DT_6 = -A_2A_7A_{12} - A_3A_9A_{10}$$

$$DT_7 = A_3A_5A_{10} + A_2A_4A_{12} - A_2A_6A_{10} \qquad DT_8 = A_2A_6A_7 + A_3A_4A_9 - A_3A_5A_7$$

$$DT_9 = A_4A_8A_{12} + A_6A_7A_{11} - A_6A_8A_{10} \qquad DT_{10} = A_1A_7A_{12} + A_3A_8A_{10} - A_3A_7A_{11}$$

$$DT_{11} = A_3A_4A_{11} + A_1A_6A_{10} - A_1A_4A_{12} \qquad DT_{12} = -A_1A_6A_7 - A_3A_4A_8$$

$$DT_{13} = A_4A_9A_{11} + A_5A_8A_{10} - A_5A_7A_{11} \qquad DT_{14} = A_1A_9A_{10} + A_2A_7A_{11} - A_2A_8A_{10}$$

$$DT_{15} = -A_1A_5A_{10} - A_2A_4A_{11} \qquad DT_{16} = A_1A_5A_7 - A_1A_4A_9 + A_2A_4A_8$$

where

$$D = \begin{vmatrix} 0 & A_1 & A_2 & A_3 \\ A_4 & 0 & A_5 & A_6 \\ A_7 & A_8 & A_9 & 0 \\ A_{10} & A_{11} & 0 & A_{12} \end{vmatrix}$$

$$Vb_{11} = v_{11}C_{11}^f + C_{11}^m(v_{12} + v_{21} + v_{22}) + (C_{12}^m - C_{12}^f)(Q_2 + Q_3)$$

$$Vb_{12} = \frac{h}{h_1}(C_{12}^m v_{12} + Q_1 C_{22}^m + Q_3 C_{23}^m) + \frac{h}{h_2}(C_{12}^m v_{21} + Q_2 C_{22}^m + Q_4 C_{23}^m)$$

$$Vb_{13} = \frac{l}{l_1}(C_{12}^m v_{21} + Q_2 C_{23}^m + Q_4 C_{22}^m) + \frac{l}{l_2}(C_{12}^m v_{12} + Q_1 C_{23}^m + Q_3 C_{22}^m)$$

$$Vb_{22} = \frac{h}{h_1}[C_{22}^m(v_{12} + Q_1') + Q_3' C_{23}^m] + \frac{h}{h_2}[C_{22}^m(v_{21} + Q_2') + Q_4' C_{23}^m]$$

$$Vb_{23} = \frac{l}{l_1}[C_{23}^m(v_{21} + Q_2') + Q_4' C_{22}^m] + \frac{l}{l_2}[C_{23}^m(v_{12} + Q_1') + Q_3' C_{22}^m]$$

$$Vb_{33} = \frac{l}{l_1}[C_{22}^m(v_{21} + Q_4'') + Q_2'' C_{23}^m] + \frac{l}{l_2}[C_{22}^m(v_{12} + Q_3'') + Q_1'' C_{23}^m]$$

$$Vb_{44} = \frac{C_{44}^m\{C_{44}^f[h(V_{11} + V_{21}) + h_2(V_{12} + V_{22})] + C_{44}^m h_1(V_{12} + V_{22})\}}{h_1 C_{44}^m + h_2 C_{44}^f}$$

$$Q_i = v_{11}C_{12}^f(T_i + T_{i+8}) - v_{12}C_{12}^m\left(\frac{h_2}{h_1}T_{i+4} + \frac{l_1}{l_2}T_{i+8}\right) - v_{21}C_{12}^m\left(\frac{h_1}{h_2}T_i + \frac{l_2}{l_1}T_{i+12}\right) + v_{22}C_{12}^m(T_{i+4} + T_{i+12}) \qquad i = 1,2,3,4$$

$$Q_i' = v_{11}\left(C_{22}^f T_i + C_{23}^f T_{i+8}\right) - v_{12}\left(C_{22}^m \frac{h_2}{h_1} T_{i+4} + C_{23}^m \frac{l_1}{l_2} T_{i+8}\right) - v_{21}\left(C_{22}^m \frac{h_1}{h_2} T_i + C_{23}^m \frac{l_2}{l_1} T_{i+12}\right)$$
$$+ v_{22}\left(C_{22}^m T_{i+4} + C_{23}^m T_{i+12}\right) \qquad i = 1,2,3,4$$

$$Q_i'' = v_{11}\left(C_{23}^f T_i + C_{22}^f T_{i+8}\right) - v_{12}\left(C_{23}^m \frac{h_2}{h_1} T_{i+4} + C_{22}^m \frac{l_1}{l_2} T_{i+8}\right) - v_{21}\left(C_{23}^m \frac{h_1}{h_2} T_i + C_{22}^m \frac{l_2}{l_1} T_{i+12}\right)$$
$$+ v_{22}\left(C_{23}^m T_{i+4} + C_{22}^m T_{i+12}\right) \qquad i = 1,2,3,4$$

$$VH_{11} = Q_1\left(C_{11}^m - C_{12}^m\right)\left(\varepsilon_{22}^{p\,(12)} - \varepsilon_{22}^{p\,(22)}\right) + Q_2\left[\left(C_{11}^m - C_{12}^m\right)\varepsilon_{22}^{p\,(21)} - \left(C_{11}^m - C_{12}^m\right)\varepsilon_{22}^{p\,(11)}\right]$$
$$+ Q_3\left[\left(C_{11}^m - C_{12}^m\right)\varepsilon_{33}^{p\,(12)} - \left(C_{11}^m - C_{12}^m\right)\varepsilon_{33}^{p\,(11)}\right] + Q_4\left(C_{11}^m - C_{12}^m\right)\left(\varepsilon_{33}^{p\,(21)} - \varepsilon_{33}^{p\,(22)}\right)$$
$$+ v_{11}\left(C_{11}^f - C_{12}^f\right)\varepsilon_{11}^{p\,(11)} + \left(C_{11}^m - C_{12}^m\right)\left(v_{12}\varepsilon_{11}^{p\,(12)} + v_{21}\varepsilon_{11}^{p\,(21)} + v_{22}\varepsilon_{11}^{p\,(22)}\right)$$

$$VH_{22} = Q_1'\left(C_{11}^m - C_{12}^m\right)\left(\varepsilon_{22}^{p\,(12)} - \varepsilon_{22}^{p\,(22)}\right) + Q_2'\left[\left(C_{11}^m - C_{12}^m\right)\varepsilon_{22}^{p\,(21)} - \left(C_{11}^m - C_{12}^m\right)\varepsilon_{22}^{p\,(11)}\right]$$
$$+ Q_3'\left[\left(C_{11}^m - C_{12}^m\right)\varepsilon_{33}^{p\,(12)} - \left(C_{11}^m - C_{12}^m\right)\varepsilon_{33}^{p\,(11)}\right] + Q_4'\left(C_{11}^m - C_{12}^m\right)\left(\varepsilon_{33}^{p\,(21)} - \varepsilon_{33}^{p\,(22)}\right)$$
$$+ v_{11}\left(C_{11}^f - C_{12}^f\right)\varepsilon_{22}^{p\,(11)} + \left(C_{11}^m - C_{12}^m\right)\left(v_{12}\varepsilon_{22}^{p\,(12)} + v_{21}\varepsilon_{22}^{p\,(21)} + v_{22}\varepsilon_{22}^{p\,(22)}\right)$$

$$VH_{33} = Q_1''\left(C_{11}^m - C_{12}^m\right)\left(\varepsilon_{22}^{p\,(12)} - \varepsilon_{22}^{p\,(22)}\right) + Q_2''\left[\left(C_{11}^m - C_{12}^m\right)\varepsilon_{22}^{p\,(21)} - \left(C_{11}^m - C_{12}^m\right)\varepsilon_{22}^{p\,(11)}\right]$$
$$+ Q_3''\left[\left(C_{11}^m - C_{12}^m\right)\varepsilon_{33}^{p\,(12)} - \left(C_{11}^m - C_{12}^m\right)\varepsilon_{33}^{p\,(11)}\right] + Q_4''\left(C_{11}^m - C_{12}^m\right)\left(\varepsilon_{33}^{p\,(21)} - \varepsilon_{33}^{p\,(22)}\right)$$
$$+ v_{11}\left(C_{11}^f - C_{12}^f\right)\varepsilon_{33}^{p\,(11)} + \left(C_{11}^m - C_{12}^m\right)\left(v_{12}\varepsilon_{33}^{p\,(12)} + v_{21}\varepsilon_{33}^{p\,(21)} + v_{22}\varepsilon_{33}^{p\,(22)}\right)$$

$$VH_{12} = 2\left[V_{11}C_{44}^f\varepsilon_{12}^{p\,(11)} + C_{44}^m\left(V_{12}\varepsilon_{12}^{p\,(12)} + V_{21}\varepsilon_{12}^{p\,(21)} + V_{22}\varepsilon_{12}^{p\,(22)}\right)\right] + \frac{2}{h}C_{44}^m\left(V_{22}h_1 - V_{12}H_2\right)\left(\varepsilon_{12}^{p\,(12)} - \varepsilon_{12}^{p\,(22)}\right)$$
$$- \frac{2}{h_1C_{44}^m + h_2C_{44}^f}\left(V_{11}h_2C_{44}^f - V_{21}h_1C_{44}^m\right)\left(C_{44}^f\varepsilon_{12}^{p\,(11)} - C_{44}^m\varepsilon_{12}^{p\,(21)}\right)$$

$$\underline{\alpha}^* = \underline{\alpha}^m + \left[\underline{\alpha}^f - \underline{\alpha}^m\right]\left[\underline{S}^f - \underline{S}^m\right]^{-1}\left[\underline{S}^* - \underline{S}^m\right]$$

where $\underline{\alpha}^*$ is the effective CTE vector, $\underline{\alpha}^m$ is the matrix CTE vector, $\underline{\alpha}^f$ is the fiber CTE vector, $\underline{S}^*$ is the effective compliance matrix, $\underline{S}^m$ is the matrix compliance matrix, and $\underline{S}^f$ is the fiber compliance matrix.

$$C_{11}^* = b_{11}$$

$$C_{12}^* = C_{13}^* = \frac{b_{12} + b_{13}}{2}$$

$$C_{22}^* = C_{33}^* = \frac{3}{8}(b_{22} + b_{33}) + \frac{b_{23}}{4} + \frac{b_{66}}{2}$$

$$C_{23}^* = \frac{b_{22} + b_{33}}{8} + \frac{3b_{23}}{4} - \frac{b_{66}}{2}$$

$$Vb_{44} = \frac{C_{44}^m\left\{C_{44}^f\left[h(V_{11} + V_{21}) + h_2(V_{12} + V_{22})\right] + C_{44}^m h_1(V_{12} + V_{22})\right\}}{h_1 C_{44}^m + h_2 C_{44}^f}$$

$$VH_{12} = 2\left[V_{11}C_{44}^f \varepsilon_{12}^{p\,(11)} + C_{44}^m\left(V_{12}\varepsilon_{12}^{p\,(12)} + V_{21}\varepsilon_{12}^{p\,(21)} + V_{22}\varepsilon_{12}^{p\,(22)}\right)\right] + \frac{2}{h}C_{44}^m(V_{22}h_1 - V_{12}H_2)\left(\varepsilon_{12}^{p\,(12)} - \varepsilon_{12}^{p\,(22)}\right)$$
$$- \frac{2}{h_1 C_{44}^m + h_2 C_{44}^f}\left(V_{11}h_2 C_{44}^f - V_{21}h_1 C_{44}^m\right)\left(C_{44}^f \varepsilon_{12}^{p\,(11)} - C_{44}^m \varepsilon_{12}^{p\,(21)}\right)$$

REPORT DOCUMENTATION PAGE

Form Approved
OMB No. 0704-0188

1. AGENCY USE ONLY (*Leave blank*)	2. REPORT DATE	3. REPORT TYPE AND DATES COVERED
	August 1994	Final Contractor Report

4. TITLE AND SUBTITLE

Micromechanical Modeling of the Thermal Expansion of Graphite/Copper Composites With Nonuniform Microstructure

5. FUNDING NUMBERS

WU–505–90–52
G–NAG3–1319

6. AUTHOR(S)

Brett A. Bednarcyk and Marek-Jerzy Pindera

7. PERFORMING ORGANIZATION NAME(S) AND ADDRESS(ES)

University of Virginia
Charlottesville, Virginia 22903

8. PERFORMING ORGANIZATION REPORT NUMBER

E–9050

9. SPONSORING/MONITORING AGENCY NAME(S) AND ADDRESS(ES)

National Aeronautics and Space Administration
Lewis Research Center
Cleveland, Ohio 44135–3191

10. SPONSORING/MONITORING AGENCY REPORT NUMBER

NASA CR–195368

11. SUPPLEMENTARY NOTES

Project Manager, Robert V. Miner, Materials Division, NASA Lewis Research Center, organization code 5120, (216) 433–9515.

12a. DISTRIBUTION/AVAILABILITY STATEMENT

Unclassified - Unlimited
Subject Category 26

12b. DISTRIBUTION CODE

13. ABSTRACT ***(Maximum 200 words)***

Two micromechanical models were developed to investigate the thermal expansion of graphite/copper (Gr/Cu) composites. The models incorporate the effects of temperature-dependent material properties, matrix inelasticity, initial residual stresses due to processing history, and nonuniform fiber distribution. The first model is based on the multiple concentric cylinder geometry, with each cylinder treated as a two-phase composite with a characteristic fiber volume fraction. By altering the fiber volume fraction of the individual cylinders, unidirectional composites with radially nonuniform fiber distributions can be investigated using this model. The second model is based on the inelastic lamination theory. By varying the fiber content in the individual laminae, composites with nonuniform fiber distribution in the thickness direction can be investigated. In both models, the properties of the individual regions (cylinders or laminae) are calculated using the method of cells micromechanical model. Classical incremental plasticity theory is used to model the inelastic response of the copper matrix at the micro-level. The models were used to characterize the effects of nonuniform fiber distribution on the thermal expansion of Gr/Cu. These effects were compared to the effects of matrix plasticity, choice of stress-free temperature, and slight fiber misalignment. It was found that the radially nonuniform fiber distribution has little effect on the thermal expansion of Gr/Cu but could become significant for composites with large fiber-matrix transverse CTE and Young's modulus mismatch. The effect of nonuniform fiber distribution in the through-thickness direction of a laminate was more significant, but only approached that of the stress-free temperature for the most extreme cases that include large amounts of bending. Subsequent comparison with experimental thermal expansion data indicated the need for more accurate characterization of the graphite fiber thermo-mechanical properties. Correlation with cyclic data revealed the presence of a mechanism not considered in the developed models. The predicted response did, however, exhibit ratcheting behavior that has been observed experimentally in Gr/Cu. Finally, simulation of the actual fiber distribution of particular specimens had little effect on the predicted thermal expansion.

14. SUBJECT TERMS	15. NUMBER OF PAGES
Composite materials; Metal matrix composites; Thermal expansion; Solid mechanics	142
	16. PRICE CODE: A07

17. SECURITY CLASSIFICATION OF REPORT	18. SECURITY CLASSIFICATION OF THIS PAGE	19. SECURITY CLASSIFICATION OF ABSTRACT	20. LIMITATION OF ABSTRACT
Unclassified	Unclassified	Unclassified	